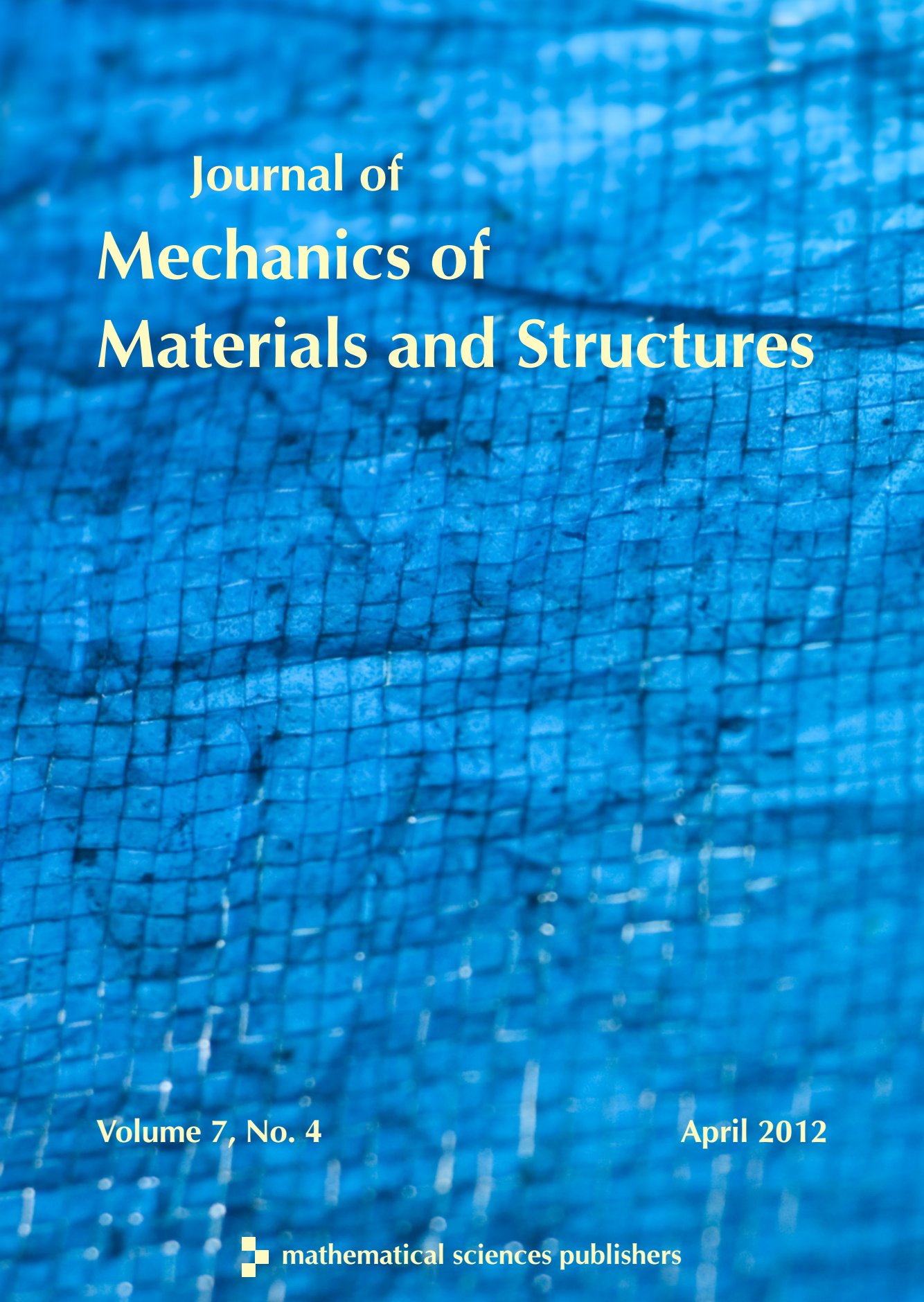

Volume 7, No. 4 April 2012

mathematical sciences publishers

JOURNAL OF MECHANICS OF MATERIALS AND STRUCTURES

jomms.net

Founded by Charles R. Steele and Marie-Louise Steele

See http://jomms.net for submission guidelines.

JoMMS (ISSN 1559-3959) is published in 10 issues a year. The subscription price for 2012 is US $555/year for the electronic version, and $735/year (+$60 shipping outside the US) for print and electronic. Subscriptions, requests for back issues, and changes of address should be sent to Mathematical Sciences Publishers, Department of Mathematics, University of California, Berkeley, CA 94720–3840.

JoMMS peer-review and production is managed by EditFLOW® from Mathematical Sciences Publishers.

PUBLISHED BY
mathematical sciences publishers
http://msp.org/

A NON-PROFIT CORPORATION

Typeset in LaTeX

JOURNAL OF MECHANICS OF MATERIALS AND STRUCTURES
Vol. 7, No. 4, 2012

ANALYTICAL STUDY OF PLASTIC DEFORMATION OF CLAMPED CIRCULAR PLATES SUBJECTED TO IMPULSIVE LOADING

HASHEM BABAEI AND ABOLFAZL DARVIZEH

This paper presents an analytical method for determining deflection of fully clamped thin circular plates. The plates are made from a rigid perfectly plastic material and subjected to a transverse localized and uniform blast loading. The essence of the model is to describe the deformation profile with the aid of a zero-order Bessel function and to perform energy analysis. This provides a method for predicting the plastic deformation of circular plates under impulsive loading. It can be also regarded as an attempt to use the energy method for different impulsive loading conditions. Calculations of the cases indicate that the proposed analytical models are based on reasonable assumptions. The solutions obtained are in very good agreement with different sets of experimental results.

A list of symbols can be found on page 320.

1. Introduction

Circular plates are common structural elements, which may, in many applications, be subjected to impact and blast loads. Their large deflection and dynamic response under such conditions has received great attention [Jones 1989]. An understanding of the response of structures when subjected to dynamic loads which produce large plastic deformations and damage is important in solving a variety of engineering problems. Despite significant progresses which have been made in this field during the past decade, complete theoretical analysis of the dynamic structural response is still a formidable task, even for very simple structures such as beams and plates [Chen et al. 2005]. Recently, various simplified models have been developed for predicting the dynamic response of circular plate structures subjected to intense blast loads. Wen et al. [1995a] developed a quasistatic procedure to predict the deformation and failure of a clamped beam struck transversely at any point by a mass traveling at low velocities. A similar procedure has been proposed in [Wen et al. 1995b; 1995c] to construct failure maps for fully clamped metal beams and circular plates under impulsive loadings using a hybrid model (i.e., r.p.p. for the bending-membrane solution and a power law for the effects of local shear) [Wen 1998].

The present paper attempts to explain a theoretical formulation based on energy method. The major objective is to predict high rate plastic deformation of circular plate subjected to transverse impulsive loading and for clamped boundary condition. The shape of deformation profile was described using a Bessel function of zero order. The key assumption employed in the method is that effects of circumferential and radial strains are dominate during deformation process and thickness strain is negligible which in turn simplifies the formulation and reduces the mathematical complexity of the problem.

Keywords: circular plate, blast load, localized load, uniform load, deformation, Bessel function.

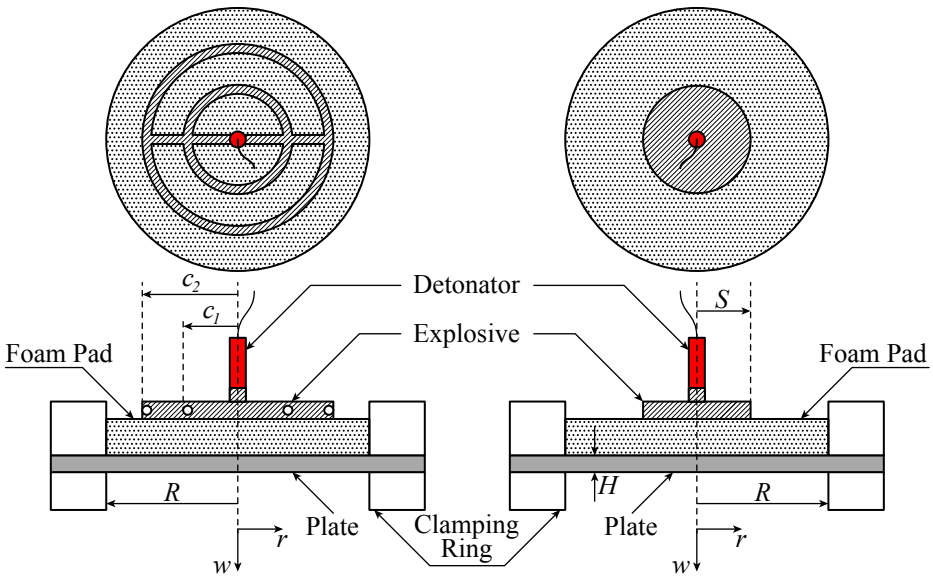

Figure 1. Schematic of two explosive conditions: uniform load (left) and localized load (right).

2. Analytical analysis

Uniform and localized loads on plates are two different explosive conditions which are applied in experimental work. For localized loading as in Figure 1 (left), the disc-shaped explosive is laid on a polystyrene pad. The explosive height and diameter is based on the loading required. In this case, the distribution of blast load is focused (localized).

For uniform loading as in Figure 1 (right), the explosive is laid out on concentric annuli. The explosive rings are connected by a cross leader of explosive. Concentric annuli are used instead of spreading the explosive over the entire area, because the explosive does not detonate if the charge thickness is less than two millimeters. According to the figure, the concentric annuli are set at radii $0.41R$ and $0.82R$. There is a polystyrene pad between shaped explosive and plate. In this case, the distribution of blast load on target plate is uniform.

Localized load. In the theoretical analysis, the large deflection problem of thin circular plate has been regarded as prototype on which various modeling concepts could be conveniently employed. One is wave form solution on the transient responses of circular membrane as proposed in [Symonds and Wierzbicki 1979; Wierzbicki and Nurick 1996]. The result obtained is the zero-order Bessel function of the first kind for the deflected shapes of membrane. Based on this deduction and similarity of zero-order Bessel function curve with deflection profile of circular plate, it is assumed that, a suitable mathematical function to describe the deflection profile of a circular plate is the zero-order Bessel function of the first kind as in [Gharababaei and Darvizeh 2010]

$$w(r) = W_\circ J_0\Big(\frac{a \cdot r}{R}\Big), \tag{1}$$

where $w(r)$ is the transverse displacement of the plate, $W_\circ$ is the transverse displacement at the center, r, R are the radial coordinate and outer radius of the plate, and a is first root of J_0, with approximate value 2.4048.

The strain energy per unit area in a circular plate is

$$dU = \sigma_r \, d\varepsilon_r + \sigma_\theta \, d\varepsilon_\theta. \tag{2}$$

It is assumed that radial and circumferential strains are significant and thickness strain ε_t is negligible.

The total strain energy during the deformation of plate is

$$U_T = \int_V U \cdot dV. \tag{3}$$

The total strain energy of a deformed circular plate consists of a bending strain energy U_b and a membrane strain energy U_m:

$$U_T = U_b + U_m. \tag{4}$$

For U_b, according to (1), the bending strains are

$$\varepsilon_{rb} = -z\frac{\partial^2 w}{\partial r^2} = W_\circ z\frac{a^2}{R^2}\left[J_0\left(\frac{ar}{R}\right) - \frac{R}{ra}J_1\left(\frac{ar}{R}\right)\right], \tag{5}$$

$$\varepsilon_{\theta b} = -z\frac{1}{r}\frac{\partial w}{\partial r} = W_\circ z\frac{a}{rR}J_1\left(\frac{ar}{R}\right), \tag{6}$$

where ε_{rb} and $\varepsilon_{\theta b}$ are the radial bending and circumferential bending strains, J_1 is first-order Bessel function of the first kind and z is the transverse coordinate.

$$U_b = \int_V (\sigma_r \varepsilon_{rb} + \sigma_\theta \varepsilon_{\theta b}) \, dV. \tag{7}$$

For materials insensitive to hydrostatic pressure, such as metals, the hydrostatic component of the stress tensor does not have a significant influence on yielding and plastic flow. Therefore these components can be subtracted from the stress tensor and it is common practice to employ the Tresca or von Mises yield criteria and the von Mises flow rules. Introducing the Tresca yield criterion and the von Mises flow relation for a rigid plastic material, one obtains for the circular plate the relation

$$\sigma_r = \sigma_\theta = \sigma_d, \tag{8}$$

where σ_d is the mean dynamic flow stress. Therefore, (7) can be converted to

$$U_b = \int_0^R \int_{-H/2}^{H/2} \sigma_d(\varepsilon_{rb} + \varepsilon_{\theta b}) 2\pi r \, dz \, dr = \tfrac{1}{2}\pi\sigma_d H^2 a J_1(a) W_\circ. \tag{9}$$

For U_m, the membrane strain is

$$\varepsilon_{rm} = \frac{1}{2}\left(\frac{\partial w}{\partial r}\right)^2 = 2\pi\left(\frac{a}{R}\right)^2 \frac{W_\circ^2}{2} J_1^2\left(\frac{ar}{R}\right). \tag{10}$$

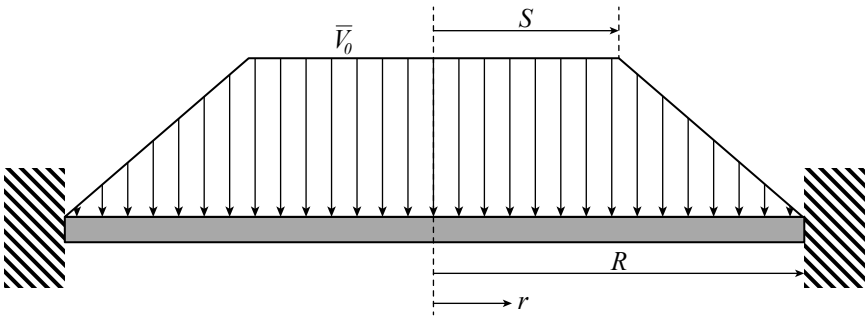

Figure 2. Initial velocity profile of circular plate subjected to localized load.

Then, the membrane energy can be obtained as

$$U_m = \int_V \sigma_r \varepsilon_{rm} dV = 2\pi\sigma_d \left(\frac{a}{R}\right)^2 \left[\int_0^R \int_{-H/2}^{H/2} \frac{W_\circ^2}{2} J_1^2\left(\frac{ar}{R}\right)\right] r\, dz\, dr = \tfrac{1}{2}\pi\sigma_d H (a J_1(a) W_\circ)^2. \tag{11}$$

When the plate is under a large deformation, the bending strain energy is much lower than the membrane strain energy, because the ratio between the two is

$$\frac{U_m}{U_b} = \frac{a J_1(a) W_\circ}{H}. \tag{12}$$

In large deformation, the mid point deflection of plate $W_\circ$ is approximately more than $5H$. Therefore,

$$U_m \approx 6U_b. \tag{13}$$

So, in the analysis of large deformation of circular plate, the bending strain energy can be neglected completely. Thus

$$U_T = U_m. \tag{14}$$

The total strain energy is equal to the initial kinetic energy of the plate. Initial velocity profile of circular plate subjected to localized load is not uniformly and it can be approximated as trapezoid distribution; see Figure 2. By conservation of momentum, the input impulse I to the plate can be calculated as

$$I = m_1 V_1(r) + m_2 V_2(r), \tag{15}$$

where m_1 and m_2 are the plate mass in the region under the explosive and in free region, respectively, and

$$V_1(r) = V_\circ \qquad \text{for } 0 \le r \le S, \tag{16}$$

$$V_2(r) = V_\circ \frac{R-r}{R-S} \quad \text{for } S \le r \le R, \tag{17}$$

S being the radius of the explosive disc and $V_\circ$ the initial impulsive velocity in the central region of plate.

Substituting (16) and (17) into (15) yields

$$I = \rho H V_\circ \left[\int_0^S 2\pi r\, dr + \int_S^R 2\pi r \left(\frac{R-r}{R-S}\right) dr\right]. \tag{18}$$

Integrating (18) with respect to r gives

$$I = mV_\circ\psi, \tag{19}$$

where

$$m = \rho\pi R^2 H, \tag{20}$$

$$\psi = \left(\frac{S}{R}\right)^2 + \frac{1}{R-S}\left(\frac{2S^3}{3R^2} + \frac{R}{3} - \frac{S^2}{R}\right), \tag{21}$$

with ρ the density and m is the mass of the plate.

The kinetic energy imparted by an input impulse I to the plate can be calculated as

$$E_K = \frac{1}{2}mV_\circ^2 = \frac{I^2}{2m\psi^2}. \tag{22}$$

Equating (14) and (22) gives

$$[aJ_1(a)]^2 W_\circ^2 = \frac{I^2}{\rho\sigma_d(\pi RH)^2\psi^2}. \tag{23}$$

The mean dynamic flow (yield) stress σ_d can be determined by the well known Cowper–Symonds empirical equation

$$\sigma_d = \sigma_y\left[1 + \left(\frac{\dot{\varepsilon}_m}{D}\right)^{1/q}\right], \tag{24}$$

where $\dot{\varepsilon}_m$ is the mean strain rate, D and q are material constants with typical values for mild steel of $D = 40.4\,\mathrm{s}^{-1}$ and $q = 5$[1], and σ_y is the quasistatic yield stress.

Equation (24) can be estimated by (see [Symonds 1973; Wojno and Wierzbicki 1979])

$$\sigma_d = \beta\sigma_y\left(\frac{\dot{\varepsilon}_m}{D}\right)^{1/\beta q}, \tag{25}$$

where β is a constant with value 2.5.

According to (10), the strain rate $\dot{\varepsilon}$ is obtained

$$\dot{\varepsilon} = \frac{d\varepsilon_{rm}}{dt} = W_\circ\dot{W}_\circ\left(\frac{a}{R}\cdot J_1\left(\frac{ar}{R}\right)\right)^2. \tag{26}$$

The mean strain rate at $r = R$ may be expressed as

$$\dot{\varepsilon}_m = W_\circ\dot{W}_\circ\left(\frac{a\cdot J_1(a)}{R}\right)^2, \tag{27}$$

where $\dot{W}_\circ$ is the mean velocity that is estimated as

$$\dot{W}_\circ = \frac{V_\circ}{2}. \tag{28}$$

Finally, (25) can be rewritten as

$$\sigma_d = \beta\sigma_y\zeta(W_\circ)^{1/\beta q}, \tag{29}$$

where

$$\zeta = \left(\frac{I\,(a \cdot J_1(a))^2}{2\pi\rho R^4 \psi D} \right)^{1/\beta q}. \tag{30}$$

Introducing ϕ as a dimensionless impulsive parameter

$$\phi = \frac{I}{\pi R H^2 \psi \sqrt{\beta\rho\sigma_y}}, \tag{31}$$

one can rewrite (30) as

$$\zeta = \left(\sqrt{\frac{\beta\sigma_y}{\rho}} \cdot \frac{(a \cdot J(a))^2}{2D} \cdot \frac{H^2\phi}{R^3} \right)^{1/(\beta q)}. \tag{32}$$

By substituting (29) into (23), one reaches the expression for the relationship between the dimensionless displacement (ratio between midpoint deflection and thickness) and the dimensionless impulse parameter.

$$\frac{W_\circ}{H} = \left[\frac{1}{\zeta} \left(\frac{\phi}{a J_1(a)} \right)^2 \right]^{\beta q/(1+2\beta q)}. \tag{33}$$

Uniform load. In the case of a uniform load, the deflection profile is also described using the zero-order Bessel function of the first kind, but the initial velocity profile of circular plate is uniform; see Figure 3. So, by conservation of momentum, the initial velocity induced by the impulsive load is

$$\bar{V}_\circ = \frac{I}{m}, \tag{34}$$

$$\bar{E}_K = \frac{1}{2} m \bar{V}_\circ^2 = \frac{I^2}{2m}, \tag{35}$$

where $\bar{V}_\circ$ is the initial impulsive velocity and $\bar{E}_K$ is kinetic energy imparted by an input impulse I to the plate. Equating (35) and (14) gives

$$[a J_1(a)]^2 W_\circ^2 = \frac{I^2}{\rho\sigma_d (\pi R H)^2}. \tag{36}$$

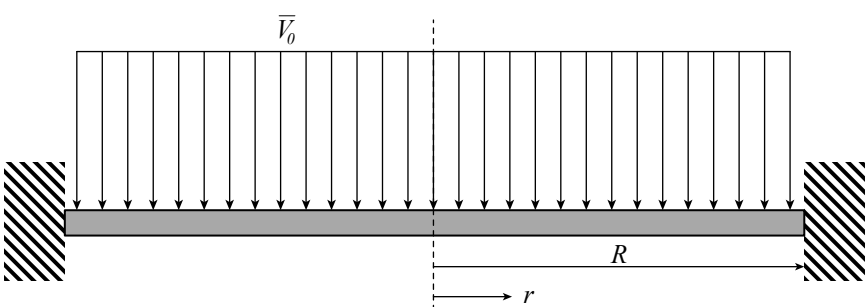

Figure 3. Initial velocity profile of circular plate subjected to uniform load.

Similarly to the preceding section, the mean dynamic flow (yield) stress σ_d can be determined as follows:

$$\sigma_d = \beta\sigma_y\bar{\zeta}\left(\frac{W_\circ}{H}\right)^{1/\beta q}, \tag{37}$$

where

$$\bar{\zeta} = \left(\frac{I(a\cdot J_1(a))^2}{2\pi\rho R^4 D}\right)^{1/\beta q}. \tag{38}$$

Introducing $\bar{\phi}$ as a dimensionless impulsive parameter

$$\bar{\phi} = \frac{I}{\pi R H^2\sqrt{\beta\rho\sigma_y}}. \tag{39}$$

Equation (38) also can be rewritten as

$$\bar{\zeta} = \left(\sqrt{\frac{\beta\sigma_y}{\rho}}\cdot\frac{(a\cdot J(a))^2}{2D}\cdot\frac{H^2\bar{\phi}}{R^3}\right)^{1/\beta q}. \tag{40}$$

Similar to the procedure employed in previous section, by substituting (37) into (36), it leads to expression for the relationship between the midpoint-deflection-to-thickness ratio (dimensionless displacement) and dimensionless impulse parameter.

$$\frac{W_\circ}{H} = \left[\frac{1}{\bar{\zeta}}\left(\frac{\bar{\phi}}{aJ_1(a)}\right)^2\right]^{\beta q/(1+2\beta q)}. \tag{41}$$

3. Results of experimental tests

The different experimental results used in this paper have been obtained through similar procedures. The experimental method consisted of creating an impulsive load with the aid of plastic explosive and measuring the impulse using a blast pendulum. The test plates are made from mild steel material with various thicknesses and radii. The test plates were sandwiched securely by support plates as shown in Figure 4 which were in turn fixed to ballistic pendulum [Jacob et al. 2007].

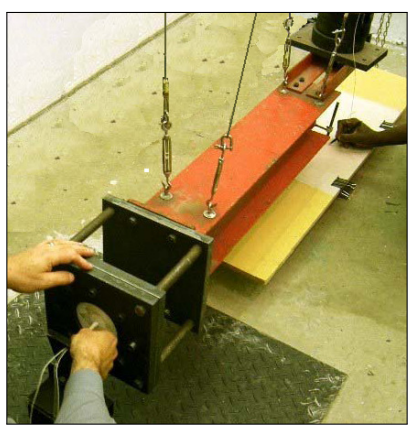

Figure 4. Experimental set-up [Jacob et al. 2007].

Experiment number and source	Data points	$2R$ (mm)	H (mm)	Load type	Load ratio S/R	σ_y (MPa)	$W_{\circ,\min}$ (mm)	$W_{\circ,\max}$ (mm)	$I_{\min}$ (N s)	$I_{\max}$ (N s)
1. [Chung Kim Yuen and Nurick 2000]	20	100	1.6, 3.6	loc.	0.25, 0.33 0.4	252	16	31.3	6.6	31.3
2. [Bodner and Symonds 1979]	21	64	1.9	loc.	0.33, 0.5	223	2.5	11.4	0.85	4.
3. [Nurick and Radford 1997]	42	100	1.6	loc.	0.18, 0.25 0.33, 0.4	194	5.4	29.9	2.7	12.4
4. [Nurick 1989]	21	100	1.6	unif.	—	282	6.14	19.8	5.6	15.6
5. [Nurick and Teeling-Smith 1994]	143	100	1.6	unif.	—	270	4.62	27.9	4.55	22.04
6. [Nurick and Lumpp 1996]	7	100	1.6	unif.	—	255	7.26	20.43	5.21	16.47
7. [Nurick et al. 1996]	113	60, 80 100, 120	1.6	unif.	—	290	2.7	34.3	1.4	30.9
8. [Bodner and Symonds 1979]	8	64	1.9	unif.	—	223	0.86	12.34	0.91	7.15
9. [Thomas and Nurick 1995]	20	100	3–3.9	unif.	—	262	5.6	20.9	4.6	16.3

Table 1. Summary of circular plate experimental conditions. Density $\rho = 7860\,\text{kg/m}^3$ in all cases. For the meaning of the variables see the text or the list on page 320.

The impulsive load is provided by a shaped plastic explosive charge placed over the test plate. The shape of charge adjusts localized or uniform according to Figure 1. The explosive charge is placed on a 12–16 mm thick polystyrene pad mounted directly onto the plate. The reason for using a polystyrene pad is to prevent spalling. A detonator taped with 1 gram of explosive was attached to the center of the explosive disk. Table 1 summarizes different load conditions and plate geometries for various experimental reports for clamped circular mild steel plates subjected to localized and uniform blast loads [Chung Kim Yuen and Nurick 2000; Bodner and Symonds 1979; Nurick and Radford 1997; Nurick 1989; Nurick and Teeling-Smith 1994; Nurick and Lumpp 1996; Nurick et al. 1996; Thomas and Nurick 1995].

4. Comparison of the experimental and analytical results

Comparison with experimental results. The results obtained from analytical models in the preceding section — (33) and (41) — are now compared with various sets of experimental results reported in the literature (Table 1).

Figure 5 compares the theoretical values of the midpoint-deflection-to-thickness ratio obtained using (33) with the experimental values for different series of experiments from the literature, performed using a localized load. The ratio is shown as a function of the dimensionless impulse (ϕ). The results of the present model are generally in good agreement with the experimental ones. In three cases — parts (a2), (b1), (c1) of the figure — the agreement is not so good, but even then the experimental values still fall within a range of ± 1 from the confidence line of (33) with confidence level of 83%, 100% and 52%, respectively.

Similarly, Figure 6 compares the theoretical values of the midpoint-deflection-to-thickness ratio obtained using (41) with the experimental values from the literature, in the case of a uniform load. Again we see generally good agreement, suggesting that the model can successfully predict central deflection.

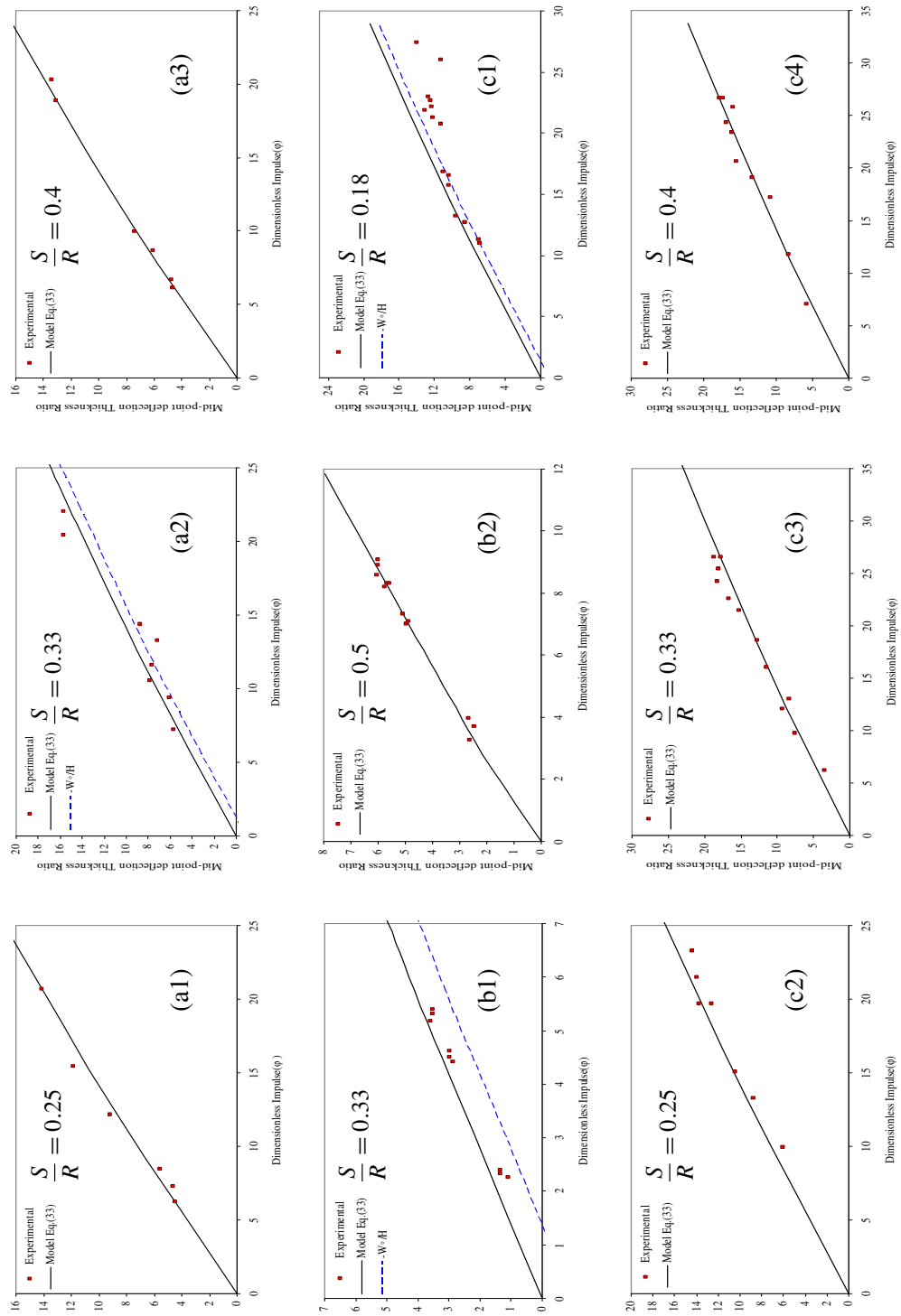

Figure 5. Comparison between experimental and model data: midpoint-deflection-to-thickness ratio versus dimensionless number (ϕ), under localized load. Comparison data for (a1)–(a3) from [Chung Kim Yuen and Nurick 2000]; for (b1)–(b2) from [Bodner and Symonds 1979]; for (c1)–(c4) from [Nurick and Radford 1997].

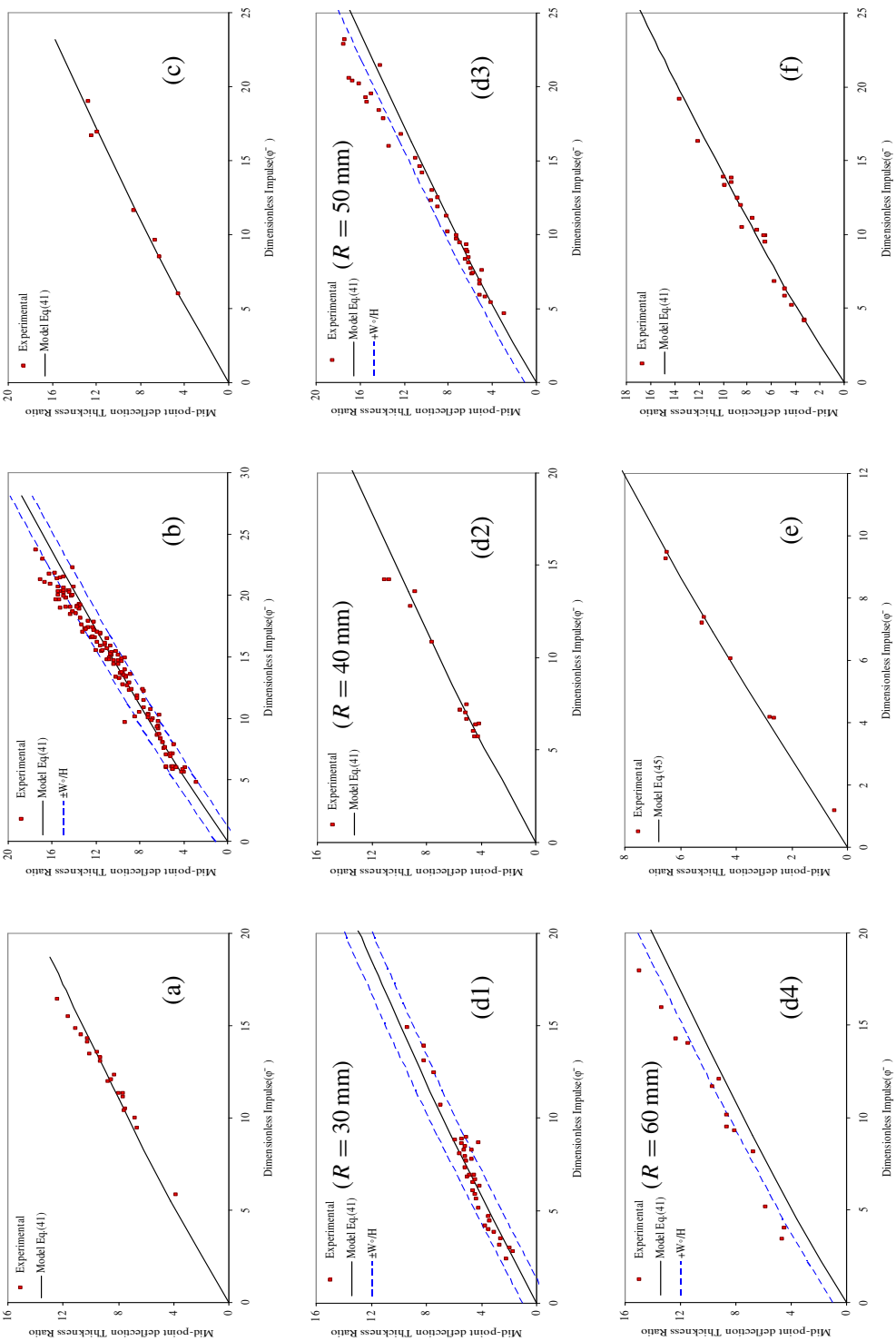

Figure 6. Comparison between experimental and model data: midpoint-deflection-to-thickness ratio versus dimensionless number (ϕ), under uniform load. Comparison data for (a) from [Nurick 1989]; for (b) from [Nurick and Teeling-Smith 1994]; for (c) from [Nurick and Lumpp 1996]; for (d1)–(d4) from [Nurick et al. 1996]; for (e) from [Bodner and Symonds 1979]; for (f) from [Thomas and Nurick 1995].

In parts (b), (d1), (d3), and (d4) some experimental points do not fit with values of model; these points fall within the ± 1 confidence line of (41) with confidence level of 94%, 99%, 78% and 42%, respectively.

Thus the proposed model can be used in most cases to predict midpoint deflection thickness ratio for different conditions of uniform and localized loads. Some experimental results obtained from literature as shown in Figures 5(c1) and 6(d4) do show a big difference with the results obtained from the present model. This could be due to incorrect impulse measurement or anisotropy in material properties.

Comparison with other formulas. There have been many research efforts for theoretical modeling the dynamic response and deformation of thin plates to predict the relationship of deflection-thickness ratio as a function of impulse, plate geometry and material properties. These models predict maximum midpoint deflection of circular plates for localized and uniform loads: we mention in particular [Nurick and Martin 1989], which supplies the equation

$$\frac{W_\circ}{H} = \frac{0.318I}{H^2 R\sqrt{\rho\sigma_y}}\left(1 + \ln\frac{R}{S}\right) \tag{42}$$

for the ratio between midpoint deflection and thickness, and [Gharababaei et al. 2010], which supplies

$$\frac{W_\circ}{H} = \frac{0.12I}{H^2 R\sqrt{\rho\sigma_y}}\,\frac{R}{S}. \tag{43}$$

Both of these apply to the case of localized loads. For case of uniform loads we have from [Nurick and Martin 1989]

$$\frac{W_\circ}{H} = \frac{f\,I}{H^2 R\sqrt{\rho\sigma_y}} \tag{44}$$

where the factor f is given by those authors as 0.135; values from other authors (cited in [Nurick and Martin 1989]) include 0.318 (Hudson), 0.212 (Symonds and Wierzbicki), 0.132 (Lipman), 0.260 (Jones), and 0.382 (Batra and Dubey).

The table below compares the RMSE obtained with the literature equations (42)–(44) and with the equations from our model, (33) and (41)). It can be observed that the models introduced in this paper have much less RMSE compared with those reported in (42)–(44).

model	RMSE	model	RMSE
(42) [Nurick and Martin 1989]	0.042	(44) [Nurick and Martin 1989]	1.055
(43) [Gharababaei et al. 2010]	0.045	(44) (Hudson)	12.914
(33) (present)	0.037	(44) (Symonds and Wierzbicki)	2.318
		(44) (Lipman)	1.136
		(44) (Jones)	8.439
		(44) (Batra and Dubey)	28.064
		(41) (present)	0.052

5. Conclusion

The models developed in the present work account for energy dissipation through plastic work. Two different analytical models were presented, for localized and uniform blast loads. The solution is determined

completely through material and geometrical parameters. A zero Bessel function was used to determine the deflection profile for different types of impulsive loading (localized and uniform). Subsequent calculation indicated that the accuracy of quantities such as central deflection is sensitive to the function describing the exact shape of deflection profile. Analytical predictions of present models for central deflection of fully clamped impulsively loaded circular plates are in good agreement with numerous experimental data. This is despite of fact that calculation based on the analytical solution of present model involved only values of radial and circumferential strains, the values of thickness strain considered being relatively small and negligible.

Although the models in (33) and (41) indicate a nonlinear relationship between deflection and impulsive load, Figures 2 and 3 show an almost linear relationship between these parameters. In fact, the linearity or nonlinearity of the models depends on material properties (q) of the plates.

In summary, the models presented in this paper can predict central deflection of the plate subjected to impulsive loading accurately. The values obtained for central deflection from analytical models developed here show less error, in comparison with experimental results, than those obtained from other models already reported in literature. It is intended that this analytical approach will be complementary to the existing ones. However, the current establishment of equations in the present models is more straightforward.

Acknowledgements

The authors express their thanks to Prof. G. N. Nurick, Dr. G. S. Langdon and Mr. T. J. Cloete for valuable discussions. The authors also thank all the members of the BISRU group at the University of Cape Town.

List of symbols

w	Transverse displacement of plate	m	Mass of plate
$W_\circ$	Transverse displacement of plate at center	ρ	Density of plate
r	Radial coordinate	E_k	Kinetic energy for localized load
z	Transverse coordinate	$\bar{E}_k$	Kinetic energy for uniform load
R	Radius of plate	I	Input impulse
H	Thickness of plate	ψ	Coefficient of load (geometric)
J_0	Zero-order Bessel function	ϕ	Dimensionless impulsive for localized load
a	First root of J_0	$\bar{\phi}$	Dimensionless impulsive for uniform load
J_1	First-order Bessel function	$\dot{\varepsilon}_m$	Mean strain rate
ε_r	Radial strain	D	Material constant, defined in (24)
ε_θ	Circumferential strain	q	Material constant, defined in (24)
ε_t	Thickness strain	V	volume of plate
σ_r	Radial stress	ζ	Dimensionless parameter for localized load
σ_θ	Circumferential stress	$\bar{\zeta}$	Dimensionless parameter for uniform load
σ_d	Mean dynamic stress	U_T	Total strain energy
σ_y	Quasistatic yield stress	U_m	Membrane strain energy
$V_\circ, \bar{V}_\circ$	Initial impulsive velocity	U_b	Bending strain energy

References

[Bodner and Symonds 1979] S. R. Bodner and P. S. Symonds, "Experiments on viscoplastic response of circular plates to impulsive loading", *Int. J. Mech. Phys. Solids* **27** (1979), 91–113.

[Chen et al. 2005] Y. Chen, J. Zhang, Y. Wang, and P. Tang, "Non-linear transient analysis of a blast-loaded circular plate resting on non viscous fluid", *Int. J. Pressure Vessels Piping* **82** (2005), 729–737.

[Chung Kim Yuen and Nurick 2000] S. Chung Kim Yuen and G. N. Nurick, "The significance of the thickness of a panel when subjected to localized blast load", pp. 491–499 in *16th symposium on military aspects of blast and shock*, Oxford, UK, 2000.

[Gharababaei and Darvizeh 2010] H. Gharababaei and A. Darvizeh, "Experimental and analytical investigation of large deformation of thin circular plates subjected to localized and uniform impulsive loading", *Int. J. Mech. based Des. Struct. Mach.* **38**:2 (2010), 171–189.

[Gharababaei et al. 2010] H. Gharababaei, N. Nariman-zadeh, and A. Darvizeh, "A simple modelling method for deflection of circular plates under impulsive loading using dimensionless analysis and singular value decomposition", *Int. J. Mech.* **26**:3 (2010), 355–361.

[Jacob et al. 2007] N. Jacob, G. N. Nurick, and G. S. Langdon, "The effect of stand-off distance on the failure of fully clamped circular mild steel plates subjected to blast loads", *Int. J. Eng. Struct.* **29** (2007), 2723–2736.

[Jones 1989] N. Jones, *Structural impact*, Cambridge University Press, Cambridge, 1989.

[Nurick 1989] G. N. Nurick, "An empirical solution for predicting maximum central deflections of impulsively loaded plates", pp. 457–464 in *Mechanical properties of materials at high rates of strain*, edited by J. Harding, Oxford, 1989.

[Nurick and Lumpp 1996] G. N. Nurick and D. M. Lumpp, "Deflection and tearing of clamped stiffened circular plates subjected to uniform impulsive loads", pp. 393–402 in *Structures under shock and impact*, edited by N. Jones et al., Computational Mechanics Publications, Southampton, UK, 1996.

[Nurick and Martin 1989] G. N. Nurick and J. B. Martin, "Deformations of thin plates subjected to impulsive loading - a review; Part I - Theoretical considerations", *Int. J. Impact Eng.* **8**:2 (1989), 159–170.

[Nurick and Radford 1997] G. N. Nurick and A. M. Radford, "Deformation and tearing of clamped circular plates subjected to localised central blast loads", pp. 276–301 in *Recent developments in computational and applied mechanics: a volume in honour of John B. Martin* (Barcelona), International Centre for Numerical Methods in Engineering (CIMNE), 1997.

[Nurick and Teeling-Smith 1994] G. N. Nurick and R. G. Teeling-Smith, "Predicting the onset of necking and hence rupture of thin plates loaded impulsively- an experimental view", pp. 431–445 in *Structures under shock and impact II*, Computational Mechanics Publications, 1994.

[Nurick et al. 1996] G. N. Nurick, M. E. Gelman, and N. S. Marshall, "Tearing of blast loaded plates with clamped boundary conditions", *Int. J. Impact Eng.* **18**:7–8 (1996), 803–827.

[Symonds 1973] P. S. Symonds, "Approximate techniques for impulsively loaded structures of rate sensitive plastic behavior", *SIAM J. Appl. Math.* **25** (1973), 462–470.

[Symonds and Wierzbicki 1979] P. S. Symonds and T. Wierzbicki, "Membrane mode solution for impulsively loaded circular plates", *J. Appl. Mech.* **46** (1979), 58–64.

[Thomas and Nurick 1995] B. M. Thomas and G. N. Nurick, "The effect of boundary conditions on thin plates subjected to impulsive loads", pp. 85–88 in *Plasticity 1995 — the 5th international symposium on plasticity and its current application*, 1995.

[Wen 1998] H. M. Wen, "Deformation and tearing of clamped circular work-hardening plates under impulsive loading", *Int. J. Pressure Vessels Piping* **75** (1998), 67–73.

[Wen et al. 1995a] H. M. Wen, T. Y. Reddy, and S. R. Reid, "Deformation and failure of clamped beams under low speed impact loading", *Int. J. Impact Eng.* **16**:3 (1995), 435–454.

[Wen et al. 1995b] H. M. Wen, T. X. Yu, and T. Y. Reddy, "Failure maps of clamped beams under impulsive loading", *Mech. Struct. Mach.* **23**:4 (1995), 353–372.

[Wen et al. 1995c] H. M. Wen, T. X. Yu, and T. Y. Reddy, "A note on the clamped circular plates under impulsive loading", *Mech. Struct. Mach.* **23**:3 (1995), 331–342.

[Wierzbicki and Nurick 1996] T. Wierzbicki and G. N. Nurick, "Large deformation of thin plates under localized impulsive loading", *Int. J. Impact Eng.* **18** (1996), 899–918.

[Wojno and Wierzbicki 1979] W. Wojno and T. Wierzbicki, "Perturbation solution for impulsively loaded viscoplastic plates", *Int. J. Non-linear Mech.* **15** (1979), 211–223.

Received 1 Aug 2011. Revised 25 Mar 2012. Accepted 8 Apr 2012.

HASHEM BABAEI: ghbabaei@guilan.ac.ir
Department of Mechanical Engineering, University of Guilan, PO Box 3756, Rasht, Iran

ABOLFAZL DARVIZEH: adarvizeh@guilan.ac.ir
Department of Mechanical Engineering, Islamic Azad University, Bandar Anzali Branch, Anzali, Iran

JOURNAL OF MECHANICS OF MATERIALS AND STRUCTURES
Vol. 7, No. 4, 2012

THEREOTICAL SOLUTIONS OF ADHESIVE STRESSES IN BONDED COMPOSITE BUTT JOINTS

GANG LI

In this paper, closed-form solutions for the adhesive stresses in bonded composite single-strap butt joints have been obtained. Two strategies were used for deriving the adhesive peel stress. The solutions are applicable to a butt joint made from different adherend and doubler laminates, as well as the unbalanced single-lap joints. In addition, three-dimensional finite element models of the unit-width composite joints were created for analyzing the adhesive stresses under a plane strain condition. A total of six joint conditions, three joint configurations and each with two layup sequences, were studied. Consistency in the peel stress predictions was obtained from the two theoretical strategies. Good agreement has been achieved between the theoretical and finite element results. The effects of the doubler thickness and laminate layup sequence on the adhesive stress variation can be displayed. The theoretical solution would provide a solid foundation for supporting the practical composite joint assessment.

A list of symbols can be found on page 345.

1. Introduction

With the recent advances in automated fiber placement equipment, composites can be effectively and extensively used in various aircraft structures. A recent example is the fuselage structure being fabricated for the Boeing 787, where large composite barrel sections are assembled. To this end, the composite joints used are critical. One possible joint option for these types of structures is the single-strap butt joint configuration. Typical attachments considered could be bonding, bolting, bonded-bolted joining, etc.

Bonded joints using adhesives with high moduli and strength would have much higher joint static strength than bolted joints [Li et al. 2012]. To improve the structural integrity, mechanical fasteners can be introduced using a hybrid (bonded-bolted) attachment approach [Kelly 2006; Li et al. 2012]. For the bonded single-strap butt joint configuration, high peak adhesive stresses exist at the bonded overlap edges, especially at the inner overlap edges [Hart-Smith 1985]. To evaluate the joint performance, the adhesive stress profiles are crucial and need to be fully understood first for further joint improvement. This is the subject of the current study.

The single-strap butt joint is actually fabricated by attaching two single-lap joints end-to-end, as shown in Figure 1. The same adhesive stress equilibrium equations exist between the single-strap and single-lap joints. Therefore, theoretical progress in the bonded single-lap joint can be applied to the single-strap butt joint. The elastic analysis of the bonded joints can be first traced back to [Volkersen 1938]. To date, elastic closed-form adhesive stress solution of the balanced single-lap joint has been well established [Goland

MSC2010: 00A05.
Keywords: adhesive stresses, closed-form solutions, composite single-strap butt joint, finite element analysis.

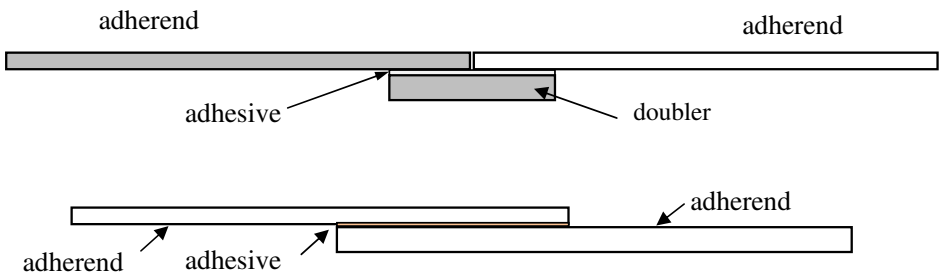

Figure 1. Schematic diagrams for a single-strap butt (top) and a single-lap joint (bottom).

and Reissner 1944; Hart-Smith 1973; Chen and Cheng 1983; Oplinger 1994; Li and Lee-Sullivan 2006a; Li and Lee-Sullivan 2006b]. When the two adherends have different geometries and/or mechanical properties, the single-lap joints are referred to as unbalanced. Due to the coupling relationship between the adhesive peel and shear stresses in the unbalance single-lap joint, the complexity of the analysis of this joint configuration is much higher than that of the balanced case. The corresponding closed-form adhesive stress solutions have not been provided by previous researchers [Hart-Smith 1973; Bigwood and Crocombe 1989; Cheng et al. 1991].

Coupling relationship between the adhesive shear and peel stresses is present in a general butt joint configuration with different doubler and adherends. Delale et al. [1981] reported their theoretical study on a bonded panel-to-substrate joint structure, a kind of butt joint configuration. The uncoupled seven-order differential equation for adhesive shear stress was provided. They gave general expressions of the closed-form solutions for adhesive shear and peel stresses using complex terms with non-zero imaginary terms. The associated integral constants and the final solutions of the adhesive stresses were not further investigated. Bigwood and Crocombe [1989] obtained the uncoupled sixth-order differential equation for the adhesive peel stress. The final closed-form stress solutions were not fully provided.

To obtain the closed-form adhesive stress solutions using explicit expressions in bonded composite butt joints, the following theoretical preparations were made in [Li 2008; 2010; Li et al. 2011]:

(1) This kind of closed-form stress solutions was obtained for the butt joint using isotropic materials.

(2) The effective Young's modulus and bending stiffness were identified for laminate beam panels.

(3) Expressions were provided for the four coefficients arising from the coupled adhesive stress differential equations in composite butt joint.

(4) A theoretical strategy for exploring adhesive peel and shear stresses was presented.

Closed-form stress solutions were successfully obtained and are presented in the current paper. Two strategies were used to derive the adhesive peel stress solutions. To effectively demonstrate the theoretical solution, three-dimensional finite element models using twenty-node brick elements were created for analyzing the unit-width joints under a plane strain condition. A total of six joint conditions, three joint configurations with two layup sequences each, were studied. One joint configuration, case 1, was a special butt joint case made of identical laminates. The other two, cases 2 and 3, were general butt joints with different adherends and doubler in bending stiffness. For the sake of brevity, only the adhesive stress solutions and the associated comparisons are present. A quantitative study of the effect of various

factors on the adhesive stress magnitude can be carried out using the obtained solutions, which is not included in the paper. The theoretical solutions would make a sound basis for practical composite butt joint applications in the aerospace industry.

2. Theoretical formulation

Joint deformation and its loading condition. A typical configuration for a bonded composite single-strap butt joint is shown in Figure 2. The two adherends are made from identical laminates, which can be different from the doubler laminate. Due to load path eccentricity, secondary bending occurs when the joint is loaded in tension. Solutions of the joint deflection, elongation, bending moment, and strain at the overlap edge region were given in [Li et al. 2011]. For a thin adhesive layer, the equations relating the adhesive stress to the joint deformation are

$$\frac{\sigma_a}{E_a} = \frac{w_u - w_d}{\eta}, \qquad \frac{\tau_a}{G_a} = \frac{u_u - u_d}{\eta}, \tag{1a}$$

where E_a and G_a are adhesive Young's and shear moduli; η is the adhesive thickness, w_u and w_d are deflections in the upper adherend and doubler and u_u and u_d are displacements in the adherend at the adherend-adhesive interface and in the doubler at the adhesive-doubler interface.

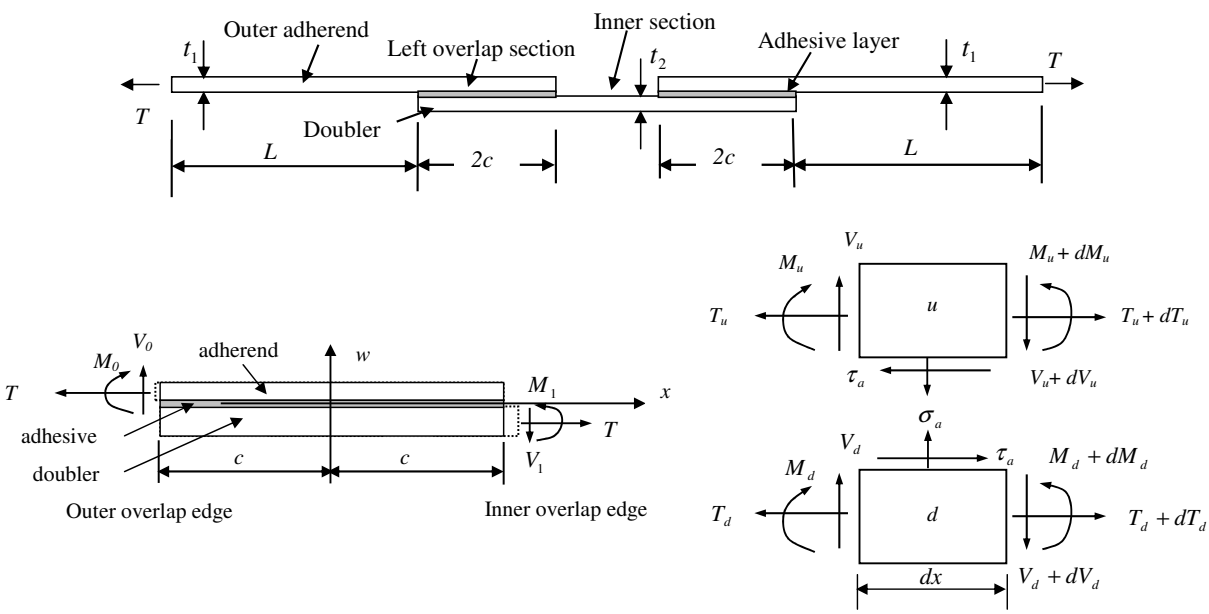

Figure 2. Top: a bonded composite butt joint in tension. Bottom left: forces at the overlap edges. Bottom right: the loading state in infinitesimal elements for upper adherend (denoted by u) and doubler (d) in the overlap section.

The axial strains of the adherend-adhesive and adhesive-doubler interfaces are

$$\epsilon_{x,\text{adh}} = \frac{du_u}{dx} = \epsilon^0_{x,\text{adh}} + \tfrac{1}{2}t_1\kappa_{x,\text{adh}} = k_{11,\text{adh}}T_u + k_{12,\text{adh}}M_u + \tfrac{1}{2}t_1\kappa_{x,\text{adh}}$$
$$= k_{11,\text{adh}}T_u + k_{12,\text{adh}}M_u + \tfrac{1}{2}t_1(k_{12,\text{adh}}T_u + k_{22,\text{adh}}M_u), \tag{1b}$$

$$\epsilon_{x,\text{doub}} = \frac{du_d}{dx} = \epsilon^0_{x,\text{doub}} - \tfrac{1}{2}t_2\kappa_{x,\text{doub}} = k_{11,\text{doub}}T_d + k_{12,\text{doub}}M_d - \tfrac{1}{2}t_2\kappa_{x,\text{doub}}$$
$$= k_{11,\text{doub}}T_d + k_{12,\text{doub}}M_d - \tfrac{1}{2}t_2(k_{12,\text{doub}}T_d + k_{22,\text{doub}}M_d), \tag{1c}$$

where the k_{ij} terms are compliances in the associated laminate in-plane constitutive equation [Li et al. 2011], as defined by (A.1a) in the Appendix.

Governing differential equations for adhesive stresses. The coupled adhesive stress differential equations for a single-strap butt joint are identical to those of a single-lap joint, except for the loading boundary conditions at the overlap edges. Through equilibrium analysis in the bonded overlap section, the adhesive stress equations can be derived (see [Cheng et al. 1991; Li 2008; 2010; Li et al. 2011]:

$$\frac{d^3\tau_a}{dx^3} + a_1\frac{d\tau_a}{dx} + a_2\sigma_a = 0, \qquad \frac{d^4\sigma_a}{dx^4} + b_1\sigma_a + b_2\frac{d\tau_a}{dx} = 0, \tag{2a}$$

where a_1, a_2, b_1, and b_2, are four basic parameters to be determined prior to the exploration of the adhesive peel and shear stresses, σ_a and τ_a. The coupling parameters a_2 and b_2 vanish when dealing with identical materials having the same thickness for the adherends and doubler. The four parameters are determined in [Li et al. 2011] to be

$$a_1 = -\frac{G_a}{\eta}(k_{11,\text{adh}} + k_{11,\text{doub}} + \tfrac{1}{2}t_1k_{12,\text{adh}} - \tfrac{1}{2}t_2k_{12,\text{doub}})$$
$$- \frac{G_a}{\eta}\big(\tfrac{1}{2}(t_1+\eta)(k_{12,\text{adh}} + \tfrac{1}{2}t_1k_{22,\text{adh}}) - \tfrac{1}{2}(t_2+\eta)(k_{12,\text{doub}} - \tfrac{1}{2}t_2k_{22,\text{doub}})\big), \tag{2b}$$

$$a_2 = \frac{G_a}{\eta}(k_{12,\text{adh}} + k_{12,\text{doub}} + \tfrac{1}{2}t_1k_{22,\text{adh}} - \tfrac{1}{2}t_2k_{22,\text{doub}}), \tag{2c}$$

$$b_1 = \frac{E_a}{\eta}(k_{22,\text{adh}} + k_{22,\text{doub}}), \tag{2d}$$

$$b_2 = -\frac{E_a}{\eta}\big(k_{12,\text{adh}} + k_{12,\text{doub}} + k_{22,\text{adh}}\tfrac{1}{2}(t_1+\eta) - k_{22,\text{doub}}\tfrac{1}{2}(t_2+\eta)\big), \tag{2e}$$

where the k_{ij} terms are presented in the Appendix.

3. Solutions for the adhesive stresses

Definitions of the butt joints in general and special cases. The general case refers to joints with different adherends and doubler in materials and/or thicknesses. The special case refers to joints with the coupling parameters $a_2 = b_2 = 0$. For this situation, the adhesive peel and shear stresses can be decoupled as in the balanced single-lap joints and it is easy to obtain the closed-form solutions [Bigwood and Crocombe 1989; Cheng et al. 1991; Hart-Smith 1973; Li and Lee-Sullivan 2006a; Li and Lee-Sullivan 2006b].

Efforts to explore the closed-form solutions are carried out for the general butt joint case in the following.

A special joint case: $a_2 = b_2 = 0$. The special joints are made from identical, symmetric and balanced laminates. In this case, the parameters are $k_{12} = 0$, $t_1 = t_2 = t$, and $k_{22,\text{adh}} = k_{22,\text{doub}} = k_{22}$. For thin adhesive layer, the other two parameters are

$$a_1 \approx -\frac{G_a}{\eta}(2k_{11} + \tfrac{t^2}{2}k_{22}) \quad \text{and} \quad b_1 = \frac{2E_a}{\eta}(k_{22}). \tag{3a}$$

The decoupled shear and peel stress equations would be

$$\frac{d^3\tau_a}{dx^3} + a_1\frac{d\tau_a}{dx} = 0, \qquad \frac{d^4\sigma_a}{dx^4} + b_1\sigma_a = 0. \tag{3b}$$

Adhesive shear stress in the special joint case. The general solution for the adhesive shear stress is then

$$\tau_a = C_{0S} + C_{1S}\cosh\bigl(x\sqrt{-a_1}\bigr) + C_{2S}\sinh\bigl(x\sqrt{-a_1}\bigr). \tag{3c}$$

The expressions for the three constants C_{0S}, C_{1S} and C_{2S}, given in the Appendix, are determined using the following three boundary conditions:

$$\int_{-c}^{c}\tau_a\,dx = -T, \quad \left.\frac{d\tau_a}{dx}\right|_{x=-c} = \frac{G_a}{\eta}(k_{11}T + \tfrac{1}{2}tk_{22}M_0), \quad \left.\frac{d\tau_a}{dx}\right|_{x=c} = \frac{G_a}{\eta}(-k_{11}T + \tfrac{1}{2}tk_{22}M_1). \tag{3d}$$

The first boundary condition is the equilibrium relationship in the adherend between the applied tensile load and the integral of the resulting shear stress in the adhesive layer. The second and third boundary conditions relate the first derivative of shear stress to the loads at two overlap edges, which are obtained by combining the first derivative of the adhesive shear stress in $(1a)_2$ and the expressions of axial strains at the adherend-adhesive and adhesive-doubler interfaces in (1b) and (1c).

Adhesive peel stress in the special joint case. The general solution for the adhesive peel stress is

$$\begin{aligned}\sigma_a = {} & C_{3S}\cosh x\bigl(\sqrt[4]{b_1/4}\bigr)\cos x\bigl(\sqrt[4]{b_1/4}\bigr) + C_{4S}\sinh x\bigl(\sqrt[4]{b_1/4}\bigr)\cos x\bigl(\sqrt[4]{b_1/4}\bigr) \\ & + C_{5S}\cosh x\bigl(\sqrt[4]{b_1/4}\bigr)\sin x\bigl(\sqrt[4]{b_1/4}\bigr) + C_{6S}\sinh x\bigl(\sqrt[4]{b_1/4}\bigr)\sin x\bigl(\sqrt[4]{b_1/4}\bigr).\end{aligned} \tag{3e}$$

The four constants $C_{3S}, \ldots, C_{6S}$, given in the Appendix, are determined using the boundary conditions

$$\left.\frac{d^2\sigma_a}{dx^2}\right|_{x=-c} = \frac{E_a}{\eta}k_{22}M_0, \quad \left.\frac{d^2\sigma_a}{dx^2}\right|_{x=c} = -\frac{E_a}{\eta}k_{22}M_1, \quad \left.\frac{d^3\sigma_a}{dx^3}\right|_{x=-c} = \frac{E_a}{\eta}k_{22}V_0, \quad \left.\frac{d^3\sigma_a}{dx^3}\right|_{x=c} = -\frac{E_a}{\eta}k_{22}V_1.$$

These four boundary conditions relate the derivatives of adhesive peel stress with the applied loads at the outer and inner overlap edges of the balanced butt joint.

The general joint case: $a_2 \neq 0$, $b_2 \neq 0$.

Adhesive shear stress in the general joint case. The uncoupled equation for the adhesive shear stress can be obtained by eliminating the peel stress in $(2a)_1$:

$$\frac{d^7\tau_a}{dx^7} + a_1\frac{d^5\tau_a}{dx^5} + b_1\frac{d^3\tau_a}{dx^3} + (a_1b_1 - a_2b_2)\frac{d\tau_a}{dx} = 0 \tag{4a}$$

The corresponding characteristic equation becomes (see [Derrick and Grossman 1987; Kreyszig 1993]):

$$\lambda\bigl(\lambda^6 + a_1\lambda^4 + b_1\lambda^2 + (a_1b_1 - a_2b_2)\bigr) = 0. \tag{4b}$$

The seven roots were previously obtained through complicated mathematical analyses in [Li 2010; Li et al. 2011]. The seven λ roots are given in the Appendix. Provided $\phi_1 = \gamma_1 - a_1/3 \geq 0$, the general solution for the adhesive shear stress can be established as

$$\begin{aligned}\tau_a = {} & C_0 + C_1 \cosh\big(x\sqrt{\gamma_1 - a_1/3}\big) + C_2 \sinh\big(x\sqrt{\gamma_1 - a_1/3}\big) \\ & + C_3 \cosh\big(x(|\phi|^{\frac{1}{2}} \cos\tfrac{\beta}{2})\big) \cos\big(x(|\phi|^{\frac{1}{2}} \sin\tfrac{\beta}{2})\big) + C_4 \sinh\big(x(|\phi|^{\frac{1}{2}} \cos\tfrac{\beta}{2})\big) \cos\big(x(|\phi|^{\frac{1}{2}} \sin\tfrac{\beta}{2})\big) \\ & + C_5 \cosh\big(x(|\phi|^{\frac{1}{2}} \cos\tfrac{\beta}{2})\big) \sin\big(x(|\phi|^{\frac{1}{2}} \sin\tfrac{\beta}{2})\big) + C_6 \sinh\big(x(|\phi|^{\frac{1}{2}} \cos\tfrac{\beta}{2})\big) \sin\big(x(|\phi|^{\frac{1}{2}} \sin\tfrac{\beta}{2})\big), \end{aligned} \tag{5a}$$

where the augment symbols ϕ and β have the same expression as in [Li 2010; Li et al. 2011] and are not spelled out here. The seven integral constants $C_0, \ldots, C_6$, given in the Appendix, are determined using the seven boundary conditions

$$\begin{aligned} & \int_{-c}^{c} \tau_a \, dx = -T, \\ & \left.\frac{d\tau_a}{dx}\right|_{x=-c} = \frac{G_a}{\eta}\big((k_{11,\mathrm{adh}} + \tfrac{1}{2}t_1 k_{12,\mathrm{adh}})T + (k_{12,\mathrm{adh}} + \tfrac{1}{2}t_1 k_{22,\mathrm{adh}})M_0\big), \\ & \left.\frac{d\tau_a}{dx}\right|_{x=c} = \frac{G_a}{\eta}\big((-k_{11,\mathrm{doub}} + \tfrac{1}{2}t_2 k_{12,\mathrm{doub}})T + (-k_{12,\mathrm{doub}} + \tfrac{1}{2}t_2 k_{22,\mathrm{doub}})M_1\big), \end{aligned} \tag{5b}$$

$$\left.\frac{d^2\tau_a}{dx^2} + a_1\tau_a\right|_{x=-c} = \frac{G_a}{\eta}(k_{12,\mathrm{adh}} + \tfrac{1}{2}t_1 k_{22,\mathrm{adh}})V_0, \quad \left.\frac{d^5\tau_a}{dx^5} + a_1\frac{d^3\tau_a}{dx^3}\right|_{x=-c} = -a_2\frac{E_a}{\eta}(k_{12,\mathrm{adh}}T + k_{22,\mathrm{adh}}M_0),$$

$$\left.\frac{d^2\tau_a}{dx^2} + a_1\tau_a\right|_{x=c} = \frac{G_a}{\eta}(\tfrac{1}{2}t_2 k_{22,\mathrm{doub}} - k_{12,\mathrm{doub}})V_1, \quad \left.\frac{d^5\tau_a}{dx^5} + a_1\frac{d^3\tau_a}{dx^3}\right|_{x=c} = a_2\frac{E_a}{\eta}(k_{12,\mathrm{doub}}T + k_{22,\mathrm{doub}}M_1),$$

where M_0 and V_0 are the bending moment and shear force at the outer overlap edge on the adherend, while M_1 and V_1 are the bending moment and shear force at the inner overlap edge on the doubler.

The first boundary condition in (5b) is obtained through the equilibrium relationship between joint adherend tensile load and the integral of the resulting shear stress in the adhesive layer. The other six boundary conditions relate different derivatives of adhesive shear stress at the outer and inner overlap edges with the applied loads at the same positions. Assuming continuity of strains at the adherend-adhesive and doubler-adhesive interfaces, as well as the continuity in the adhesive stress, the second and third boundary conditions at the two overlap edges are obtained by combining the first derivative of adhesive shear stress in $(1a)_2$ and the expressions of axial strains at the adherend-adhesive and adhesive-doubler interfaces in (1b) and (1c). Adhesive shear stress in $(1a)_2$ is differentiated twice and using the equilibrium equations of moment and tensile force to substitute for the fourth and fifth boundary conditions. To obtain the sixth and seventh boundary conditions for the uncoupled adhesive shear stress, two differentiations are applied to the adhesive stress equation in $(2a)_1$ with the aid of the peel stress expression in $(1a)_1$ and the moment-curvature relationship defined in the beam theory.

Current boundary conditions led to good agreement between the closed-form solutions of the proposed first strategy and FE results for the butt joints made of isotropic materials [Li 2010; Li et al. 2011], as well as the composite joints in the following section of the current paper.

First strategy: adhesive peel stress in the general joint case. Two strategies are presented to explore the closed-form adhesive peel stress solutions in bonded composite single-strap joints, provided the adhesive shear stress solution is known. The first is the one used in [Li 2010; Li et al. 2011], and good agreement was achieved between the theoretical and finite element results. The second was initially proposed in [Bigwood and Crocombe 1989].

The general solution of the adhesive peel stress can be explored using its fundamental equation, $(2a)_2$:

$$\frac{d^4\sigma_a}{dx^4} + b_1\sigma_a = -b_2\frac{d\tau_a}{dx}.$$

This nonhomogeneous equation can be investigated using variation of constants or Lagrange's method [Derrick and Grossman 1987; Kreyszig 1993]. The general solution is established by combining the solution of its homogeneous equation and any one particular solution of its nonhomogeneous equation. This strategy was successfully undertaken in [Li 2010; Li et al. 2011] and a detailed derivation of adhesive stresses in a bonded isotropic butt joint, where the general adhesive stress solutions were determined and good agreement was shown between closed-form solutions and finite element predictions.

The general solution of its homogeneous equation is

$$\begin{aligned}\sigma_{aH} = {} & C_{1H}\cosh x\left(\sqrt[4]{b_1/4}\right)\cos x\left(\sqrt[4]{b_1/4}\right) + C_{2H}\sinh x\left(\sqrt[4]{b_1/4}\right)\cos x\left(\sqrt[4]{b_1/4}\right)\\ & + C_{3H}\cosh x\left(\sqrt[4]{b_1/4}\right)\sin x\left(\sqrt[4]{b_1/4}\right) + C_{4H}\sinh x\left(\sqrt[4]{b_1/4}\right)\sin x\left(\sqrt[4]{b_1/4}\right).\end{aligned} \tag{6a}$$

One particular solution for its nonhomogeneous equation can be expressed in the form

$$\begin{aligned}\sigma_{ap} = {} & G_{1p}(x)\cosh x\left(\sqrt[4]{b_1/4}\right)\cos x\left(\sqrt[4]{b_1/4}\right) + G_{2p}(x)\sinh x\left(\sqrt[4]{b_1/4}\right)\cos x\left(\sqrt[4]{b_1/4}\right)\\ & + G_{3p}(x)\cosh x\left(\sqrt[4]{b_1/4}\right)\sin x\left(\sqrt[4]{b_1/4}\right) + G_{4p}(x)\sinh x\left(\sqrt[4]{b_1/4}\right)\sin x\left(\sqrt[4]{b_1/4}\right),\end{aligned} \tag{6b}$$

where the functions $G_{1p}, \ldots, G_{4p}$ are determined using the following simultaneous equations [Derrick and Grossman 1987; Kreyszig 1993], where we have set $Q = \sqrt[4]{b_1/4}$:

$$\begin{aligned}& G'_{1p}(x)\cosh x\,Q\cos x\,Q + G'_{2p}(x)\sinh x\,Q\cos x\,Q\\ & + G'_{3p}(x)\cosh x\,Q\sin x\,Q + G'_{4p}(x)\sinh x\,Q\sin x\,Q = 0,\\ & G'_{1p}(x)\frac{d}{dx}(\cosh x\,Q\cos x\,Q) + G'_{2p}(x)\frac{d}{dx}(\sinh x\,Q\cos x\,Q)\\ & + G'_{3p}(x)\frac{d}{dx}(\cosh x\,Q\sin x\,Q) + G'_{4p}(x)\frac{d}{dx}(\sinh x\,Q\sin x\,Q) = 0,\\ & G'_{1p}(x)\frac{d^2}{dx^2}(\cosh x\,Q\cos x\,Q) + G'_{2p}(x)\frac{d^2}{dx^2}(\sinh x\,Q\cos x\,Q)\\ & + G'_{3p}(x)\frac{d^2}{dx^2}(\cosh x\,Q\sin x\,Q) + G'_{4p}(x)\frac{d^2}{dx^2}(\sinh x\,Q\sin x\,Q) = 0,\\ & G'_{1p}(x)\frac{d^3}{dx^3}(\cosh x\,Q\cos x\,Q) + G'_{2p}(x)\frac{d^3}{dx^3}(\sinh x\,Q\cos x\,Q)\\ & + G'_{3p}(x)\frac{d^3}{dx^3}(\cosh x\,Q\sin x\,Q) + G'_{4p}(x)\frac{d^3}{dx^3}(\sinh x\,Q\sin x\,Q) = -b_2\frac{d\tau_a}{dx}.\end{aligned} \tag{6c}$$

The expressions for $G_{1p}(x), \ldots, G_{4p}(x)$ are very lengthy and can be found in [Li 2010], and thus are not included here. The solution for the adhesive peel stress in the general butt joint case is given by (again with $Q = \sqrt[4]{b_1/4}$)

$$\begin{aligned}\sigma_a &= \sigma_{aH} + \sigma_{ap}\\ &= C_{1H}\cosh x\,Q\cos x\,Q + C_{2H}\sinh x\,Q\cos x\,Q\\ &\quad + C_{3H}\cosh x\,Q\sin x\,Q + C_{4H}\sinh x\,Q\sin x\,Q\\ &\quad + G_{1p}(x)\cosh x\,Q\cos x\,Q + G_{2p}(x)\sinh x\,Q\cos x\,Q\\ &\quad + G_{3p}(x)\cosh x\,Q\sin x\,Q + G_{4p}(x)\sinh x\,Q\sin x\,Q.\end{aligned} \tag{6d}$$

The expressions for the four constants $C_{1H}, \ldots, C_{4H}$, given in the Appendix, are determined using the boundary conditions

$$\begin{aligned}\left.\frac{d^2\sigma_a}{dx^2}\right|_{x=-c} &= \frac{E_a}{\eta}(k_{12,\mathrm{adh}}T + k_{22,\mathrm{adh}}M_0), & \left.\frac{d^3\sigma_a}{dx^3} + b_2\tau_a\right|_{x=-c} &= \frac{E_a}{\eta}k_{22,\mathrm{adh}}V_0,\\ \left.\frac{d^2\sigma_a}{dx^2}\right|_{x=c} &= -\frac{E_a}{\eta}(k_{12,\mathrm{doub}}T + k_{22,\mathrm{doub}}M_1), & \left.\frac{d^3\sigma_a}{dx^3} + b_2\tau_a\right|_{x=c} &= -\frac{E_a}{\eta}k_{22,\mathrm{doub}}V_1.\end{aligned} \tag{6e}$$

The above four boundary conditions relate the derivatives of adhesive peel stress with the applied loads at the outer and inner overlap edges. Two differentiations are conducted to the peel stress expression in $(1a)_1$ with the aid of the moment-curvature relationship to obtain the first two boundary conditions. One more differentiation is applied to the second derivative of the peel stress expression in $(1a)_1$ with the aid of moment equilibrium relationship to obtain the third and fourth boundary conditions.

Second strategy: adhesive peel stress in the general joint case. As mentioned before, this strategy was initially suggested by Bigwood and Crocombe in 1989. They did not present the associated boundary conditions for exploring the peel stress. To assess the possibility and difficulty in using this strategy, further adhesive stress exploration is conducted in the following.

The uncoupled sixth-order differential equation [Bigwood and Crocombe 1989] for adhesive peel stress can be derived by eliminating adhesive shear stress in $(2a)_2$ as

$$\frac{d^6\sigma_a}{dx^6} + a_1\frac{d^4\sigma_a}{dx^4} + b_1\frac{d^2\sigma_a}{dx^2} + (a_1b_1 - a_2b_2)\sigma_a = 0. \tag{7a}$$

The corresponding characteristic equation becomes

$$\lambda^6 + a_1\lambda^4 + b_1\lambda^2 + (a_1b_1 - a_2b_2) = 0. \tag{7b}$$

Note from the two uncoupled adhesive stress differential equations in (4a) and (7a), that their characteristic equations would have up to six common roots, λ_i ($i = 1$ to 6). One more characteristic root of $\lambda = 0$ exists for the adhesive shear stress.

The general solution for the adhesive peel stress can be established as:

$$\begin{aligned}\sigma_a = {} & C_{p1}\cosh\left(x\sqrt{\gamma_1 - a_1/3}\right) + C_{p2}\sinh\left(x\sqrt{\gamma_1 - a_1/3}\right) \\ & + C_{p3}\cosh\left(x(|\phi|^{\frac{1}{2}}\cos\tfrac{\beta}{2})\right)\cos\left(x(|\phi|^{\frac{1}{2}}\sin\tfrac{\beta}{2})\right) + C_{p4}\sinh\left(x(|\phi|^{\frac{1}{2}}\cos\tfrac{\beta}{2})\right)\cos\left(x(|\phi|^{\frac{1}{2}}\sin\tfrac{\beta}{2})\right) \\ & + C_{p5}\cosh\left(x(|\phi|^{\frac{1}{2}}\cos\tfrac{\beta}{2})\right)\sin\left(x(|\phi|^{\frac{1}{2}}\sin\tfrac{\beta}{2})\right) + C_{p6}\sinh\left(x(|\phi|^{\frac{1}{2}}\cos\tfrac{\beta}{2})\right)\sin\left(x(|\phi|^{\frac{1}{2}}\sin\tfrac{\beta}{2})\right). \quad (7c)\end{aligned}$$

The six integral constants $C_{p1}, \ldots, C_{p6}$ in the general peel stress solution expression may be determined using the following boundary conditions:

$$\begin{aligned} &\int_{-c}^{c}\sigma_a\,dx = V_u|_{x=-c} - V_u|_{x=c} = V_0, && \int_{-c}^{c}\sigma_a x\,dx = -(V_0 c + M_0), \\ &\left.\frac{d^2\sigma_a}{dx^2}\right|_{x=-c} = \frac{E_a}{\eta}(k_{12,\mathrm{adh}}T + k_{22,\mathrm{adh}}M_0), && \left.\frac{d^3\sigma_a}{dx^3} + b_2\tau_a\right|_{x=-c} = \frac{E_a}{\eta}k_{22,\mathrm{adh}}V_0, \quad (7d) \\ &\left.\frac{d^2\sigma_a}{dx^2}\right|_{x=c} = -\frac{E_a}{\eta}(k_{12,\mathrm{doub}}T + k_{22,\mathrm{doub}}M_1), && \left.\frac{d^3\sigma_a}{dx^3} + b_2\tau_a\right|_{x=c} = -\frac{E_a}{\eta}k_{22,\mathrm{doub}}V_1. \end{aligned}$$

Similarly to the explanations of the boundary conditions (5b), the boundary conditions (7d) reflect the joint equilibrium state and internal relationship between the adhesive stresses and the associated laminate moment-curvature at different differentiation levels. The derived six integral constants are given in the Appendix. It can be seen from the derivations that the second strategy would avoid the complex derivations and long expressions required for determining the adhesive peel stress used in the first strategy.

Consistency of the adhesive stresses from the general to special joint cases. The derivations in the closed-form stress solutions were carried out based on their fundamental equations, thus, when the general case approaches the special butt joint case, both the adhesive peel and shear stresses will converge to their corresponding adhesive stresses in the special joint case, which have been validated elsewhere [Li 2010].

Consistency of the adhesive peel stresses between the two solution strategies in general joint case. For clarity and simplicity, numerical examples in Section 4 will be used to demonstrate the consistency.

4. Numerical examples and discussion

A total of six joint conditions were studied: three joint configurations and each with two layup sequences. Each of the selected joints have two identical 50 mm long unbonded outer adherends, a 101.6 mm long doubler including a 0.5 mm long inner section, and two identical 50.55 mm long adhesive layers of 0.17 mm in thickness. A 100 MPa remote tensile stress was applied to the joint adherend.

The 16-ply laminates were used for all the joint adherends. The only difference was the doubler laminates in the three joint configurations. The case 1 joint had identical 16-ply laminates for both the adherend and doubler, which makes it the special joint without a coupling effect between the adhesive peel and shear stresses. The doublers of the case 2 joint were made from 24-ply laminates, and the case 3 joint doublers were made from 32-ply laminates. The two layup sequences were $[45/-45/0/90]_{\mathrm{ns}}$ and $[0/90/45/-45]_{\mathrm{ns}}$ referred to as S1 and S2, respectively. The same layup sequence was used in each joint

laminates. For instance, C1S1 refers the case 1 joint made from the 16-ply $[45/-45/0/90]_{2s}$ laminates; and C2S2 refers the case 2 joint made from the 16-ply $[0/90/45/-45]_{2s}$ laminate adherend and 24-ply $[0/90/45/-45]_{3s}$ laminate doubler, etc. The laminates were generated using 0.14 mm thick carbon fiber laminae, and the lamina material properties were: $E_{11} = 145$ GPa, $E_{22} = 8.9$ GPa, $v_{12} = 0.31$, and $G_{12} = 4.5$ GPa based on our tests.

Determination of the adhesive stresses using the closed-form solutions. The first step is to determine the bending moments and shear forces at the bonded overlap edges as explained in [Li et al. 2011]. Then, according to the laminate layup condition and material properties, the four coefficients, a_1, a_2, b_1, and b_2 from (2b)–(2e) are calculated. Finally, the adhesive stresses are determined using the solutions given in Section 3.

Finite element modeling. To properly set up the lamina orientation in each ply, three-dimensional finite element (FE) models with unit width (1 mm in the y-direction) were generated using MSC.Patran and MSC.Marc version 2010r1. Geometrically nonlinear behavior in the joint deformation under a two-dimensional plane strain condition was analyzed by applying the zero displacement condition, $U_y = 0$, at the two joint side edges over the entire joint length (x-direction). The joint width was in the y-axis direction, and thickness was in the z-direction. As shown in Figure 3, a fine mesh was applied to the

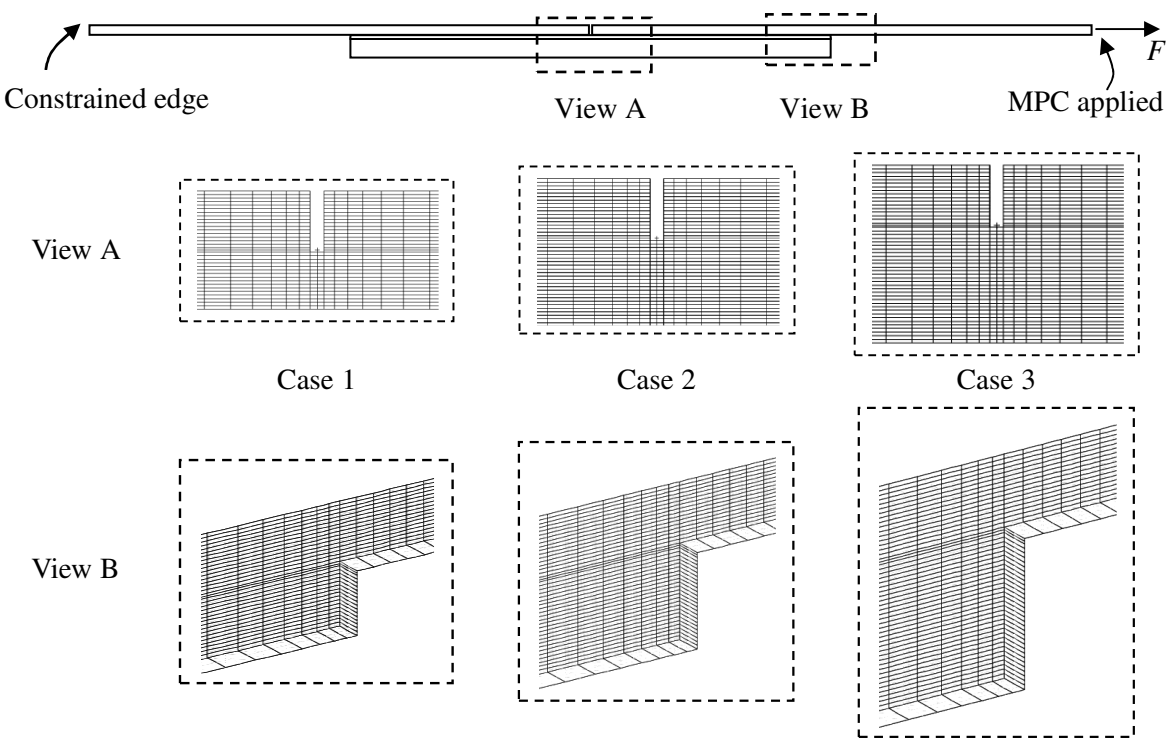

Figure 3. Schematic diagrams for the two simulated butt joints with a 0.5 mm inner gap section for both adherends and adhesive. Case 1: a joint made of identical 16-ply laminates. Case 2: a joint with 16-ply adherend and 24-ply doubler laminates. Case 3: a joint with 16-ply adherend and 32-ply doubler laminates.

overlap edge areas. Two elements were used through the adhesive thickness, while one element was used along the joint unit width as well as in each lamina in the thickness direction. A total of 2,404 twenty-node hexahedron brick elements with 17,561 nodes were created for the special case 1 joint. A total of 2,820 twenty-node hexahedron brick elements with 20,513 nodes were generated for the case 2 joint with the 24-ply doubler. A total of 3,236 twenty-node hexahedron brick elements with 23,465 nodes were generated for the case 3 joint with the 32-ply doubler. The convergence of the adhesive stress value was obtained using the current meshes in the FE models. The left edge was clamped without any displacement in both the horizontal and vertical directions, while the right adherend far end edge was uniformly loaded with a tensile stress of 100 MPa. Multi-point-constrain (MPC) conditions were applied to the right edge nodes ensuring the same displacement during the tensile loading stage. FE analysis results for each pair of nodes, located at the $[x, 0, z]$ and $[x, 1, z]$ positions on the two width side surfaces, were almost identical.

Comparison of the adhesive stresses between the closed-form solutions and FE results. Five nodes were used through the thickness of the adhesive layer. Adhesive stresses at the upper element mid-node (near adherend), adhesive centerline, and lower elements mid-node (near doubler) were extracted and analyzed.

Comparison of the adhesive peel stresses. Variations in the adhesive peel stresses obtained from closed-form solutions and finite element results are presented in Figures 4 to 9 for the three joint cases with two layups. For clarity, close views of the peak stress profiles at the inner bonded overlap edges are plotted. Good correlations were obtained between the theoretical and FE results for all the cases. The following details can be observed:

(1) high stresses are present in the vicinity of the overlap edges, the highest being at the inner overlap edge position;

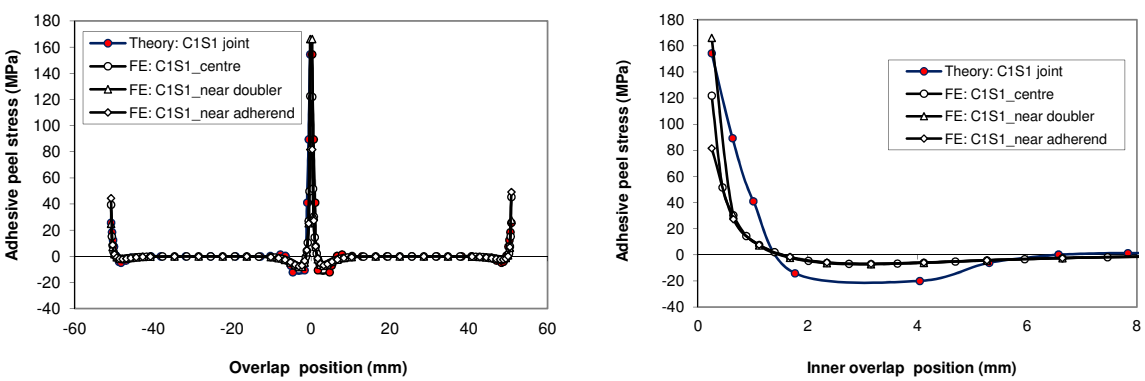

Figure 4. Comparison of the adhesive peel stresses obtained from closed-form solutions and FE results for a special butt C1S1 joint with the identical 16-ply laminates in $[45/-45/0/90]_{2s}$ layup condition. Left: adhesive peel stress profile through the bonded overlap. Right: Peak adhesive peel stress at the inner overlap edge region Here FE: C1S1_near doubler refers to the path along the mid-nodes of the adhesive layer elements adjacent to the doubler. Similar labels apply to the remaining figures.

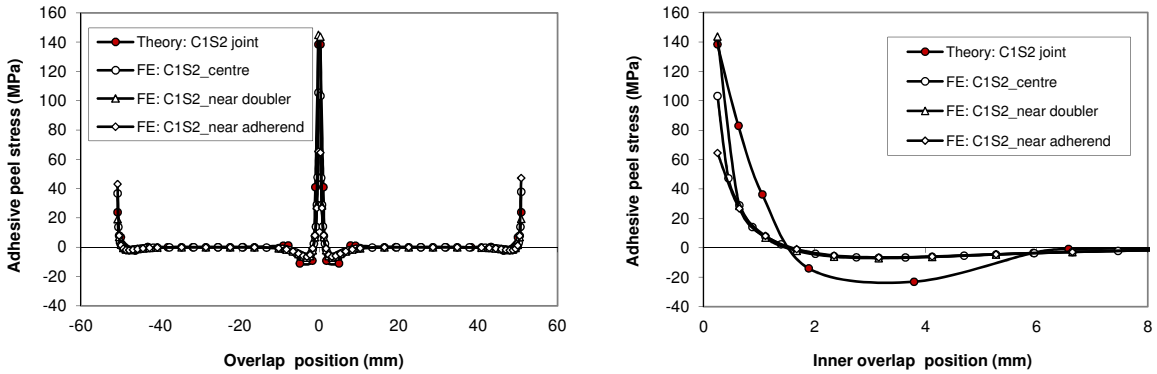

Figure 5. Comparison of the adhesive peel stresses obtained from closed-form solutions and FE results for a special butt C1S2 joint with the identical 16-ply laminates in $[0/90/45/-45]_{2s}$ layup condition.

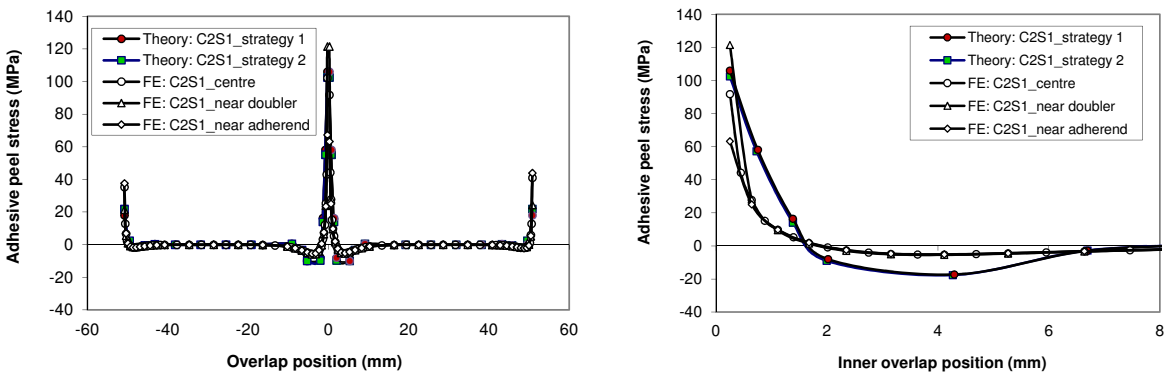

Figure 6. Comparison of the adhesive peel stresses obtained from closed-form solutions and FE results for a special butt C2S1 joint with the 16-ply adherend in $[45/-45/0/90]_{2s}$ layup and 24-ply doubler in $[45/-45/0/90]_{3s}$ layup condition.

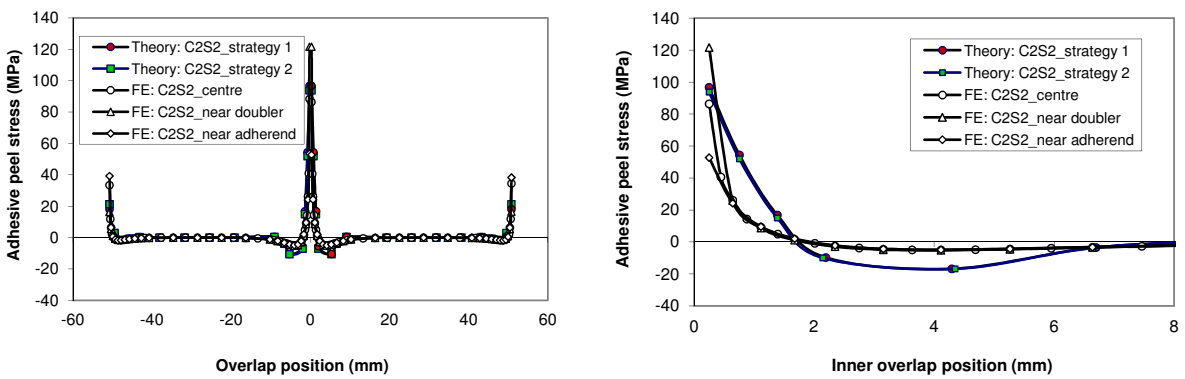

Figure 7. Comparison of the adhesive peel stresses obtained from closed-form solutions and FE results for a special butt C2S2 joint with the 16-ply adherend in $[0/90/45/-45]_{2s}$ layup and 24-ply doubler in $[0/90/45/-45]_{3s}$ layup condition.

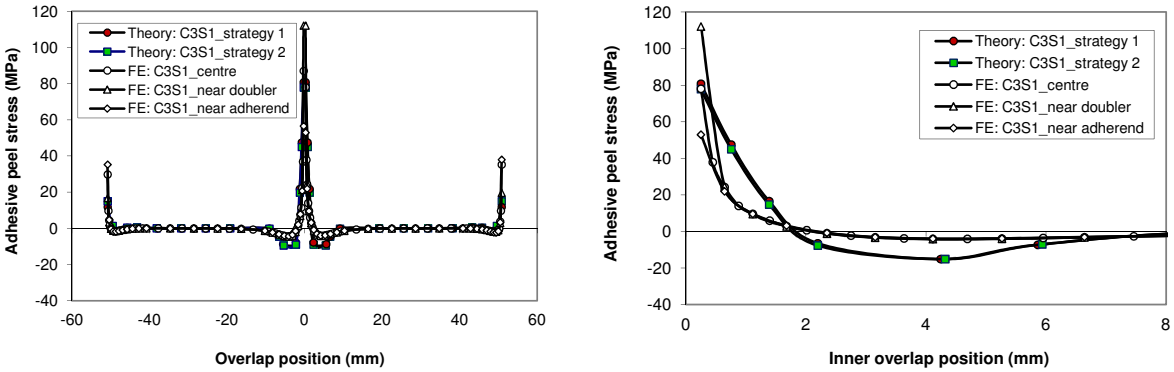

Figure 8. Comparison of the adhesive peel stresses obtained from closed-form solutions and FE results for a special butt C3S1 joint with the 16-ply adherend in $[45/-45/0/90]_{2s}$ layup and 32-ply doubler in $[45/-45/0/90]_{4s}$ layup condition.

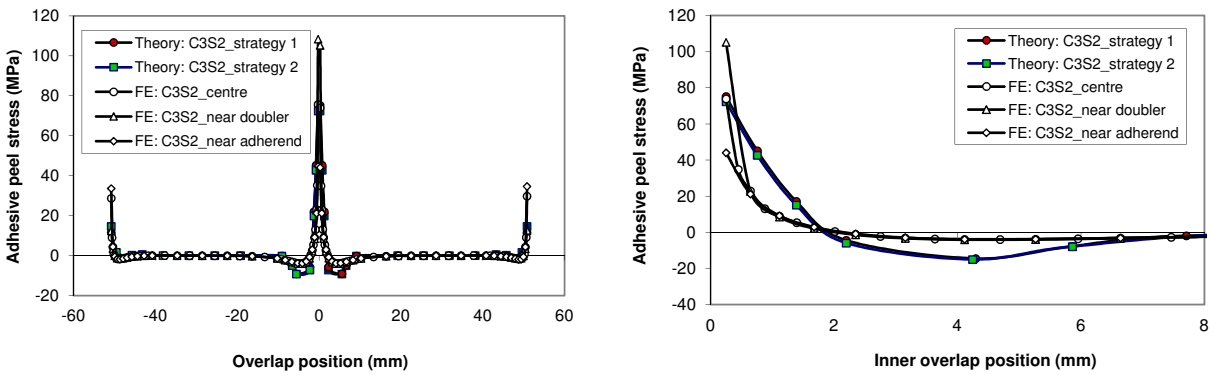

Figure 9. Comparison of the adhesive peel stresses obtained from closed-form solutions and FE results for a special butt C3S2 joint with the 16-ply adherend in $[0/90/45/-45]_{2s}$ layup and 32-ply doubler in $[0/90/45/-45]_{4s}$ layup condition.

(2) the stress magnitudes are lower using the thicker doubler, as well as the S2 layup condition;

(3) consistency in the adhesive peel stress magnitude obtained from the two theoretical strategies is demonstrated;

(4) the theoretical results are approximately the same as the FE results, except at the edge positions; and

(5) at the overlap edge position, the peel stress singularity can be obtained from both the theoretical and FE results with correlated peak stresses.

Comparison of the adhesive shear stresses. Figures 10 to 15 show the adhesive shear stress profiles for the six joint conditions. Both theoretical and FE results show that both the peel and shear stress magnitudes are affected by the doubler thickness and laminate layup condition. The direct reason could be the effective bending stiffness value. The S2 layup laminates have a higher bending stiffness than

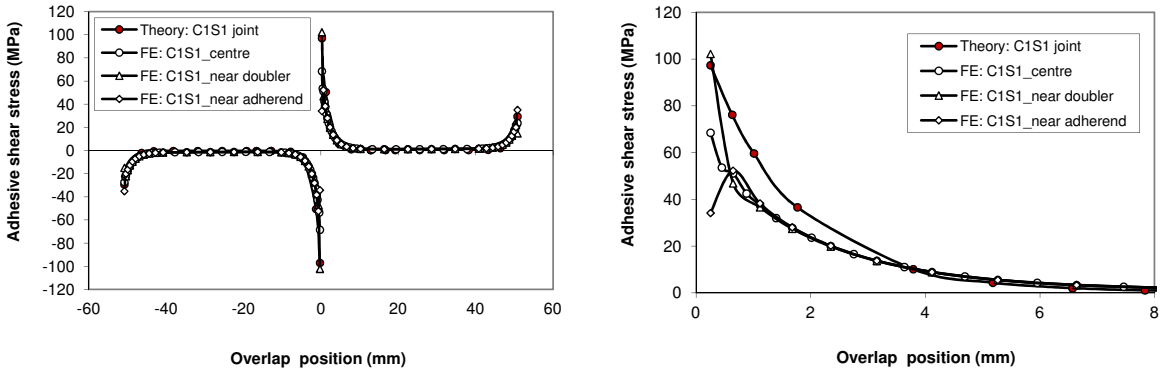

Figure 10. Comparison of the adhesive shear stresses obtained from closed-form solutions and FE results for a special butt C1S1 joint with the identical 16-ply laminates in $[45/-45/0/90]_{2s}$ layup condition.

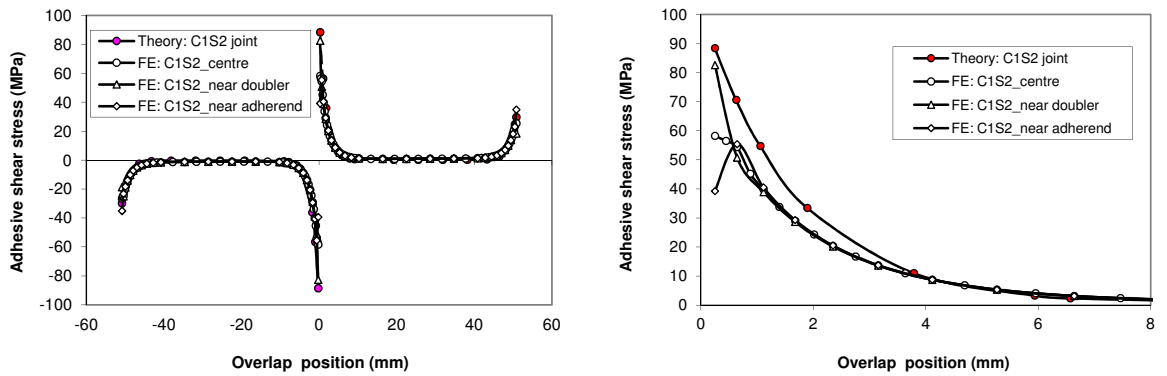

Figure 11. Comparison of the adhesive shear stresses obtained from closed-form solutions and FE results for a special butt C1S2 joint with the identical 16-ply laminates in $[0/90/45/-45]_{2s}$ layup condition.

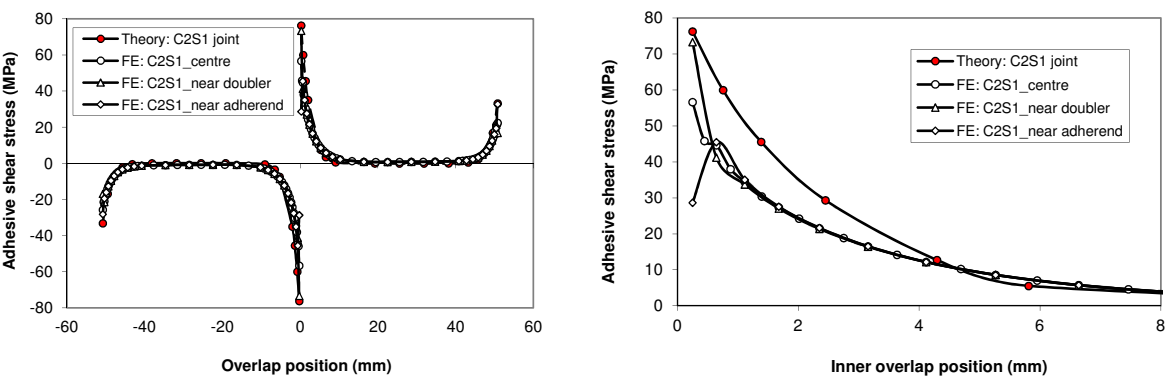

Figure 12. Comparison of the adhesive shear stresses obtained from closed-form solutions and FE results for a special butt C2S1 joint with the 16-ply adherend in $[45/-45/0/90]_{2s}$ layup and 24-ply doubler in $[45/-45/0/90]_{3s}$ layup condition.

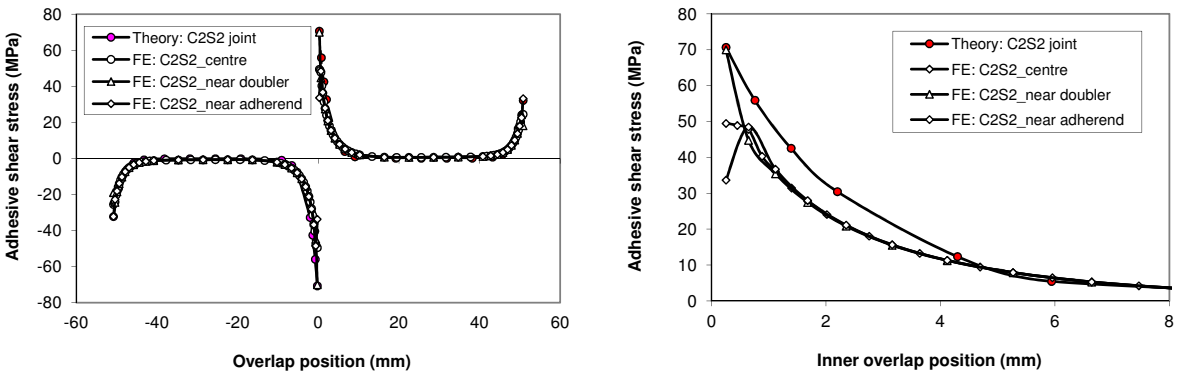

Figure 13. Comparison of the adhesive shear stresses obtained from closed-form solutions and FE results for a special butt C2S2 joint with the 16-ply adherend in $[0/90/45/-45]_{2s}$ layup and 24-ply doubler in $[0/90/45/-45]_{3s}$ layup condition.

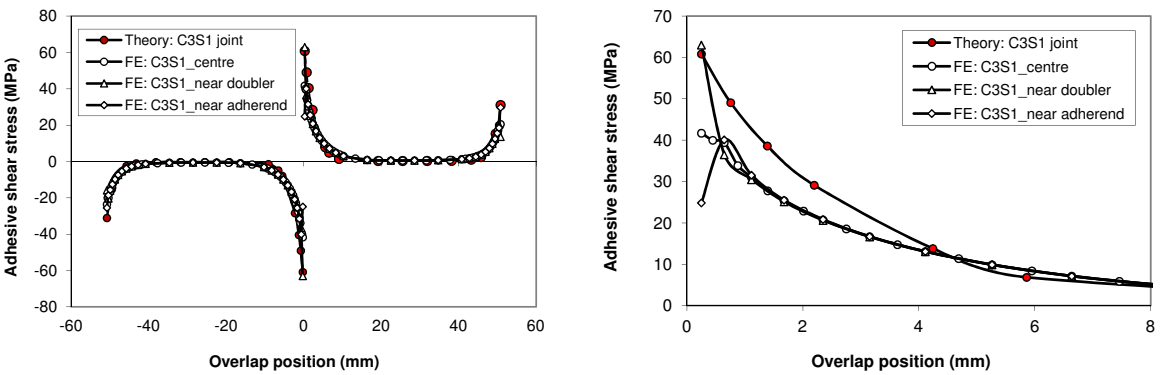

Figure 14. Comparison of the adhesive shear stresses obtained from closed-form solutions and FE results for a special butt C3S1 joint with the 16-ply adherend in $[45/-45/0/90]_{2s}$ layup and 32-ply doubler in $[45/-45/0/90]_{4s}$ layup condition.

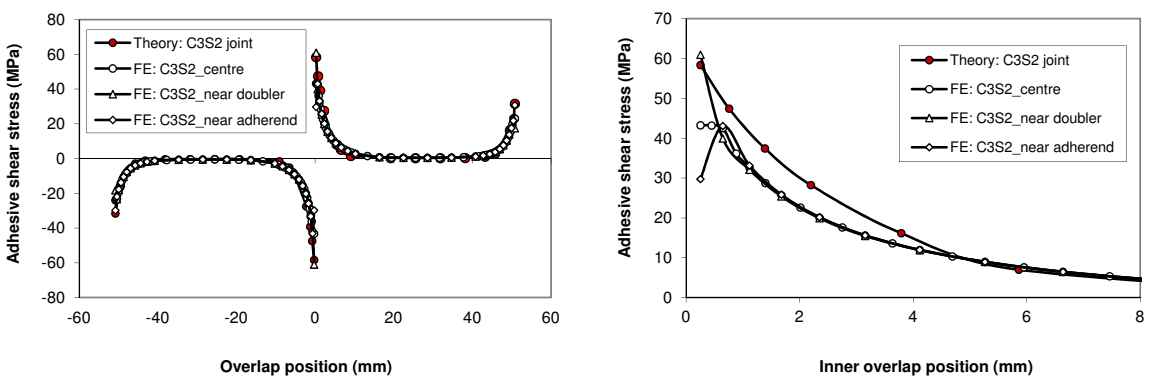

Figure 15. Comparison of the adhesive shear stresses obtained from closed-form solutions and FE results for a special butt C3S2 joint with the 16-ply adherend in $[0/90/45/-45]_{2s}$ layup and 32-ply doubler in $[0/90/45/-45]_{4s}$ layup condition.

the S1 laminates. Small bending deformations would be found in the joint using stiff laminates, and the resulting adhesive stresses magnitude should be small. Due to the shear stress free condition at the two inner adherend edges, the FE results for the adhesive shear stresses at the upper nodes near to the adhesive-adherend interface dropped at the edge positions, as shown in the right-hand portions of Figures 10 through 15. This drop cannot be obtained from the theoretical solutions due to the approximations used in (1a). A study of the correlation between the stress drop and the associated bending stiffness and/or doubler thickness could be carried out using the theoretical solutions, but is not covered in this paper.

The comparisons above clearly show that the closed-form stress solutions are reliable and accurate. The obtained results demonstrate that the current used boundary conditions are adequate. The closed-form stress solutions could be used to analyze the Mode I and Mode II strain energy release rate for cohesive crack propagation behavior or associated delamination in a generic situation of butt joints using the approach as in [Hu 1995; Li et al. 1999]. The adhesive stress profile clearly shows the high stressed area where further appropriate reinforcement work should be made to improve the joint structural integrity.

Factors affecting the adhesive stress magnitude. Typical factors affecting the adhesive stress include the thicknesses in the adherend, doubler, and adhesive, the inner doubler section length (a kind of cohesive crack length at the bonded butt joint mid-position area), the adhesive modulus, the laminate layup condition, etc. The impact of these factors could be investigated using the closed-form solutions, but this is not pursued in this report. To avoid tedious calculations in the adhesive peel stress, strategy 2 is recommended, since both strategies give almost identical peel stress results.

5. Conclusions

(1) Closed-form adhesive stress solutions were obtained for the bonded composite single-strap butt joint. Strategy 2 would lead to a relative concise peel stress expression, as compared to the strategy 1. Generally, the integration constants in the closed-form adhesive stress solutions are quite long and complex, which is acceptable for such a complicated analysis of high order differential equations. The theoretical solution can be applied to the unbalanced composite single-lap joints, because the single-strap butt joint actually consists of two unbalanced single-lap joints. The complete theoretical solution can be the solid base for further development of simplified stress solutions for better practical applications of composite joint in the near future.

(2) A total of six joint conditions: three joint configurations, each having two different layup sequences in laminates, were studied theoretically and numerically for demonstrating the theoretical correctness. Three-dimensional finite element models using twenty-node brick elements were created for the unit-width joints deformation analysis under plane strain condition.

(3) Consistency in the predicted adhesive peel stresses were demonstrated using the two theoretical strategies; the small difference observed could be attributed to numerical error in the lengthy, complex, and sensitive terms in the closed-form solutions.

(4) Good agreement was obtained in all the associated stress comparisons obtained from the theoretical and numerical results. High peak stress exists at the bonded overlap edges, with higher magnitude at the inner overlap edge.

(5) Effects of doubler bending stiffness (e.g., thickness) and laminate layup sequence on the adhesive stress magnitude were revealed by both theoretical and numerical results. The thicker doubler led to the smaller peak stress magnitudes. Similarly, two used layup sequences, which had different laminate bending stiffness, also had different adhesive stress magnitudes. For instance, the bending stiffness of the S1 $[45/-45/0/90]_{ns}$ laminates would be approximately 80% of the S2 $[0/90/45/-45]_{ns}$ laminates, and the corresponding stress magnitudes for both peel and shear stresses are smaller in the S1 joints than the S2 joints, at a lesser degree. A practical evaluation of the adhesive stress profile under the influence of each joint component can be easily carried out using the obtained closed-form solutions, with the aid of an Excel spreadsheet tool.

(6) The closed-form solutions would provide the insightful assessment to identify the proper hole positions for introducing extra fasteners to fabricate a strong hybrid attached, bonded-bolted, composite joint. In addition, extra strengthening should be applied to the geometrical transition areas, especially the inner overlap edge region to ensure structural integrity.

Acknowledgements

The full support from the Institute for Aerospace Research (IAR) is acknowledged and greatly appreciated. Many thanks to those people who have, in one way or another, contributed to this work.

Appendix: Expressions for relevant parameters in adhesive stresses

Effective parameters in laminated composite beam analysis [Li et al. 2011]. For the classic Euler–Bernoulli beam with no transverse loads, the in-plane laminate constitutive relationship simplifies to

$$\begin{bmatrix} \epsilon_x^0 \\ \kappa_x \end{bmatrix} = \begin{bmatrix} k_{11} & k_{12} \\ k_{12} & k_{22} \end{bmatrix} \begin{bmatrix} N_x \\ M_x \end{bmatrix}. \tag{A.1a}$$

Under the cylindrical bending laminate condition (the plane strain condition), the deformation of the laminate is a function of its axial position x, with the terms, ϵ_x^0, κ_y, and κ_{xy} equal to zero. Thus, the in-plane mid-plane strain and curvature can be determined as:

$$\begin{bmatrix} \epsilon_x^0 \\ \gamma_{xy}^0 \\ \kappa_x \end{bmatrix} = \begin{bmatrix} A_{11} & A_{16} & B_{11} \\ A_{16} & A_{66} & B_{16} \\ B_{11} & B_{16} & D_{11} \end{bmatrix}^{-1} \begin{bmatrix} N_x \\ N_{xy} \\ M_x \end{bmatrix}, \tag{A.1b}$$

where A_{ij}, B_{ij}, and D_{ij} are elements in the stiffness (**ABD**) matrix of the laminate constitutive equation; N_x, N_{xy}, and M_x are unit-width in-plane forces and moments.

The in-plane shear force N_{xy} is equal to zero in this bending situation; hence, (A.1b) becomes

$$\begin{bmatrix} \epsilon_x^0 \\ \kappa_x \end{bmatrix} = \frac{\begin{bmatrix} A_{66}D_{11} - B_{16}^2 & A_{16}B_{16} - A_{66}B_{11} \\ A_{16}B_{16} - A_{66}B_{11} & A_{11}A_{66} - A_{16}^2 \end{bmatrix} \begin{bmatrix} N_x \\ M_x \end{bmatrix}}{A_{11}(A_{66}D_{11} - B_{16}^2) + 2A_{16}B_{11}B_{16} - D_{11}A_{16}^2 - A_{66}B_{11}^2}. \tag{A.1c}$$

The corresponding k_{ij} term can be determined by comparing (A.1a) and (A.1b). The effective Young's modulus and bending stiffness are

$$E_{xx} = \frac{1}{t(A_{66}D_{11} - B_{16}^2)}\big(A_{11}(A_{66}D_{11} - B_{16}^2) + 2A_{16}B_{11}B_{16} - D_{11}A_{16}^2 - A_{66}B_{11}^2\big), \tag{A.1d}$$

$$D_x = (EI)_{xx} = \frac{1}{(A_{11}A_{66} - A_{16}^2)}\big(D_{11}(A_{11}A_{66} - A_{16}^2) + 2A_{16}B_{11}B_{16} - A_{11}B_{16}^2 - A_{66}B_{11}^2\big), \tag{A.1e}$$

where t is the laminate thickness. When the laminate is symmetrical and balanced, $B_{ij} = 0$ and $A_{16} = A_{26} = 0$. The effective parameters, E_{xx} and D_x, can be further simplified as:

$$E_{xx} = \frac{1}{tk_{11}} = \frac{A_{11}}{t}, \quad D_x = (EI)_{xx} = \frac{M_x}{\kappa_x} = D_{11}. \tag{A.1f}$$

Integral constants for adhesive shear stresses (3c) and adhesive peel stresses (3e) in the special joint case. Let $Q = \sqrt[4]{b_1/4}$. Then

$$\begin{aligned}
C_{0S} &= \tfrac{1}{c}\bigg(-\frac{T}{2} + \frac{k_{11}T + \frac{1}{4}tk_{22}(M_0 - M_1)}{2k_{11} + \frac{1}{2}t^2k_{22}}\bigg),\\
C_{1S} &= \frac{\frac{G_a}{\eta}(-k_{11}T + \frac{1}{4}tk_{22}(M_1 - M_0))}{\sqrt{-a_1}\sinh(c\sqrt{-a_1})}, \quad C_{2S} = \frac{\frac{G_a}{\eta}\frac{1}{4}tk_{22}(M_0 + M_1)}{\sqrt{-a_1}\cosh(c\sqrt{-a_1})};\\
C_{3S} &= \frac{\frac{E_a}{2\eta}k_{22}\cosh c\,Q\cos c\,Q\left(\frac{V_0+V_1}{Q^3} + \frac{M_0-M_1}{Q^2}(\tanh c\,Q - \tan c\,Q)\right)}{\sinh 2c\,Q + \sin 2c\,Q},\\
C_{4S} &= \frac{\frac{E_a}{2\eta}k_{22}\sinh c\,Q\cos c\,Q\left(\frac{V_0-V_1}{Q^3} + \frac{M_0+M_1}{Q^2}\left(\frac{1}{\tanh c\,Q} - \tan c\,Q\right)\right)}{\sin 2c\,Q - \sinh 2c\,Q},\\
C_{5S} &= \frac{\frac{E_a}{2\eta}k_{22}\cosh c\,Q\sin c\,Q\left(\frac{V_0-V_1}{Q^3} + \frac{M_0+M_1}{Q^2}\left(\tanh c\,Q + \frac{1}{\tan c\,Q}\right)\right)}{\sin 2c\,Q - \sinh 2c\,Q},\\
C_{6S} &= \frac{\frac{E_a}{2\eta}k_{22}\sinh c\,Q\sin c\,Q\left(\frac{V_0+V_1}{Q^3} + \frac{M_0-M_1}{Q^2}\left(\frac{1}{\tanh c\,Q} + \frac{1}{\tan c\,Q}\right)\right)}{\sin 2c\,Q + \sinh 2c\,Q}.
\end{aligned} \tag{A.2a, A.2b}$$

Adhesive shear stress solution in the general joint case. The details on the derivation of the seven λ roots can be found from the [Li 2010]. They are

$$\lambda_0 = 0, \quad \lambda_{1,2} = \pm\sqrt{\gamma_1 - \tfrac{a_1}{3}}, \quad \lambda_{3,4} = \pm|\phi|^{\frac{1}{2}}\big(\cos\tfrac{\beta}{2} + i\sin\tfrac{\beta}{2}\big), \quad \lambda_{5,6} = \pm|\phi|^{\frac{1}{2}}\big(\cos\tfrac{\beta}{2} - i\sin\tfrac{\beta}{2}\big), \tag{A.3a}$$

where

$$\gamma_1 = \sqrt[3]{-\tfrac{q}{2} + \sqrt{\big(\tfrac{q}{2}\big)^2 + \big(\tfrac{p}{3}\big)^3}} + \sqrt[3]{-\tfrac{q}{2} - \sqrt{\big(\tfrac{q}{2}\big)^2 + \big(\tfrac{p}{3}\big)^3}}, \quad p = b_1 - \frac{a_1^2}{3}, \quad q = \frac{2a_1^3}{27} + \frac{2a_1b_1}{3} - a_2b_2$$

$$|\phi| = \sqrt{\left(-\tfrac{\gamma_1}{2} - \tfrac{a_1}{3}\right)^2 + \tfrac{3}{4}\left(\sqrt[3]{-\tfrac{q}{2} + \sqrt{\left(\tfrac{q}{2}\right)^2 + \left(\tfrac{p}{3}\right)^3}} + \sqrt[3]{\tfrac{q}{2} + \sqrt{\left(\tfrac{q}{2}\right)^2 + \left(\tfrac{p}{3}\right)^3}}\right)^2}, \quad \beta = \min\{\beta_1, \beta_2\}.$$

The angles β_1 and β_2 are defined within the 0 to 2π range. The sum of the two angles is 2π. The angles are measured in radians and positive in the counterclockwise sense. For instance, if the angle β_1 is within the range 0 to $\pi/2$, the angles can be calculated to be

$$\beta_1 = \arctan \frac{\frac{\sqrt{3}}{2}\left(\sqrt[3]{-\frac{q}{2} + \sqrt{\left(\frac{q}{2}\right)^2 + \left(\frac{p}{3}\right)^3}} + \sqrt[3]{\frac{q}{2} + \sqrt{\left(\frac{q}{2}\right)^2 + \left(\frac{p}{3}\right)^3}}\right)}{-\frac{\gamma_1}{2} - \frac{a_1}{3}}, \quad \beta_2 = 2\pi - \beta_1. \tag{A.3b}$$

Expression of the adhesive shear stress in (5a). Details on the derivation of the following parameters, integral constants and functions can be found in [Li 2010]. Only the final expressions are provided in the following.

Submitting the shear stress from (5a) into the boundary conditions (5b), seven simultaneous equations written in terms of the seven constants $C_0, \ldots, C_6$ are obtained:

$$\begin{aligned}
C_0 c + C_1 C_{10} + C_3 C_{30} + C_6 C_{60} &= f_0,\\
-C_1 C_{11} + C_2 C_{21} - C_3 C_{31} + C_4 C_{41} + C_5 C_{51} - C_6 C_{61} &= f_1,\\
C_1 C_{11} + C_2 C_{21} + C_3 C_{31} + C_4 C_{41} + C_5 C_{51} + C_6 C_{61} &= f_2,\\
a_1 C_0 + C_1 C_{12} - C_2 C_{22} + C_3 C_{32} - C_4 C_{42} - C_5 C_{52} + C_6 C_{62} &= f_3,\\
a_1 C_0 + C_1 C_{12} + C_2 C_{22} + C_3 C_{32} + C_4 C_{42} + C_5 C_{52} + C_6 C_{62} &= f_4,\\
-C_1 C_{13} + C_2 C_{23} - C_3 C_{33} + C_4 C_{43} + C_5 C_{53} - C_6 C_{63} &= f_5,\\
C_1 C_{13} + C_2 C_{23} + C_3 C_{33} + C_4 C_{43} + C_5 C_{53} + C_6 C_{63} &= f_6.
\end{aligned} \tag{A.3c}$$

The coefficients C_{ij} in (A.3c) are presented in [Li 2010]; they are omitted here for brevity. The final expressions for the seven constants are

$$C_6 = \frac{\frac{f_3+f_4}{2} - f_0\frac{a_1}{c} + \frac{f_1-f_2}{2}\frac{C_{12}-C_{10}\frac{a_1}{c}}{C_{11}} - \left(\frac{f_6-f_5}{2} + \frac{f_1-f_2}{2}\frac{C_{13}}{C_{11}}\right)\frac{C_{32}-\frac{a_1}{c}C_{30}-\frac{C_{31}}{C_{11}}\left(C_{12}-C_{10}\frac{a_1}{c}\right)}{C_{33}-C_{31}C_{13}/C_{11}}}{C_{62}-\frac{a_1}{c}C_{60}-C_{61}\frac{C_{12}-C_{10}\frac{a_1}{c}}{C_{11}} - \left(C_{63}-C_{61}\frac{C_{13}}{C_{11}}\right)\frac{C_{32}-\frac{a_1}{c}C_{30}-\frac{C_{31}}{C_{11}}\left(C_{12}-C_{10}\frac{a_1}{c}\right)}{C_{33}-C_{31}C_{13}/C_{11}}},$$

$$C_5 = \frac{\frac{f_5+f_6}{2} - \frac{f_1+f_2}{2}\frac{C_{23}}{C_{21}} - \left(\frac{f_4-f_3}{2} - \frac{f_1+f_2}{2}\frac{C_{22}}{C_{21}}\right)\frac{C_{43}-C_{41}C_{23}/C_{21}}{C_{42}-C_{41}C_{22}/C_{21}}}{C_{53}-C_{51}\frac{C_{23}}{C_{21}} - \left(C_{52}-C_{51}\frac{C_{22}}{C_{21}}\right)\frac{C_{43}-C_{41}C_{23}/C_{21}}{C_{42}-C_{41}C_{22}/C_{21}}},$$

$$C_4 = \frac{1}{C_{42}-C_{41}C_{22}/C_{21}}\left(\frac{f_4-f_3}{2} - \frac{f_1+f_2}{2}\frac{C_{22}}{C_{21}} - C_5\left(C_{52}-C_{51}\frac{C_{22}}{C_{21}}\right)\right),$$

$$C_3 = \frac{1}{C_{33}-C_{31}C_{13}/C_{11}}\left(\frac{f_6-f_5}{2} + \frac{f_1-f_2}{2}\frac{C_{13}}{C_{11}} - C_6\left(C_{63}-C_{61}\frac{C_{13}}{C_{11}}\right)\right),$$

$$C_2 = \frac{1}{C_{21}}\Big(\frac{f_1+f_2}{2} - C_{41}C_4 - C_{51}C_5\Big),$$
$$C_1 = -\frac{1}{C_{11}}\Big(\frac{f_1-f_2}{2} + C_{31}C_3 + C_{61}C_6\Big),$$
$$C_0 = \frac{1}{c}(f_0 - C_{10}C_1 - C_{30}C_3 - C_{60}C_6),$$

where

$$f_0 = -T/2,$$
$$f_1 = \frac{G_a}{\eta}\big((k_{11,\mathrm{adh}} + \tfrac{1}{2}t_1k_{12,\mathrm{adh}})T + (k_{12,\mathrm{adh}} + \tfrac{1}{2}t_1k_{22,\mathrm{adh}})M_0\big),$$
$$f_2 = \frac{G_a}{\eta}\big((-k_{11,\mathrm{doub}} + \tfrac{1}{2}t_2k_{12,\mathrm{doub}})T + (-k_{12,\mathrm{doub}} + \tfrac{1}{2}t_2k_{22,\mathrm{doub}})M_1\big),$$
$$f_3 = \frac{G_a}{\eta}(k_{12,\mathrm{adh}} + \tfrac{1}{2}t_1k_{22,\mathrm{adh}})V_0, \qquad f_4 = \frac{G_a}{\eta}(-k_{12,\mathrm{doub}} + \tfrac{1}{2}t_2k_{22,\mathrm{doub}})V_1,$$
$$f_5 = -a_2\frac{E_a}{\eta}(k_{12,\mathrm{adh}}T + k_{22,\mathrm{adh}}M_0), \quad f_6 = a_2\frac{E_a}{\eta}(k_{12,\mathrm{doub}}T + k_{22,\mathrm{doub}}M_1).$$

Expression of the adhesive peel stress using the first strategy. Let $Q = \sqrt[4]{b_1/4}$. The four constants in (6a) and (6d) are

$$C_{1H} = \frac{\frac{E_a}{2\eta}\cosh cQ\cos cQ\left(\frac{k_{22,\mathrm{adh}}V_0 + k_{22,\mathrm{doub}}V_1}{Q^3} + \frac{k_{12}^-T + k_{22,\mathrm{adh}}M_0 - k_{22,\mathrm{doub}}M_1}{Q^2}(\tanh cQ - \tan cQ)\right)}{\sinh 2cQ + \sin 2cQ}$$
$$- \frac{\cosh cQ\cos cQ}{2(\sinh 2cQ + \sin 2cQ)}\frac{b_2(\tau_a(-c) - \tau_a(c))}{Q^3} + H_1,$$

$$C_{2H} = \frac{\frac{E_a}{2\eta}\sinh cQ\cos cQ\left(\frac{k_{22,\mathrm{adh}}V_0 - k_{22,\mathrm{doub}}V_1}{Q^3} + \frac{k_{12}^+T + k_{22,\mathrm{adh}}M_0 + k_{22,\mathrm{doub}}M_1}{Q^2}\left(\frac{1}{\tanh cQ} - \tan cQ\right)\right)}{\sin 2cQ - \sinh 2cQ}$$
$$+ \frac{\sinh cQ\cos cQ}{2(\sin 2cQ - \sinh 2cQ)}\frac{b_2(\tau_a(-c) + \tau_a(c))}{Q^3} + H_2,$$

$$C_{3H} = \frac{\frac{E_a}{2\eta}\cosh cQ\sin cQ\left(\frac{k_{22,\mathrm{adh}}V_0 - k_{22,\mathrm{doub}}V_1}{Q^3} + \frac{k_{12}^+T + k_{22,\mathrm{adh}}M_0 + k_{22,\mathrm{doub}}M_1}{Q^2}\left(\tanh cQ + \frac{1}{\tan cQ}\right)\right)}{\sin 2cQ - \sinh 2cQ} \tag{A.4}$$
$$+ \frac{\cosh cQ\sin cQ}{2(\sinh 2cQ - \sin 2cQ)}\frac{b_2(\tau_a(-c) + \tau_a(c))}{Q^3} + H_3,$$

$$C_{4H} = \frac{\frac{E_a}{2\eta}\sinh cQ\sin cQ\left(\frac{k_{22,\mathrm{adh}}V_0 + k_{22,\mathrm{doub}}V_1}{Q^3} + \frac{k_{12}^-T + k_{22,\mathrm{adh}}M_0 - k_{22,\mathrm{doub}}M_1}{Q^2}\left(\frac{1}{\tanh cQ} + \frac{1}{\tan cQ}\right)\right)}{\sin 2cQ + \sinh 2cQ}$$
$$- \frac{\sinh cQ\sin cQ}{(\sin 2cQ + \sinh 2cQ)}\frac{b_2(\tau_a(-c) - \tau_a(c))}{Q^3} + H_4,$$

where

$$k_{12}^{+} = k_{12,\mathrm{adh}} + k_{12,\mathrm{doub}}, \quad k_{12}^{-} = k_{12,\mathrm{adh}} - k_{12,\mathrm{doub}},$$

$$H_1 = -\tfrac{1}{2}\big(G_{1p}(-c) + G_{1p}(c)\big) + \frac{\cosh^2 c\,Q\big(G_{2p}(-c) - G_{2p}(c)\big)}{\sinh 2c\,Q + \sin 2c\,Q} - \frac{\cos^2 c\,Q\big(G_{3p}(-c) - G_{3p}(c)\big)}{\sinh 2c\,Q + \sin 2c\,Q},$$

$$H_2 = \frac{\sinh^2 c\,Q\big(G_{1p}(-c) - G_{1p}(c)\big)}{\sinh 2c\,Q - \sin 2c\,Q} - \tfrac{1}{2}\big(G_{2p}(-c) + G_{2p}(c)\big) + \frac{\cos^2 c\,Q\big(G_{4p}(-c) - G_{4p}(c)\big)}{\sinh 2c\,Q - \sin 2c\,Q},$$

$$H_3 = \frac{\sin^2 c\,Q\big(G_{1p}(-c) - G_{1p}(c)\big)}{\sinh 2c\,Q - \sin 2c\,Q} - \tfrac{1}{2}\big(G_{3p}(-c) + G_{3p}(c)\big) + \frac{\cosh^2 c\,Q\big(G_{4p}(-c) - G_{4p}(c)\big)}{\sinh 2c\,Q - \sin 2c\,Q},$$

$$H_4 = -\frac{\sin^2 c\,Q\big(G_{2p}(-c) - G_{2p}(c)\big)}{\sinh 2c\,Q + \sin 2c\,Q} + \frac{\sinh^2 c\,Q\big(G_{3p}(-c) - G_{3p}(c)\big)}{\sinh 2c\,Q + \sin 2c\,Q} - \tfrac{1}{2}\big(G_{4p}(-c) + G_{4p}(c)\big).$$

The six integral constants in the adhesive peel stress expression using the second strategy. Submitting the peel stress from (7c) into the boundary conditions Equation (7d), six simultaneous equations written in terms of the six constants $C_{p1}, \ldots, C_{p6}$ can be obtained:

$$\begin{aligned}
C_{p1}I_{11} + C_{p3}I_{31} + C_{p6}I_{61} &= g_1,\\
C_{p2}I_{22} + C_{p4}I_{42} + C_{p5}I_{52} &= g_2,\\
C_{p1}I_{13} - C_{p2}I_{23} + C_{p3}I_{33} - C_{p4}I_{43} - C_{p5}I_{53} + C_{p6}I_{63} &= g_3,\\
C_{p1}I_{13} + C_{p2}I_{23} + C_{p3}I_{33} + C_{p4}I_{43} + C_{p5}I_{53} + C_{p6}I_{63} &= g_4,\\
-C_{p1}I_{14} + C_{p2}I_{24} - C_{p3}I_{34} + C_{p4}I_{44} + C_{p5}I_{54} - C_{p6}I_{64} &= g_5,\\
C_{p1}I_{14} + C_{p2}I_{24} + C_{p3}I_{34} + C_{p4}I_{44} + C_{p5}I_{54} + C_{p6}I_{64} &= g_6.
\end{aligned} \tag{A.5a}$$

The final expressions for the six constants are

$$C_{p6} = \frac{\dfrac{g_5 - g_6}{2} + g_1\dfrac{I_{14}}{I_{11}} + \Big(\dfrac{g_3 + g_4}{2} - g_1\dfrac{I_{13}}{I_{11}}\Big)\dfrac{I_{11}I_{34} - I_{31}I_{14}}{I_{11}I_{33} - I_{31}I_{13}}}{-I_{64} + I_{61}\dfrac{I_{14}}{I_{11}} + \Big(I_{63} - I_{61}\dfrac{I_{13}}{I_{11}}\Big)\dfrac{I_{11}I_{34} - I_{31}I_{14}}{I_{11}I_{33} - I_{31}I_{13}}},$$

$$C_{p5} = \frac{\dfrac{g_5 + g_6}{2} - g_2\dfrac{I_{24}}{I_{22}} - \Big(\dfrac{g_4 - g_3}{2} - g_2\dfrac{I_{23}}{I_{22}}\Big)\dfrac{I_{22}I_{44} - I_{42}I_{24}}{I_{22}I_{43} - I_{42}I_{23}}}{I_{54} - I_{52}\dfrac{I_{24}}{I_{22}} - \Big(I_{53} - I_{52}\dfrac{I_{23}}{I_{22}}\Big)\dfrac{I_{22}I_{44} - I_{42}I_{24}}{I_{22}I_{43} - I_{42}I_{23}}},$$

$$C_{p4} = \frac{\dfrac{g_4 - g_3}{2} - g_2\dfrac{I_{23}}{I_{22}} - C_{p5}\Big(I_{53} - I_{52}\dfrac{I_{23}}{I_{22}}\Big)}{I_{43} - I_{42}\dfrac{I_{23}}{I_{22}}},$$

$$C_{p3} = \frac{\frac{g_3+g_4}{2} - g_1\frac{I_{13}}{I_{11}} - C_{p6}\big(I_{63} - I_{61}\frac{I_{13}}{I_{11}}\big)}{I_{33} - I_{31}\frac{I_{13}}{I_{11}}},$$

$$C_{p2} = \frac{1}{I_{22}}(g_2 - C_{p4}I_{42} - C_{p5}I_{52}), \quad C_{p1} = \frac{1}{I_{11}}(g_1 - C_{p3}I_{31} - C_{p6}I_{61}).$$

where

$$g_1 = \frac{V_0}{2}, \quad g_2 = -\frac{cV_0+M_0}{2}, \quad g_3 = \frac{E_a}{\eta}(k_{12,\mathrm{adh}}T + k_{22,\mathrm{adh}}M_0), \quad g_4 = -\frac{E_a}{\eta}(k_{12,\mathrm{doub}}T + k_{22,\mathrm{doub}}M_1),$$

$$g_5 = \frac{E_a}{\eta}k_{22,\mathrm{adh}}V_0 - b_2\tau_a|_{x=-c}, \quad g_6 = -\frac{E_a}{\eta}k_{22,\mathrm{doub}}V_1 - b_2\tau_a|_{x=c},$$

$$I_{11} = C_{10} = \frac{\sinh c\sqrt{\gamma_1 - a_1/3}}{\sqrt{\gamma_1 - a_1/3}},$$

$$I_{31} = C_{30} = \sin\tfrac{\beta}{2}|\phi|^{-\frac{1}{2}}\big(\cosh\big(c|\phi|^{\frac{1}{2}}\cos\tfrac{\beta}{2}\big)\sin\big(c|\phi|^{\frac{1}{2}}\sin\tfrac{\beta}{2}\big) + \cot\tfrac{\beta}{2}\sinh\big(c|\phi|^{\frac{1}{2}}\cos\tfrac{\beta}{2}\big)\cos\big(c|\phi|^{\frac{1}{2}}\sin\tfrac{\beta}{2}\big)\big),$$

$$I_{61} = C_{60} = \sin\tfrac{\beta}{2}|\phi|^{-\frac{1}{2}}\big(-\sinh\big(c|\phi|^{\frac{1}{2}}\cos\tfrac{\beta}{2}\big)\cos\big(c|\phi|^{\frac{1}{2}}\sin\tfrac{\beta}{2}\big) + \cot\tfrac{\beta}{2}\cosh\big(c|\phi|^{\frac{1}{2}}\cos\tfrac{\beta}{2}\big)\sin\big(c|\phi|^{\frac{1}{2}}\sin\tfrac{\beta}{2}\big)\big),$$

$$I_{22} = \frac{c}{\sqrt{\gamma_1 - a_1/3}}\cosh c\sqrt{\gamma_1 - a_1/3} - \frac{1}{\gamma_1 - a_1/3}\sinh c\sqrt{\gamma_1 - a_1/3},$$

$$\begin{aligned} I_{42} = {} & c\sin\tfrac{\beta}{2}|\phi|^{-\frac{1}{2}}\sinh\big(c|\phi|^{\frac{1}{2}}\cos\tfrac{\beta}{2}\big)\sin\big(c|\phi|^{\frac{1}{2}}\sin\tfrac{\beta}{2}\big) + c\cos\tfrac{\beta}{2}|\phi|^{-\frac{1}{2}}\cosh\big(c|\phi|^{\frac{1}{2}}\cos\tfrac{\beta}{2}\big)\cos\big(c|\phi|^{\frac{1}{2}}\sin\tfrac{\beta}{2}\big) \\ & - \sin\tfrac{\beta}{2}|\phi|^{-1}\cosh\big(c|\phi|^{\frac{1}{2}}\cos\tfrac{\beta}{2}\big)\sin\big(c|\phi|^{\frac{1}{2}}\sin\tfrac{\beta}{2}\big) - \cos\tfrac{\beta}{2}|\phi|^{-1}\sinh\big(c|\phi|^{\frac{1}{2}}\cos\tfrac{\beta}{2}\big)\cos\big(c|\phi|^{\frac{1}{2}}\sin\tfrac{\beta}{2}\big), \end{aligned}$$

$$\begin{aligned} I_{52} = {} & c\cos\tfrac{\beta}{2}|\phi|^{-\frac{1}{2}}\sinh\big(c|\phi|^{\frac{1}{2}}\cos\tfrac{\beta}{2}\big)\sin\big(c|\phi|^{\frac{1}{2}}\sin\tfrac{\beta}{2}\big) - c\sin\tfrac{\beta}{2}|\phi|^{-\frac{1}{2}}\cosh\big(c|\phi|^{\frac{1}{2}}\cos\tfrac{\beta}{2}\big)\cos\big(c|\phi|^{\frac{1}{2}}\sin\tfrac{\beta}{2}\big) \\ & + \cos\tfrac{\beta}{2}|\phi|^{-1}\cosh\big(c|\phi|^{\frac{1}{2}}\cos\tfrac{\beta}{2}\big)\sin\big(c|\phi|^{\frac{1}{2}}\sin\tfrac{\beta}{2}\big) + \sin\tfrac{\beta}{2}|\phi|^{-1}\sinh\big(c|\phi|^{\frac{1}{2}}\cos\tfrac{\beta}{2}\big)\cos\big(c|\phi|^{\frac{1}{2}}\sin\tfrac{\beta}{2}\big), \end{aligned}$$

$$I_{13} = \big(\gamma_1 - a_1/3\big)\cosh c\sqrt{\gamma_1 - a_1/3}, \quad I_{23} = \big(\gamma_1 - a_1/3\big)\sinh c\sqrt{\gamma_1 - a_1/3},$$

$$I_{33} = |\phi|\Big(\cos\beta\cosh\big(c|\phi|^{\frac{1}{2}}\cos\tfrac{\beta}{2}\big)\cos\big(c|\phi|^{\frac{1}{2}}\sin\tfrac{\beta}{2}\big) - \sin\beta\sinh\big(c|\phi|^{\frac{1}{2}}\cos\tfrac{\beta}{2}\big)\sin\big(c|\phi|^{\frac{1}{2}}\sin\tfrac{\beta}{2}\big)\Big),$$

$$I_{43} = |\phi|\Big(\cos\beta\sinh\big(c|\phi|^{\frac{1}{2}}\cos\tfrac{\beta}{2}\big)\cos\big(c|\phi|^{\frac{1}{2}}\sin\tfrac{\beta}{2}\big) - \sin\beta\cosh\big(c|\phi|^{\frac{1}{2}}\cos\tfrac{\beta}{2}\big)\sin\big(c|\phi|^{\frac{1}{2}}\sin\tfrac{\beta}{2}\big)\Big),$$

$$I_{53} = |\phi|\Big(\cos\beta\cosh\big(c|\phi|^{\frac{1}{2}}\cos\tfrac{\beta}{2}\big)\sin\big(c|\phi|^{\frac{1}{2}}\sin\tfrac{\beta}{2}\big) + \sin\beta\sinh\big(c|\phi|^{\frac{1}{2}}\cos\tfrac{\beta}{2}\big)\cos\big(c|\phi|^{\frac{1}{2}}\sin\tfrac{\beta}{2}\big)\Big),$$

$$I_{63} = |\phi|\Big(\cos\beta\sinh\big(c|\phi|^{\frac{1}{2}}\cos\tfrac{\beta}{2}\big)\sin\big(c|\phi|^{\frac{1}{2}}\sin\tfrac{\beta}{2}\big) + \sin\beta\cosh\big(c|\phi|^{\frac{1}{2}}\cos\tfrac{\beta}{2}\big)\cos\big(c|\phi|^{\frac{1}{2}}\sin\tfrac{\beta}{2}\big)\Big),$$

$$I_{14} = \big(\gamma_1 - a_1/3\big)^{\frac{3}{2}}\sinh c\sqrt{\gamma_1 - a_1/3}, \quad I_{24} = \big(\gamma_1 - a_1/3\big)^{\frac{3}{2}}\cosh c\sqrt{\gamma_1 - a_1/3},$$

$$I_{34} = |\phi|^{\frac{3}{2}}\Big(\cos\tfrac{3\beta}{2}\sinh\big(c|\phi|^{\frac{1}{2}}\cos\tfrac{\beta}{2}\big)\cos\big(c|\phi|^{\frac{1}{2}}\sin\tfrac{\beta}{2}\big) - \sin\tfrac{3\beta}{2}\cosh\big(c|\phi|^{\frac{1}{2}}\cos\tfrac{\beta}{2}\big)\sin\big(c|\phi|^{\frac{1}{2}}\sin\tfrac{\beta}{2}\big)\Big),$$

$$I_{44} = |\phi|^{\frac{3}{2}}\Big(\cos\tfrac{3\beta}{2}\cosh\big(c|\phi|^{\frac{1}{2}}\cos\tfrac{\beta}{2}\big)\cos\big(c|\phi|^{\frac{1}{2}}\sin\tfrac{\beta}{2}\big) - \sin\tfrac{3\beta}{2}\sinh\big(c|\phi|^{\frac{1}{2}}\cos\tfrac{\beta}{2}\big)\sin\big(c|\phi|^{\frac{1}{2}}\sin\tfrac{\beta}{2}\big)\Big),$$

$$I_{54} = |\phi|^{\frac{3}{2}}\Big(\cos\tfrac{3\beta}{2}\sinh\big(c|\phi|^{\frac{1}{2}}\cos\tfrac{\beta}{2}\big)\sin\big(c|\phi|^{\frac{1}{2}}\sin\tfrac{\beta}{2}\big) + \sin\tfrac{3\beta}{2}\cosh\big(c|\phi|^{\frac{1}{2}}\cos\tfrac{\beta}{2}\big)\cos\big(c|\phi|^{\frac{1}{2}}\sin\tfrac{\beta}{2}\big)\Big),$$

$$I_{64} = |\phi|^{\frac{3}{2}}\Big(\cos\tfrac{3\beta}{2}\cosh\big(c|\phi|^{\frac{1}{2}}\cos\tfrac{\beta}{2}\big)\sin\big(c|\phi|^{\frac{1}{2}}\sin\tfrac{\beta}{2}\big) + \sin\tfrac{3\beta}{2}\sinh\big(c|\phi|^{\frac{1}{2}}\cos\tfrac{\beta}{2}\big)\cos\big(c|\phi|^{\frac{1}{2}}\sin\tfrac{\beta}{2}\big)\Big).$$

List of symbols

Only important symbols are listed. Unlisted symbols are explained in the text.

$2c$	bonded overlap length on one adherend side
L	the length of the outer unbonded adherend
$2L_0$	the length of the inner unbonded doubler
t_1	adherend laminate thickness
t_2	doubler laminate thickness
M_0, M_1	unit-width bending moments at the outer and inner bonded overlap edges
k_{ij}	compliance terms (i, $j = 1$ and 2) defined in (A.1a)
T	joint remote unit-width tensile force
V_0, V_1	unit-width shear forces at the outer and inner bonded overlap edges
η	adhesive layer thickness
σ_a, τ_a	adhesive peel and shear stresses
E_a, G_a	adhesive Young's and shear moduli
a_1, a_2, b_1, b_2	joint parameters defined in (2b), (2c), (2d), and (2e)

References

[Bigwood and Crocombe 1989] D. A. Bigwood and A. D. Crocombe, "Elastic analysis and engineering design formulae for bonded joints", *Int. J. Adhes. Adhes.* **9**:4 (1989), 229–242.

[Chen and Cheng 1983] D. Chen and S. Cheng, "An analysis of adhesive-bonded single-lap joints", *J. Appl. Mech.* (*ASME*) **50**:1 (1983), 109–115.

[Cheng et al. 1991] S. Cheng, D. Chen, and Y. Shi, "Analysis of adhesive-bonded joints with nonidentical adherends", *J. Eng. Mech.* (*ASCE*) **117**:3 (1991), 605–623.

[Delale et al. 1981] F. Delale, F. Erdogan, and M. N. Aydinoglu, "Stresses in adhesively bonded joints: a closed-form solution", *J. Compos. Mater.* **15**:3 (1981), 249–271.

[Derrick and Grossman 1987] W. R. Derrick and S. I. Grossman, *A first course in differential equations with applications*, 3rd ed., West Publishing, St. Paul, MN, 1987.

[Goland and Reissner 1944] M. Goland and E. Reissner, "The stresses in cemented joints", *J. Appl. Mech.* (*ASME*) **11** (1944), A17–A27.

[Hart-Smith 1973] L. J. Hart-Smith, "Adhesive-bonded single lap joints", Contractor Report 112236, Douglas Aircraft Company, Long Beach, CA, 1973, available at http://tinyurl.com/NASA-CR-112236.

[Hart-Smith 1985] L. J. Hart-Smith, "Designing to minimize peel stresses in adhesive-bonded joints", pp. 238–266 in *Delamination and debonding of materials* (Pittsburgh, PA, 1983), edited by W. S. Johnson, ASTM Special Technical Publication **876**, American Society for Testing and Materials, Philadelphia, 1985.

[Hu 1995] G. Hu, "Mixed mode fracture analysis of adhesive lap joints", *Compos. Eng.* **5**:8 (1995), 1043–1050.

[Kelly 2006] G. Kelly, "Quasi-static strength and fatigue life of hybrid (bonded/bolted) composite single-lap joints", *Compos. Struct.* **72**:1 (2006), 119–129.

[Kreyszig 1993] E. Kreyszig, *Advanced engineering mathematics*, 7th ed., Wiley, New York, 1993.

[Li 2008] G. Li, "Exploration of closed-form solutions for adhesive stresses in bonded single-strap butt joints", Laboratory Technical Report LTR-SMPL-2008-0174, NRC Institute for Aerospace Research, National Research Council Canada, Ottawa, ON, 2008.

[Li 2010] G. Li, "Elastic analysis of closed-form solutions for adhesive stresses in bonded single-strap butt joints", *J. Mech. Mater. Struct.* **5**:3 (2010), 409–426.

[Li and Lee-Sullivan 2006a] G. Li and P. Lee-Sullivan, "Re-visiting the beam models for adhesively bonded single-lap joints, I: Comparison of bending moment predictions", *Can. Aeronaut. Space. J.* **52**:4 (2006), 149–171.

[Li and Lee-Sullivan 2006b] G. Li and P. Lee-Sullivan, "Re-visiting the beam models for adhesively bonded single-lap joints, II: Comparison of the adhesive stress predictions", *Can. Aeronaut. Space. J.* **52**:4 (2006), 173–180.

[Li et al. 1999] G. Li, P. Lee-Sullivan, and R. W. Thring, "Nonlinear finite element analysis of stress and strain distributions across the adhesive thickness in composite single-lap joints", *Compos. Struct.* **46**:4 (1999), 395–403.

[Li et al. 2011] G. Li, A. Johnston, M. Yanishevsky, and N. C. Bellinger, "Elastic deformation analysis of adhesively bonded composite butt joints in tension", *J. Aircraft* **48**:2 (2011), 578–590.

[Li et al. 2012] G. Li, J. H. Chen, M. Yanishevsky, and N. C. Bellinger, "Static strength of a composite butt joint configuration with different attachments", *Compos. Struct.* **94**:5 (2012), 1736–1744.

[Oplinger 1994] D. W. Oplinger, "Effects of adherend deflections in single lap joints", *Int. J. Solids Struct.* **31**:18 (1994), 2565–2587.

[Volkersen 1938] O. Volkersen, "Die Nietkraftverteilung in zugbeanspruchten Nietverbindungen mit konstanten Laschenquerschritten", *Luftfahrtforsch.* **15** (1938), 41–47.

Received 1 Sep 2011. Revised 24 Nov 2011. Accepted 13 Jan 2012.

GANG LI: Gang.Li@nrc-cnrc.gc.ca
Structures Group, Aerospace Portfolio, National Reseach Council Canada, M-3, 1200 Montreal Road, Ottawa ON K1A 0R6, Canada

JOURNAL OF MECHANICS OF MATERIALS AND STRUCTURES
Vol. 7, No. 4, 2012

MICROMECHANICAL STUDY OF DISPERSION AND DAMPING CHARACTERISTICS OF GRANULAR MATERIALS

NIELS P. KRUYT

The wave-propagation characteristics of dense granular materials have been studied from the micromechanical viewpoint, in which relationships are sought between properties at the micro-scale of particles and interparticle contacts and properties at the continuum, macro-scale. The dispersion and damping characteristics have been determined from a three-dimensional lattice analysis in which the particle interaction is modeled with linear elastic springs and linear viscous dashpots.

Due the presence of rotational degrees of freedom of the particles, optical branches are observed in the dispersion and damping characteristics, besides the acoustical branches. The influence of the micromechanical characteristics on the macroscopic dispersion and damping characteristics has been determined for a face-centered cubic lattice and a body-centered cubic lattice. For small wave numbers (large wave lengths) the damping of the optical branches is very large. This means that the optical branches will not be observed in conditions where a continuum-mechanical description is appropriate.

1. Introduction

In many disciplines of engineering, the propagation of waves is important. For example, wave propagation in granular materials is important in oil exploration. Granular materials are special materials in the sense that they possess a clear, discrete structure of particles with rotational degrees of freedom and interparticle contacts. In micromechanics of granular materials, relationships are investigated between properties at the micro-scale of particles and interparticle contacts and properties at the continuum, macro-scale.

Here the characteristics of wave propagation, dispersion and damping, are studied from the micromechanical viewpoint. In this approach the three-dimensional granular assembly is modeled as a large set of spherical particles that only interact at contacts through linear elastic springs and linear viscous dampers in directions normal and tangential to contacts.

The focus is on isotropic, dense or cemented granular materials where the particle displacements are small and the number of interparticle contacts does not change. Particle dampers (see for example [Els 2011]), where damping through particle collisions is important, are not considered.

The wave-propagation characteristics consist of the dispersion and damping characteristics. These characteristics give the complex circular frequencies $\omega = \omega(\boldsymbol{k})$ that are compatible with plane-wave solutions of the governing equations with a periodic spatial variation that is characterized by the wave vector $\boldsymbol{k}$, i.e., solutions for the unknowns $\boldsymbol{u}$ of the form

$$\begin{aligned}\boldsymbol{u}(\boldsymbol{x}, t) &= \boldsymbol{V} \exp[j(\omega t - \boldsymbol{k}\cdot\boldsymbol{x})] \\ &= \boldsymbol{V} \exp[-j\boldsymbol{k}\cdot\boldsymbol{x}] \exp[j\mathrm{Re}(\omega)t] \exp[-\mathrm{Im}(\omega)t],\end{aligned} \tag{1-1}$$

Keywords: wave propagation, granular materials, dispersion, damping.

where $\boldsymbol{x}$ is the position vector, t is time, j is the imaginary unit, $\boldsymbol{V}$ is an amplitude vector, $\mathrm{Re}(\omega)$ and $\mathrm{Im}(\omega)$ are the real part and the imaginary part of the complex circular frequency, respectively. The dispersion characteristics are given by $\mathrm{Re}(\omega)$ and the damping characteristics by $\mathrm{Im}(\omega)$. Note that $\mathrm{Im}(\omega) > 0$ for actual damping (reduction of the amplitude of $\boldsymbol{u}$ with time t).

The magnitude of the wave vector $\boldsymbol{k}$ is the wave number k. The wave number k is related to the wave length Λ by

$$\Lambda = \frac{2\pi}{k}. \tag{1-2}$$

Wave speeds for small wave numbers (large wave lengths) have been studied experimentally (see for example [Jia et al. 1999] and the references given in [Magnanimo et al. 2008]), theoretically (for example [Goddard 1990]), and numerically (for example [Makse et al. 2004; Agnolin and Roux 2007; Mouraille 2009]), showing a clear dependence on confining pressure. The pressure dependence is not studied here. This dependence can be incorporated by a proper choice for the dependence of the micromechanical parameters (interparticle stiffnesses and the coordination number, i.e., the average number of contacts per particle, as described in detail in Section 3) on confining pressure.

Suiker et al. [2001] and Suiker and de Borst [2005] derived dispersion relations for granular materials, based on a two-dimensional elastic lattice model of granular material (without damping). Schwartz et al. [1984] considered the dispersion relation of a three-dimensional face-centered cubic elastic lattice (FCC lattice for short), while Kruyt [2010] studied the dispersion relation for general three-dimensional elastic lattices (including the FCC lattice studied in [Schwartz et al. 1984]) and determined the influence of the micromechanical parameters on the dispersion characteristics. In all these lattice models the rotational degrees of freedom are explicitly accounted for. This leads to the presence of so-called optical branches in the dispersion relation, with nonzero circular frequency ω for small wave number k. Such optical branches also arise in solid state physics (see for example [Kittel 1953; Dekker 1962; Ashcroft and Mermin 1976; Myers 1997]) in the presence of atoms with varying properties, where the optical branches correspond to movement of the atoms relative to that of the center of mass of the unit cell.

Previous analyses are extended here by also taking viscous damping into account in the micromechanical model. Thus, dispersion *and* damping characteristics are obtained here, in terms of particle and interparticle characteristics, using three-dimensional lattice-based approaches. These results will be used to investigate what the (regularising) influence is of (small) viscous damping at the micro-scale on the macro-scale damping of the optical branches with their high circular frequencies for small wave number.

The outline of this study is as follows. Firstly, (classical) continuum-mechanical dispersion and damping characteristics are formulated for a viscoelastic material model in Section 2 in order to establish the continuum-mechanical framework. The relevant micromechanics of granular materials is described in Section 3. This is followed by the three-dimensional lattice formulation in Section 4. Results for the dispersion and damping characteristics are given in Section 5. Finally, findings from this study are summarized in Section 6.

2. Continuum-mechanical dispersion and damping characteristics

Dispersion characteristics for elastic materials are derived in many textbooks, based on classical continuum mechanics. For extended continua, such as Cosserat continua and micropolar continua that

incorporate couple stresses and (independent) rotational degrees of freedom, respectively, such dispersion characteristics for purely elastic materials have also been obtained [Eringen 1999].

For a viscoelastic material the continuum-mechanical dispersion and damping characteristics are analysed here, based on classical continuum mechanics. For small deformations $\boldsymbol{u}$ the governing conservation equation of momentum is

$$\rho \ddot{\boldsymbol{u}} = \nabla \cdot \boldsymbol{\sigma}, \tag{2-1}$$

where ρ is the density, the two superimposed dots denote the second derivative of $\boldsymbol{u}$ with respect to time t and $\boldsymbol{\sigma}$ is the stress increment (with respect to an equilibrium state). The stress increment is described by a (Kelvin–Voigt) viscoelastic model

$$\boldsymbol{\sigma} = \{\lambda \operatorname{tr}(\boldsymbol{\epsilon})\boldsymbol{I} + 2G\boldsymbol{\epsilon}\} + \{\kappa \operatorname{tr}(\dot{\boldsymbol{\epsilon}})\boldsymbol{I} + 2\eta\dot{\boldsymbol{\epsilon}}\}, \tag{2-2}$$

with the strain increment tensor $\boldsymbol{\epsilon}$ given by

$$\boldsymbol{\epsilon} = \tfrac{1}{2}[\nabla \boldsymbol{u} + (\nabla \boldsymbol{u})^T]. \tag{2-3}$$

The parameters λ and G are the elastic Lamé constants and the parameters κ and η are corresponding viscosities. The parameter λ is related to the bulk modulus K by

$$K = \lambda + \tfrac{2}{3}G. \tag{2-4}$$

With a plane-wave solution for the displacement vector $\boldsymbol{u}$ according to (1-1), it follows from (2-1), (2-2) and (2-3), after some algebra, that the circular frequency ω must satisfy the following quadratic eigenvalue problem

$$[\{(\lambda + j\kappa\omega) + (G + j\eta\omega)\}\boldsymbol{k}\boldsymbol{k} + (G + j\eta\omega)k^2\boldsymbol{I}] \cdot \boldsymbol{V} - \rho\omega^2\boldsymbol{V} = \boldsymbol{0}, \tag{2-5}$$

where $\boldsymbol{I}$ is the 3-by-3 identity matrix.

After some further algebra we find the solutions:

- a *longitudinal branch* where the eigenvector $\boldsymbol{V}$ is in the direction of the wave vector $\boldsymbol{k}$:

$$\operatorname{Re}(\omega) \cong \sqrt{\frac{\lambda+2G}{\rho}}k, \quad \operatorname{Im}(\omega) \cong \frac{\kappa+2\eta}{2\rho}k^2; \tag{2-6}$$

- a *transverse branch* where the eigenvector $\boldsymbol{V}$ is perpendicular to the wave vector $\boldsymbol{k}$:

$$\operatorname{Re}(\omega) \cong \sqrt{\frac{G}{\rho}}k, \quad \operatorname{Im}(\omega) \cong \frac{\eta}{2\rho}k^2. \tag{2-7}$$

The multiplicity of the eigenvalue of the longitudinal branch equals one, while that of the transverse branch equals two. The longitudinal and transverse branches are called *acoustical*, as the dispersion characteristics $\operatorname{Re}(\omega)$ are proportional to the wave number k and hence cross the origin (contrary to the *optical* branches). Their damping characteristics $\operatorname{Im}(\omega)$ are proportional to k^2.

This continuum-mechanical approach is valid in the large wave-length case, that is, for small wave number k.

3. Micromechanics

Three-dimensional assemblies consisting of spherical particles are considered here. The radius of particle p is denoted by R^p and the position of the center of mass of particle p is given by $\boldsymbol{X}^p$. For two particles p and q in contact, $\boldsymbol{r}^{pq}$ is the vector directed from the center of particle p to the contact point between particles p and q, with an analogous definition for $\boldsymbol{r}^{qp}$. For very stiff particles where the "overlap" (elastic deformation) at contacts is small, the unit normal vector $\boldsymbol{n}^{pq}$ at the contact is obtained from

$$\boldsymbol{r}^{pq} = R^p \boldsymbol{n}^{pq}. \tag{3-1}$$

The direction of the normal vector $\boldsymbol{n}^{pq}$ determines the orientation of the contact.

The (small) displacement vector of the center of particle p, relative to the selected reference equilibrium configuration, is denoted by $\boldsymbol{u}^p$, while the (small) particle rotation vector is indicated by $\boldsymbol{\theta}^p$. The equations of motion governing the evolution with time t of the displacement $\boldsymbol{u}^p$ and rotation $\boldsymbol{\theta}^p$ of the spherical particle p are

$$m^p \ddot{\boldsymbol{u}}^p = \sum_q \boldsymbol{f}^{pq}, \quad I^p \ddot{\boldsymbol{\theta}}^p = \sum_q \boldsymbol{r}^{pq} \times \boldsymbol{f}^{pq}, \tag{3-2}$$

where the two superimposed dots denote the second derivative of the quantity involved with respect to time t, m^p and I^p are the mass and moment of inertia of the particle p, respectively, $\boldsymbol{f}^{pq}$ is the force exerted on particle p by particle q and the sum is over particles q that are in contact with particle p. The moment of inertia I^p for a sphere with radius R^p and mass m^p is given by

$$I^p = Q m^p {R^p}^2, \tag{3-3}$$

where $Q = \frac{2}{5}$ for a solid sphere and $Q = \frac{2}{3}$ for a hollow sphere. In the following, solid spheres with $Q = \frac{2}{5}$ are considered when numerical results are presented. Note that body forces, like gravitational forces, have been excluded in (3-2).

The relative displacement vector $\boldsymbol{\Delta}^{pq}$ at the contact point between two particles in contact p and q is given by

$$\boldsymbol{\Delta}^{pq} = [\boldsymbol{u}^p + \boldsymbol{\theta}^p \times \boldsymbol{r}^{pq}] - [\boldsymbol{u}^q + \boldsymbol{\theta}^q \times \boldsymbol{r}^{qp}]. \tag{3-4}$$

Note that the relative displacement vector involves contributions due to particle translations $\boldsymbol{u}^p$ and due to particle rotations $\boldsymbol{\theta}^p$.

The (increment of the) contact force $\boldsymbol{f}^c$ at contact c is related to the relative displacement $\boldsymbol{\Delta}^c$ and the relative velocity $\dot{\boldsymbol{\Delta}}^c$ (i.e., the time derivative of the relative displacement) at the contact through the contact constitutive relation. Since small displacements are considered, the contact constitutive relation can be formulated in a linearized form that considers two mechanisms: elastic deformation and viscous damping.

Coulomb frictional damping is not considered here, since the focus is on isotropic states where the number of contacts where Coulomb friction is fully mobilized is small. Because of the assumption of small displacements, contacts that are in an elastic state will remain to do so.

Hertz–Mindlin theory (see for example [Johnson 1985]) gives a nonlinear dependence of the elastic interparticle forces on the relative displacements. In the adopted small-displacement approach, the linearized form of this relation is described by two (linear) elastic springs in normal and tangential directions

at the contact, with spring stiffnesses k_n and k_t, respectively. The spring stiffnesses k_n and k_t then depend on the normal force in the equilibrium state, and hence on the (average) confining pressure.

As with the elastic interaction, the relation between the viscous force and the relative velocity is described by two linear viscous dashpots in normal and tangential directions at the contact, with viscous damping coefficients d_n and d_t, respectively.

The employed contact constitutive relation then can be written as

$$\boldsymbol{f}^c = -\boldsymbol{S}^c \cdot \boldsymbol{\Delta}^c - \boldsymbol{D}^c \cdot \dot{\boldsymbol{\Delta}}^c, \tag{3-5}$$

where the (elastic) contact stiffness matrix $\boldsymbol{S}^c$ and the (viscous) contact damping matrix $\boldsymbol{D}^c$ are given by

$$\boldsymbol{S}^c = (k_n - k_t)\boldsymbol{n}^c\boldsymbol{n}^c + k_t\boldsymbol{I}, \quad \boldsymbol{D}^c = (d_n - d_t)\boldsymbol{n}^c\boldsymbol{n}^c + d_t\boldsymbol{I}. \tag{3-6}$$

Here $\boldsymbol{I}$ is the 3-by-3 identity matrix. Note that these expressions satisfy Newton's third law, $\boldsymbol{f}^{qp} = -\boldsymbol{f}^{pq}$, since $\boldsymbol{\Delta}^{qp} = -\boldsymbol{\Delta}^{pq}$ and the contact stiffness and damping matrices are symmetrical.

The normal and tangential viscous damping coefficients, d_n and d_t, can also be expressed in terms of normal and tangential coefficients of restitution [Wu et al. 2003; Kruggel-Emden et al. 2007; Schwager and Pöschel 2007; Schwager et al. 2008; O'Sullivan 2011].

The equations of motion, Equations (3-2), can be expressed concisely in terms of a generalized displacement vector $\boldsymbol{U}^p$, a generalized force vector $\boldsymbol{F}^{pq}$ and a generalized mass matrix $\boldsymbol{M}^p$ by

$$\boldsymbol{M}^p \cdot \ddot{\boldsymbol{U}}^p = \sum_q \boldsymbol{F}^{pq}, \quad \boldsymbol{U}^p = \begin{bmatrix} \boldsymbol{u}^p \\ R^p\boldsymbol{\theta}^p \end{bmatrix}, \quad \boldsymbol{M}^p = m^p \begin{bmatrix} \boldsymbol{I} & \boldsymbol{0} \\ \boldsymbol{0} & Q\boldsymbol{I} \end{bmatrix}, \quad \boldsymbol{F}^{pq} = \begin{bmatrix} \boldsymbol{f}^{pq} \\ \boldsymbol{n}^{pq} \times \boldsymbol{f}^{pq} \end{bmatrix}. \tag{3-7}$$

Note that the terms in $\boldsymbol{U}^p$ and $\boldsymbol{F}^{pq}$ have the same dimension (or unit), through the inclusion and exclusion, respectively, of the particle radius R^p. For compactness in notation, the generalized force $\boldsymbol{F}^{pq}$ is expressed as

$$\boldsymbol{F}^{pq} = \begin{bmatrix} \boldsymbol{I} \\ \boldsymbol{N}^{\times pq} \end{bmatrix} \cdot \boldsymbol{f}^{pq}, \tag{3-8}$$

where the operator $\boldsymbol{N}^{\times pq}$ is defined by the equality $\boldsymbol{N}^{\times pq} \cdot \boldsymbol{v} = \boldsymbol{n}^{pq} \times \boldsymbol{v}$ for all $\boldsymbol{v}$. Thus

$$\boldsymbol{N}^{\times pq} = -\boldsymbol{P} \cdot \boldsymbol{n}^{pq}, \tag{3-9}$$

with $\boldsymbol{P}$ the three-dimensional permutation symbol.

4. Lattice formulation

The regular lattice geometry is described as follows (see Figure 1). A central particle '0' at position $\boldsymbol{X}_0$ is in contact with Z other particles. All particles have the same properties, such as identical particle radius R, mass m and coordination number Z, i.e., the number of contacts per particle. The unit normal vector at the contact c is denoted by $\boldsymbol{n}^c$. The set of normal vectors $\{\boldsymbol{n}^c\}$ determines the lattice directions. The position of the center $\boldsymbol{X}^c$ of the other particles in contact with the central particle '0' is given by $\boldsymbol{X}^c = \boldsymbol{X}_0 + 2R\boldsymbol{n}^c$. Two different three-dimensional lattices will be considered in detail in the following. These are the face-centered cubic (FCC) and body-centered cubic (BCC) lattices, as shown in Figure 2. The fabric tensor [Horne 1965], based on the contact normals, is isotropic for these lattices.

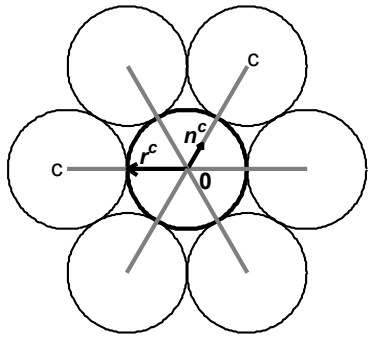

Figure 1. Example of a two-dimensional lattice with coordination number $Z = 6$. Also indicated are the contact normal vector $\boldsymbol{n}^c$ and the vector $\boldsymbol{r}^c$ from the center of the particle to the point of contact.

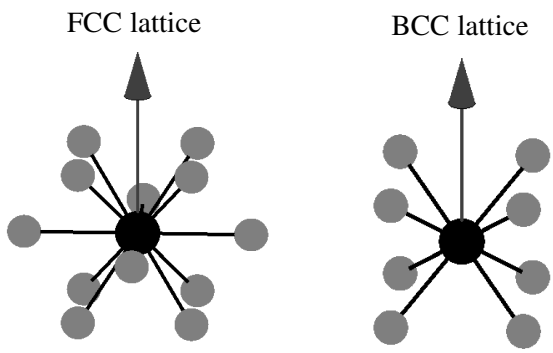

Figure 2. Lattice geometry. Left: FCC lattice, with coordination number $Z = 12$. Right: BCC lattice, with coordination number $Z = 8$. The central sphere of each lattice is shown in black, while the other spheres that are in contact with the central one are shown in gray. The radius of the spheres has been reduced for visual clarity: therefore the spheres in contact appear as if they were not in contact. Contacts between spheres are indicated by black lines connecting particle centers. The direction of the wave vector is indicated by the upward arrow.

For the *spatial* variation of the generalized displacement vector $\boldsymbol{U}(\boldsymbol{x}, t)$, a periodic variation is assumed

$$\boldsymbol{U}(\boldsymbol{x}, t) = \boldsymbol{U}_0(t) \exp[-j\boldsymbol{k} \cdot (\boldsymbol{x} - \boldsymbol{X}_0)] = \begin{bmatrix} \boldsymbol{u}_0(t) \\ R\boldsymbol{\theta}_0(t) \end{bmatrix} \exp[-j\boldsymbol{k} \cdot (\boldsymbol{x} - \boldsymbol{X}_0)], \tag{4-1}$$

where $\boldsymbol{u}_0(t)$ and $\boldsymbol{\theta}_0(t)$ are the time-dependent amplitude vectors for the displacements and rotations, respectively.

Employing the assumed solution according to (4-1), the relative displacement vector $\boldsymbol{\Delta}^c$ at contact c becomes, from (3-4) with $\boldsymbol{r}^{0c} = R\boldsymbol{n}^c$ and $\boldsymbol{r}^{c0} = -R\boldsymbol{n}^c$ for spherical particles with equal radius R,

$$\boldsymbol{\Delta}^c = (1 - \xi^c)\boldsymbol{u}_0 + (1 + \xi^c)R\boldsymbol{\theta}_0 \times \boldsymbol{n}^c, \quad \xi^c = \exp[-j(2R)\boldsymbol{k} \cdot \boldsymbol{n}^c]. \tag{4-2}$$

Note that the scalar factor ξ^c (also) depends on the wave vector $\boldsymbol{k}$. The relative displacement vector can be expressed in terms of the amplitude vector $\boldsymbol{U}_0$ and the operator $\boldsymbol{N}^{\times c}$ defined in (3-9) by

$$\boldsymbol{\Delta}^c = \left[(1-\xi^c)\boldsymbol{I} \quad -(1+\xi^c)\boldsymbol{N}^{\times c}\right] \cdot \boldsymbol{U}_0, \tag{4-3}$$

where the term inside the square brackets is a 3 by 6 matrix, which does not involve a subtraction.

It then follows that the amplitude vector $\boldsymbol{U}_0$ satisfies the second-order ordinary differential equation

$$\boldsymbol{M} \cdot \ddot{\boldsymbol{U}}_0 + \bar{\boldsymbol{D}} \cdot \dot{\boldsymbol{U}}_0 + \bar{\boldsymbol{K}} \cdot \boldsymbol{U}_0 = \boldsymbol{0}, \tag{4-4}$$

where the effective damping matrix $\bar{\boldsymbol{D}}$ and the effective stiffness matrix $\bar{\boldsymbol{K}}$ are given by

$$\begin{aligned} \bar{\boldsymbol{D}} &= \sum_{c=1}^{C} \begin{bmatrix} \boldsymbol{I} \\ \boldsymbol{N}^{\times c} \end{bmatrix} \cdot \boldsymbol{D}^c \cdot \left[(1-\xi^c)\boldsymbol{I} \quad -(1+\xi^c)\boldsymbol{N}^{\times c}\right], \\ \bar{\boldsymbol{K}} &= \sum_{c=1}^{C} \begin{bmatrix} \boldsymbol{I} \\ \boldsymbol{N}^{\times c} \end{bmatrix} \cdot \boldsymbol{S}^c \cdot \left[(1-\xi^c)\boldsymbol{I} \quad -(1+\xi^c)\boldsymbol{N}^{\times c}\right]. \end{aligned} \tag{4-5}$$

The size of the matrices $\bar{\boldsymbol{D}}$ and $\bar{\boldsymbol{K}}$ is 6 by 6. It can be shown, after some algebra, that the matrices $\bar{\boldsymbol{D}}$ and $\bar{\boldsymbol{K}}$ are Hermitian, using the fact that for every lattice direction $\boldsymbol{n}^c$ there is a corresponding direction $-\boldsymbol{n}^c$, $\boldsymbol{S}(-\boldsymbol{n}^c) = \boldsymbol{S}(\boldsymbol{n}^c)$, $\boldsymbol{D}(-\boldsymbol{n}^c) = \boldsymbol{D}(\boldsymbol{n}^c)$, $\boldsymbol{N}^{\times}(-\boldsymbol{n}^c) = -\boldsymbol{N}^{\times}(\boldsymbol{n}^c)$ and $\xi(-\boldsymbol{n}^c) = \xi^*(\boldsymbol{n}^c)$. Here ξ^* denotes the complex conjugate of ξ.

For an harmonic variation in time for the amplitude vector $\boldsymbol{U}_0(t)$

$$\boldsymbol{U}_0(t) = \boldsymbol{U}_a \exp j\omega t, \tag{4-6}$$

we obtain the following *quadratic eigenvalue problem* for the (complex) eigenfrequencies $\omega = \omega(\boldsymbol{k})$

$$[-\omega^2 \boldsymbol{M} + j\omega \bar{\boldsymbol{D}} + \bar{\boldsymbol{K}}] \cdot \boldsymbol{U}_a = \boldsymbol{0}. \tag{4-7}$$

The eigenfrequencies of this quadratic eigenvalue problem can be computed numerically from (4-7) or they can be obtained from the solution of a (larger) generalized eigenvalue problem that is obtained from the so-called linearisation approach (see for example, [Tisseur and Meerbergen 2001]). When considering analytical solutions, it is more convenient to consider the generalized eigenvalue problem. The linearisation approach is outlined in the next Section.

4A. ***Linearisation approach.*** The system (4-4) of second-order equations of motion can be rewritten as a larger system of first-order ordinary differential equations by introducing the variable (see for example [Tisseur and Meerbergen 2001])

$$\boldsymbol{P}_0 = \begin{bmatrix} \dot{\boldsymbol{U}}_0 \\ \boldsymbol{U}_0 \end{bmatrix}. \tag{4-8}$$

The resulting system of first-order ordinary differential equations is

$$\begin{bmatrix} \boldsymbol{M} & \boldsymbol{0} \\ \boldsymbol{0} & \hat{\boldsymbol{I}} \end{bmatrix} \cdot \dot{\boldsymbol{P}}_0 + \begin{bmatrix} \bar{\boldsymbol{D}} & \bar{\boldsymbol{K}} \\ -\hat{\boldsymbol{I}} & \boldsymbol{0} \end{bmatrix} \cdot \boldsymbol{P}_0 = \boldsymbol{0}, \tag{4-9}$$

where $\hat{\boldsymbol{I}}$ is the 6 by 6 identity matrix. With an harmonic time-dependence of $\boldsymbol{P}_0(t) = \boldsymbol{P}_a \exp[j\omega t]$, a generalized eigenvalue problem is obtained for the circular frequency ω

$$\begin{bmatrix} \bar{\boldsymbol{D}} & \bar{\boldsymbol{K}} \\ -\hat{\boldsymbol{I}} & \boldsymbol{0} \end{bmatrix} \cdot \boldsymbol{P}_a = \omega(-j) \begin{bmatrix} \boldsymbol{M} & \boldsymbol{0} \\ \boldsymbol{0} & \hat{\boldsymbol{I}} \end{bmatrix} \cdot \boldsymbol{P}_a. \tag{4-10}$$

4B. ***Branches in the dispersion and damping characteristics.*** From the numerical results for the eigenvectors corresponding to the eigenfrequencies, the dominant mode of motion has been identified for each eigenfrequency. This leads to the distinction of the following branches in the dispersion and damping characteristics (see also Section 2):

LA (longitudinal acoustical): the dominant motion is *longitudinal displacement*, i.e., in the direction of the wave vector $\boldsymbol{k}$; the multiplicity of the eigenfrequency is one;

TA (transverse acoustical): the dominant motion is *transverse displacement*, relative to the direction of the wave vector $\boldsymbol{k}$; the multiplicity of the eigenfrequency is two;

LO (longitudinal optical): the dominant motion is *longitudinal rotation*, i.e., in the direction of the wave vector $\boldsymbol{k}$; the multiplicity of the eigenfrequency is one;

TO (transverse optical): the dominant motion is *transverse rotation*, relative to in the direction of the wave vector $\boldsymbol{k}$; the multiplicity of the eigenfrequency is two.

The acoustical branches also resulted from the classical continuum-mechanical analysis of Section 2. Extended continuum-mechanical theories (see for example, [Mindlin 1972; Kunin 1982; 1983; Eringen 1999; Suiker et al. 2001; Suiker and de Borst 2005]) also give optical branches in the dispersion characteristics. In the lattice-based micromechanical analysis the optical branches arise due to the presence of rotational degrees of freedom [Schwartz et al. 1984; Suiker et al. 2001; Suiker and de Borst 2005; Kruyt 2010].

For future reference, non-dimensional micromechanical parameters are introduced that relate

(1) the tangential elastic stiffness to the normal elastic stiffness,

(2) the tangential viscous damping coefficient to the normal viscous damping coefficient and

(3) the normal viscous damping coefficient to the normal elastic stiffness and the particle mass.

The stiffness ratio r_K, the damping ratio r_D and the damping factor ζ (often called the damping ratio) are defined by

$$r_K = \frac{k_t}{k_n}, \quad r_D = \frac{d_t}{d_n}, \quad \zeta = \frac{d_n}{2\sqrt{k_n m}}. \tag{4-11}$$

The nondimensional wave number $\hat{k}$ and nondimensional frequency $\hat{\omega}$ are defined by

$$\hat{k} = \left(\frac{2R}{\pi}\right)k, \quad \hat{\omega} = \sqrt{\frac{m}{k_n}}\omega. \tag{4-12}$$

4C. ***Analytical solution for FCC lattice for small wave number.*** For small wave number k, analytical solutions for the eigenfrequencies ω have been found by factoring the characteristic polynomial corresponding to (4-10). From a Taylor expansion in wave number k, the solutions for an FCC lattice are obtained after some lengthy algebra (using a symbolic mathematics package). The results for the

non-dimensional real and the imaginary parts of the non-dimensional eigenfrequencies $\hat{\omega}$ are given in Table 1.

Longitudinal	$\mathrm{Re}(\hat{\omega}) \cong 2\sqrt{1+r_K}(Rk)$	$\mathrm{Im}(\hat{\omega}) \cong 4(1+4r_D)\zeta(Rk)^2$
Transverse	$\mathrm{Re}(\hat{\omega}) \cong \sqrt{2}\sqrt{1+r_K}(Rk)$	$\mathrm{Im}(\hat{\omega}) \cong 2(1+r_D)\zeta(Rk)^2$
Optical	$\mathrm{Re}(\hat{\omega}) \cong \frac{4}{Q}\sqrt{Qr_K - 16r_D^2\zeta^2}$	$\mathrm{Im}(\hat{\omega}) \cong \frac{16r_D\zeta}{Q}$

Table 1. Real and imaginary parts of the nondimensional eigenfrequencies $\hat{\omega}$ in the three situations considered.

The multiplicity of the eigenfrequency for the longitudinal branch equals one, that for the transverse equals two and for the optical branch three (both longitudinal and transverse optical).

The dispersion characteristics show branches where $\mathrm{Re}(\omega)$ is proportional to k and the damping characteristics show branches where $\mathrm{Im}(\omega)$ is proportional to k^2. These results are consistent with the results of the classical continuum-mechanical analysis of Section 2 that is based on a viscoelastic continuum material model.

The reduction in time t of the *amplitude* of the generalized displacement vector $\boldsymbol{U}$ is given by

$$\frac{\|\boldsymbol{U}(\boldsymbol{x},t)\|}{\|\boldsymbol{U}(\boldsymbol{x},0)\|} = e^{-\mathrm{Im}(\omega)t}. \tag{4-13}$$

With a characteristic time τ based on a single cycle, $\tau = (2\pi)/\mathrm{Re}(\omega)$, for the *lowest* frequency according to Table 1, the reduction of the amplitude of the optical branches becomes

$$\frac{\|\boldsymbol{U}(\boldsymbol{x},\tau)\|}{\|\boldsymbol{U}(\boldsymbol{x},0)\|} = \exp\left(-\frac{16\sqrt{2}\pi(r_D\zeta)}{Q\sqrt{1+r_K}}\,\frac{1}{Rk}\right), \tag{4-14}$$

and the reduction of the amplitude of the transverse acoustical branch becomes

$$\frac{\|\boldsymbol{U}(\boldsymbol{x},\tau)\|}{\|\boldsymbol{U}(\boldsymbol{x},0)\|} = \exp\left(-\frac{4\sqrt{2}\pi(1+4r_D)\zeta}{\sqrt{1+r_K}}\,Rk\right). \tag{4-15}$$

For small wave number k, the reduction in amplitude of the optical branches is very large (the argument of the exponent is *inversely* proportional to the wave number k), contrary to that of the acoustical branches (the argument of the exponent is proportional to the wave number k). This means that the optical branches are dampened out very rapidly, and will not be observed in situations where a continuum-mechanical description is appropriate.

5. Results

The dispersion and damping characteristics, $\mathrm{Re}(\omega)$ and $\mathrm{Im}(\omega)$, respectively, that have been obtained from the solution to the quadratic eigenvalue problem (4-7), are shown for the FCC lattice and the BCC lattice. This is done for various values of the damping factor ζ, the stiffness ratio r_K and the damping ratio r_D to show the influence of these micromechanical material characteristics on the macro-scale, continuum characteristics.

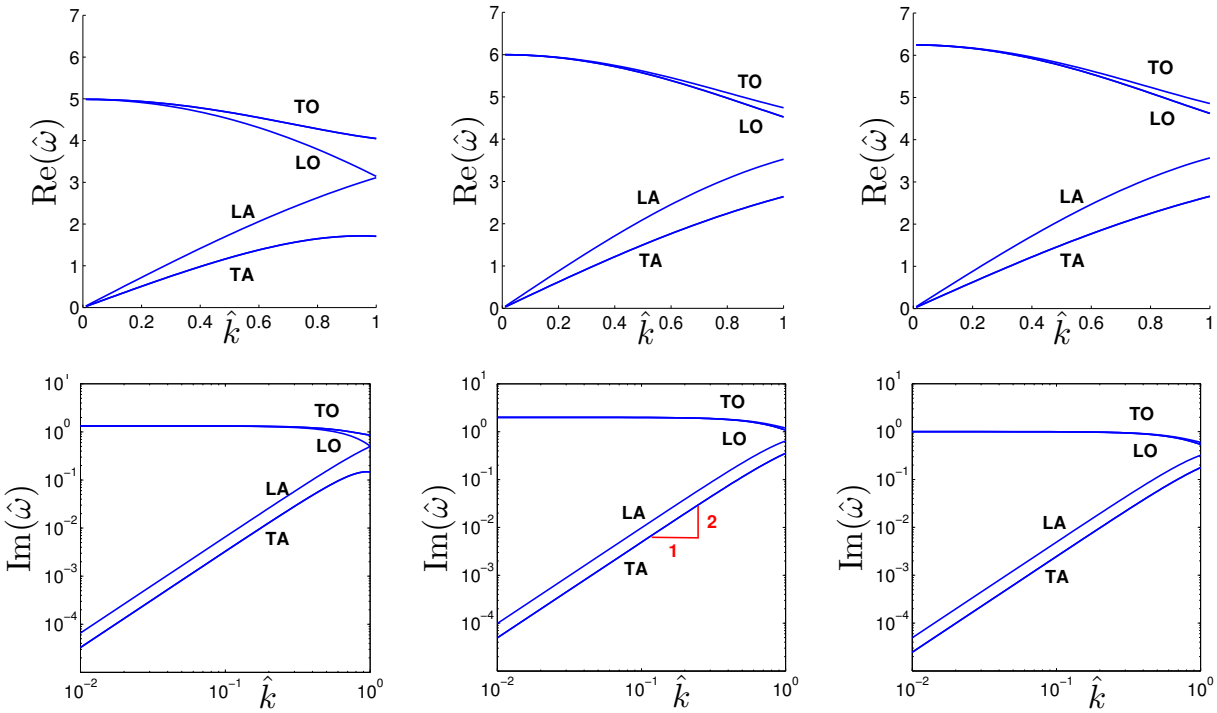

Figure 3. Dispersion characteristics (top row) and damping characteristics (bottom row). Left: BCC lattice with $\zeta = 0.05$. Middle: FCC lattice with $\zeta = 0.05$. Right: FCC lattice with $\zeta = 0.025$. In all cases $r_K = 1$; $r_D = 1$.

The middle column of Figure 3 shows typical results for the dispersion relation, Re(ω) as a function of wave number k (top graph) and for the damping characteristics Im(ω) as a function of wave number k (bottom graph).

In each of those plots four curves are shown, two acoustical branches that go through the origin and two other, optical branches. Two curves correspond to eigenfrequencies with multiplicity of one, the longitudinal branches, and two curves correspond to eigenfrequencies with multiplicity of two, the transverse branches. The total number of eigenfrequencies is six.

The two acoustical dispersion curves show an approximately linear dependence of the eigenfrequency Re(ω) on wave number k, consistent with the continuum-mechanical analysis of Section 2. The slope of the longitudinal branch is higher than that of the transverse branch. These slopes are related to the bulk modulus K and shear modulus G; see (2-6) and (2-7).

The two optical dispersion curves show a relatively weak dependence of eigenfrequency on wave number. The difference between the frequencies for the longitudinal and the transverse branches is not very large, especially for small wave numbers.

The damping characteristics of the acoustical branches show a dependence of Im(ω) on k^2, consistent with the continuum-mechanical analysis of Section 2 and with the analytical solution for the FCC lattice in Table 1. Note that the damping characteristics are presented in a log-log plot in order to show this

dependence. The damping of the optical branches is very high and is only (relatively) weakly dependent on wave number.

The results for the dispersion and the damping characteristics for the FCC lattice for small wave numbers are in agreement with the analytical expressions in Table 1.

As shown in [Suiker and de Borst 2005] for two-dimensional lattices, the direction of the wave vector $\boldsymbol{k}$ influences the dispersion relation at higher wave numbers k (small wave length), since the inherent anisotropic structure of the lattices is then apparent. For small wave number k, however, it was noted in [Suiker and de Borst 2005] that the dispersion relation is independent of the direction of the wave vector $\boldsymbol{k}$. The same is found for the three-dimensional lattices considered here (results not shown).

5A. ***Influence of lattice.*** The influence of the type of lattice on the dispersion and damping characteristics has been investigated by comparing the results for the BCC lattice (left column in Figure 3) with coordination number $Z = 8$ and for the FCC lattice (middle column) with $Z = 12$. The other micromechanical parameters are the same: $\zeta = 0.05$, $r_K = 1$ and $r_D = 1$.

Qualitatively, the dispersion and the damping characteristics for the FCC lattice and the BCC lattice are very similar. The slopes of the acoustical dispersion curves for the FCC lattice (top row, middle column in Figure 3) are larger than those for the BCC lattice (top left). This is expected, since these slopes are related to the continuum bulk and shear moduli; see Section 2. These moduli are dependent on the coordination number Z (see for example [Bathurst and Rothenburg 1988; Kruyt et al. 2010]), which is higher for the FCC lattice than for the BCC lattice. The frequency for small wave numbers of the optical branches is higher for the FCC lattice than for the BCC lattice.

The damping is higher for the FCC lattice with its higher coordination number than for the BCC lattice. A high coordination number means that a large number of contact areas (represented by the elastic springs and the viscous dashpots) is present where energy dissipation occurs.

5B. ***Influence of damping factor.*** The influence of the damping factor ζ on the dispersion and damping characteristics has been investigated by comparing the results for the FCC lattice for $\zeta = 0.05$ (middle column in Figure 3) with those for $\zeta = 0.025$ (right column). The other micromechanical parameters are the same: $r_K = 1$ and $r_D = 1$.

For small wave numbers the dispersion characteristics, $\mathrm{Re}(\omega)$, of the acoustical branches are not affected by the value of the damping factor ζ. This also follows from the analytical solution in Table 1. The frequency of the optical dispersion branches increases with decreasing damping factor ζ; see also Table 1.

As expected, a lower value of the damping factor ζ results in lower damping characteristics, $\mathrm{Im}(\omega)$, of all branches; see also Table 1.

5C. ***Influence of stiffness ratio.*** The influence of the stiffness ratio r_K on the dispersion and damping characteristics has been investigated by comparing the results with $r_K = 1$ (middle column of Figure 4) with those with $r_K = 0.5$ (left column). In this comparison the BCC lattice is considered with the other micromechanical parameters $\zeta = 0.05$ and $r_D = 1$.

For the dispersion characteristics, the slope of the acoustical branches for small wave number increases with increasing stiffness ratio r_K, since a higher value for r_K corresponds to a higher value for the shear modulus; the bulk modulus is only weakly affected by the value of the stiffness ratio when the

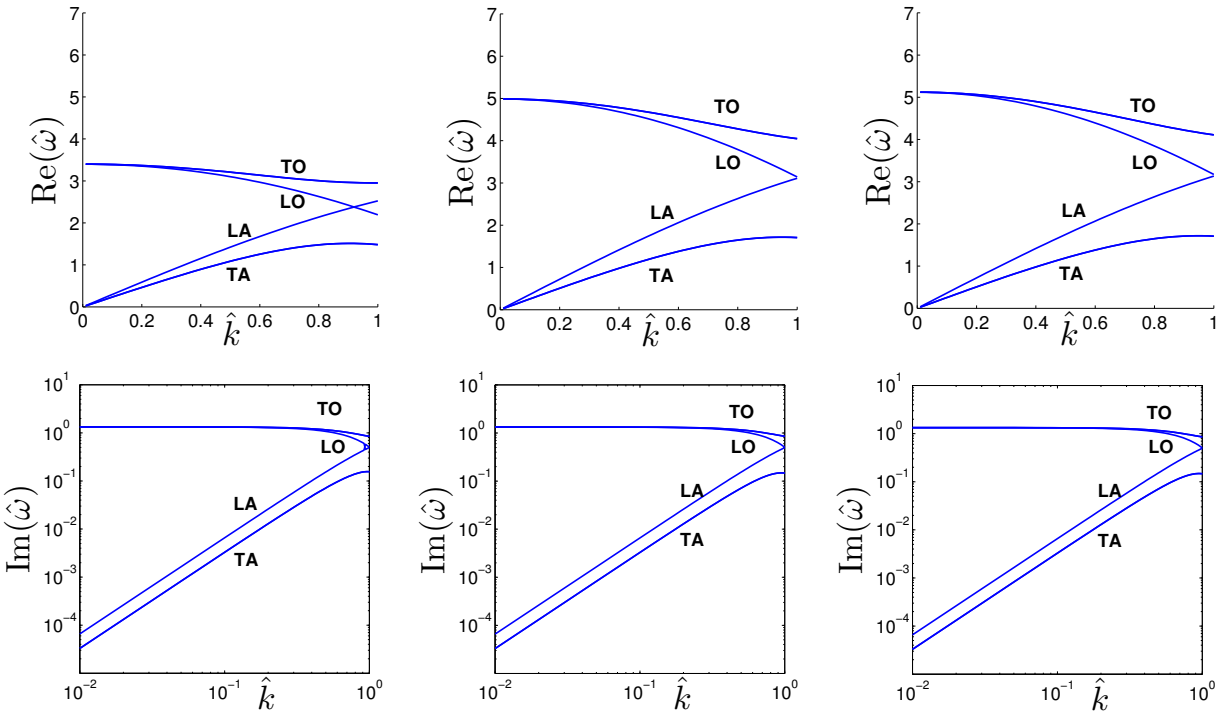

Figure 4. Dispersion characteristics (top row) and damping characteristics (bottom row). Left: $r_K = 0.5$, $r_D = 1$. Middle: $r_K = 1$, $r_D = 1$. Right: $r_K = 1$, $r_D = 0.5$. In all cases the BCC lattice is considered, with $\zeta = 0.05$.

coordination number is not low. See [Bathurst and Rothenburg 1988; Kruyt et al. 2010]. The optical branches show a higher frequency for a higher stiffness ratio. These trends for the BCC lattice are the same as for the FCC lattice; see the analytical solution in Table 1.

The damping characteristics are hardly affected by the value of the stiffness ratio. This trend is also shown by the analytical solution for the FCC lattice; see Table 1.

5D. ***Influence of damping ratio.*** The influence of the damping ratio r_D on the dispersion and damping characteristics has been investigated by comparing the results with $r_D = 1$ (middle column of Figure 4) with those with $r_D = 0.5$ (right column). In this comparison the BCC lattice is considered with the micromechanical parameters $\zeta = 0.05$ and $r_K = 1$.

The dispersion characteristics are hardly affected by the value of the damping ratio r_D. Only a small increase in the frequency of the optical branch is observed for the lower value of the damping ratio.

The damping characteristics are directly affected by the value of the damping ratio. A higher value of the damping ratio r_D gives higher damping characteristics.

These observations on the dispersion and the damping characteristics for the BCC lattice correspond to the analytical results for the FCC lattice; see Table 1.

6. Conclusions

Dispersion and damping characteristics of granular materials have been studied using a three-dimensional lattice-based approach in which the particle interaction is modeled with linear elastic springs and linear viscous dashpots. The lattice analysis leads to a quadratic eigenvalue problem for the complex eigenfrequencies.

The analysis yields acoustical and optical branches, as noted in previous studies [Schwartz et al. 1984; Suiker et al. 2001; Suiker and de Borst 2005; Kruyt 2010]. The present analysis allows for a study of the influence of the micromechanical characteristics on the continuum-mechanical dispersion and damping characteristics:

- The effect of the *type of lattice* is primarily through the coordination number. A high coordination number gives high bulk and shear moduli, and thus large slopes of the dispersion characteristics of the acoustical branches. Similarly, a high coordination number results in high damping.
- The *damping factor* has only a small effect on the dispersion characteristics of the acoustical branches. The damping increases with increasing damping factor.
- A high value of the *stiffness ratio* results in high bulk and shear moduli, and thus large slopes of the dispersion characteristics of the acoustical branches. The influence on the damping characteristics is small.
- A high value of the *damping ratio* does not affect the dispersion characteristics of the acoustical branches. A high damping ratio leads to high damping.

An important result is that the damping of the optical branches is very high. Therefore it is expected that these branches will not be observed under conditions where a continuum-mechanical description is appropriate.

The present lattice-based analysis is effectively based on the uniform-strain assumption (or mean-field assumption) for the relative displacement at contacts; see (1-1). It is well-known (see for instance [Makse et al. 1999; Kruyt and Rothenburg 2001; Kruyt and Rothenburg 2002; Kruyt et al. 2010]) that this assumption leads to an inaccurate prediction of the elastic moduli in the static case for *random* packings, especially for lower coordination numbers. It is expected that the dispersion and damping characteristics of a random packing agree qualitatively with the present results for lattices, but may show quantitative discrepancies. The quantitative study of these characteristics of random packings is a subject of further investigation.

References

[Agnolin and Roux 2007] I. Agnolin and J.-N. Roux, "Internal states of model isotropic granular packings, III: Elastic properties", *Phys. Rev. E* (3) **76**:6 (2007), 061304, 22.

[Ashcroft and Mermin 1976] N. W. Ashcroft and N. D. Mermin, *Solid state physics*, Saunders College Publishing, Fort Worth, TX, 1976.

[Bathurst and Rothenburg 1988] R. J. Bathurst and L. Rothenburg, "Micromechanical aspects of isotropic granular assemblies with linear contact interactions", *J. Appl. Mech.* (*ASME*) **55** (1988), 17–23.

[Dekker 1962] A. J. Dekker, *Solid state physics*, Macmillan, London, 1962.

[Els 2011] D. N. J. Els, "Damping of rotating beams with particle dampers: experimental analysis", *AIAA J.* **49** (2011).

[Eringen 1999] A. C. Eringen, *Microcontinuum field theories, I: Foundations and solids*, Springer, New York, 1999.

[Goddard 1990] J. D. Goddard, "Nonlinear elasticity and pressure-dependent wave speeds in granular media", *Proc. R. Soc. Lond. A* **430** (1990), 105–131.

[Horne 1965] M. R. Horne, "The behaviour of an assembly of rotound, rigid, cohesionless particles, I and II", *Proc. R. Soc. Lond. A* **286** (1965), 62–97.

[Jia et al. 1999] X. Jia, C. Caroli, and B. Velicky, "Ultrasound propagation in externally stressed granular media", *Phys. Rev. Lett.* **82** (1999), 1863–1866.

[Johnson 1985] K. L. Johnson, *Contact mechanics*, Cambridge University Press, Cambridge, UK, 1985.

[Kittel 1953] C. Kittel, *Introduction to solid state physics*, Wiley, New York, 1953.

[Kruggel-Emden et al. 2007] H. Kruggel-Emden, E. Simsek, S. Rickelt, S. Wirtz, and V. Scherer, "Review and extension of normal force models for the Discrete Element Method", *Powder Technol.* **171** (2007), 157–173.

[Kruyt 2010] N. P. Kruyt, "Three-dimensional lattice-based dispersion relations for granular materials", pp. 405–415 in *IUTAM-ISIMM Symposium on Mathematical Modelling and Physical Instances of Granular Flows, AIP Conference Proceedings*, vol. 1227, edited by J. D. Goddard et al., 2010.

[Kruyt and Rothenburg 2001] N. P. Kruyt and L. Rothenburg, "Statistics of the elastic behaviour of granular materials", *Int. J. Solids Struct.* **38** (2001), 4879–4899.

[Kruyt and Rothenburg 2002] N. P. Kruyt and L. Rothenburg, "Micromechanical bounds for the elastic moduli of granular materials", *Int. J. Solids Struct.* **39** (2002), 311–324.

[Kruyt et al. 2010] N. P. Kruyt, I. Agnolin, S. Luding, and L. Rothenburg, "Micromechanical study of elastic moduli of loose granular materials", *J. Mech. Phys. Solids* **58**:9 (2010), 1286–1301.

[Kunin 1982] I. A. Kunin, *Elastic media with microstructure, I: One-dimensional models*, Springer Series in Solid-State Sciences **26**, Springer, Berlin, 1982.

[Kunin 1983] I. A. Kunin, *Elastic media with microstructure, II: Three-dimensional models*, Springer Series in Solid-State Sciences **44**, Springer, Berlin, 1983.

[Magnanimo et al. 2008] V. Magnanimo, L. La Ragione, J. T. Jenkins, P. Wang, and H. A. Makse, "Characterizing the shear and bulk moduli of an idealized granular material", *European Physics Letters* **81** (2008). 34006.

[Makse et al. 1999] H. A. Makse, N. Gland, D. L. Johnson, and L. M. Schwartz, "Why effective medium theory fails in granular materials", *Phys. Rev. Lett.* **83** (1999), 5070–5073.

[Makse et al. 2004] H. A. Makse, N. Gland, D. L. Johnson, and L. Schwartz, "Granular packings: nonlinear elasticity, sound propagation, and collective relaxation dynamics", *Phys. Rev. E* **70** (2004), 061302.

[Mindlin 1972] R. D. Mindlin, "Elasticity, piezoelectricity and crystal lattice dynamics", *J. Elasticity* **2** (1972), 217–282.

[Mouraille 2009] O. J. P. Mouraille, *Sound propagation in dry granular materials: discrete element simulations, theory, and experiments*, Ph.D. thesis, Department of Mechanical Engineering, University of Twente, Enschede, The Netherlands, 2009.

[Myers 1997] H. P. Myers, *Introductory solid state physics*, Taylor & Francis, London, 1997.

[O'Sullivan 2011] O'Sullivan, *Particulate discrete element modelling: a geomechanics perspective*, Spon Press, London, 2011.

[Schwager and Pöschel 2007] T. Schwager and T. Pöschel, "Coefficient of restitution and linear-dashpot model revisited", *Granular Matter* **9** (2007), 465–469.

[Schwager et al. 2008] T. Schwager, V. Becker, and T. Pöschel, "Coefficient of tangential restitution for visco-elastic spheres", *Eur. Phys. J. E* **27** (2008), 107–114.

[Schwartz et al. 1984] L. M. Schwartz, D. L. Johnson, and S. Feng, "Vibrational modes in granular materials", *Phys. Rev. Lett.* **52** (1984), 831–834.

[Suiker and de Borst 2005] A. S. J. Suiker and R. de Borst, "Enhanced continua and discrete lattices for modelling granular assemblies", *Philos. Trans. R. Soc. Lond. A* **363**:1836 (2005), 2543–2580.

[Suiker et al. 2001] A. S. J. Suiker, A. V. Metrikine, and R. de Borst, "Comparison of wave propagation characteristics of the Cosserat continuum model and corresponding discrete lattice models", *Int. J. Solids Struct.* **38** (2001), 1563–1583.

[Tisseur and Meerbergen 2001] F. Tisseur and K. Meerbergen, "The quadratic eigenvalue problem", *SIAM Rev.* **43**:2 (2001), 235–286.

[Wu et al. 2003] C. Y. Wu, C. Thornton, and L. Y. Li, "Coefficients of restitution for elasto-plastic oblique impacts", *Adv. Powder Tech.* **14** (2003), 435–448.

Received 10 Oct 2011. Revised 23 Jan 2012. Accepted 7 Feb 2012.

NIELS P. KRUYT: n.p.kruyt@utwente.nl
Department of Mechanical Engineering, University of Twente, P.O. Box 217, 7500 AE Enschede, Netherlands

JOURNAL OF MECHANICS OF MATERIALS AND STRUCTURES
Vol. 7, No. 4, 2012

BUCKLING INSTABILITIES OF ELASTICALLY CONNECTED TIMOSHENKO BEAMS ON AN ELASTIC LAYER SUBJECTED TO AXIAL FORCES

VLADIMIR STOJANOVIĆ, PREDRAG KOZIĆ AND GORAN JANEVSKI

We study the buckling instability of a system of three simply supported elastic Timoshenko beams, joined together by Winkler elastic layers, and each subjected to the same compressive axial load. The model of the Timoshenko beam includes the effects of axial loading, shear deformation, and rotary inertia. Explicit analytical expressions are derived for the critical buckling load of single, double, and triple-beam systems. It can be observed from these expressions that the critical buckling load depends on the Winkler elastic layer stiffness modulus K, and that the instability of the system increases with an increase in the numbers of beams and elastic layers. These results are of considerable practical interest and have wide application in engineering practice.

1. Introduction

Vibration and buckling problems of beams and beam-columns on elastic layers occupy an important place in many fields of structural and layer engineering, occurring often in mechanical and civil engineering applications. Their solution demands modeling of the mechanical behavior of the beam, the mechanical behavior of the soil, and the form of the interaction between the beam and the soil.

As far as the beam is concerned, most engineering analyses are based on classical Bernoulli–Euler beam theory, in which straight lines or planes normal to the neutral beam axis remain straight and normal after deformation. This theory thus neglects the effect of transverse shear deformations, a condition that holds only in the case of slender beams. To confront this problem, the well-known Timoshenko beam model, in which the effect of transverse shear deflections is considered, can be used.

Matsunaga [1996] studied the buckling instabilities of a simply supported thick elastic beam subjected to axial stresses. Taking into account the effects of shear deformations and thickness changes, the buckling loads and buckling displacement modes of thick beams were obtained. Based on the power series expansion of displacement components, a set of fundamental equations of a one-dimensional higher-order beam theory was derived through the principle of virtual displacement. Several sets of truncated approximate theories were applied to solve the eigenvalue problems for a thick beam. The convergence properties of the buckling loads of a simply supported thick beam were examined in detail and comparison of the results with previously published ones was made.

On the basis of the Bernoulli–Euler beam theory, the properties of free transverse vibration and buckling of a double-beam system under compressive axial loading were investigated in [Zhang et al. 2008]. Explicit expressions were derived for the natural frequencies and the associated amplitude ratios of the two beams, and analytical solutions for the critical buckling load were obtained. The influence of the

Research supported by the Ministry of Science and Environmental Protection of the Republic of Serbia, grant No. ON 174011.
Keywords: Timoshenko beam, Winkler elastic layer, shear deformation, rotary inertia, boundary conditions.

compressive axial loading on the response of the double-beam system was discussed. It was shown that the critical buckling load of the system was related to the axial compression ratio of the two beams and the Winkler elastic layer, and that the properties of free transverse vibration of the system greatly depended on the axial compressions.

Kelly and Srinivas [2009] investigated the problem concerning free vibration of a set of n axially loaded stretched Bernoulli–Euler beams connected by elastic layers and connected to a Winkler type layer. A normal-mode solution was applied to the governing partial differential equations to derive a set of coupled ordinary differential equations which were used to determine the natural frequencies and mode shapes. It was shown that the set of differential equations could be written in self-adjoint form with an appropriate inner product. An exact solution for the general case was obtained, but numerical procedures had to be used to determine the natural frequencies and mode shapes. The numerical procedure was difficult to apply, especially in determining higher frequencies. For the special case of identical beams, an exact expression for the natural frequencies was obtained in terms of the natural frequencies of a corresponding set of unstretched beams and the eigenvalues of the coupling matrix.

Stojanović et al. [2011] studied the influence of rotary inertia and shear on the free vibration and buckling of a double-beam system under axial loading. It was assumed that the system under consideration was composed of two parallel and homogeneous simply supported beams continuously joined by a Winkler elastic layer. Both beams had the same length. It was also supposed that the buckling could only occur in the plane where the double-beam system lay. Explicit expressions were derived for the natural frequencies and the associated amplitude ratio of the two beams, and the analytical solution of the critical buckling was obtained. The influence of the characteristics of the Winkler elastic layer on the natural frequencies and the critical buckling force was determined.

Li et al. [2008] analyzed an exact dynamic stiffness matrix which was established for an elastically connected three-beam system, composed of three parallel beams of uniform properties with uniformly distributed springs connecting them. The formulation included the effects of shear deformation and rotary inertia of the beams. The dynamic stiffness matrix was derived by rigorous use of the analytical solutions of the governing differential equations of motion of the three-beam system in free vibration. The use of the dynamic stiffness matrix to study the three vibration characteristics of the three-beam system was demonstrated by applying the Muller root-search algorithm.

De Rosa [1995] studied the free vibration frequencies of Timoshenko beams on a two-parameter elastic layer. Two variants of the equation of motion were deduced, in which the second-layer parameter was a function of the total rotation of the beam or a function of the rotation due to bending only.

Lazopoulos and Lazopoulos [2011], considering the influence of the microstructure, revisited the Timoshenko beam model, invoking Mindlin's strain gradient strain energy density function. The equations of motion were derived and the bending equilibrium equations were discussed. The solution of the static problem, for a simply supported beam loaded by a force at the middle of the beam, was defined and the first (least) eigenfrequency was found.

Miranda and Taghavi [2005] presented an approximate procedure to estimate floor acceleration demands in multistory buildings with the use of only a small number of parameters. Floor acceleration demands were computed using approximations of the first three modes of vibration of the building based on those of a continuum model consisting of a cantilever flexural beam connected laterally to a cantilever shear beam. The models had uniform stiffness along the height.

In this paper, the buckling instability of simply supported elastic Timoshenko beams, continuously joined by Winkler elastic layers, subjected to the same compressive axial load is studied. The beams have the same length l, and it is also supposed that the buckling can only occur in the plane where the system beams lie. The model of the Timoshenko beams includes the effects of axial loading, shear deformation, and rotary inertia. Explicit analytical expressions are determined for the critical buckling load of single, double, and triple-beam models. The critical buckling load for the triple-beam model is also determined using the trigonometric method. It can be observed from these expressions that the critical buckling load depends on the Winkler elastic layer stiffness modulus K, and that the instability of the system increases with an increase in the numbers of beams and elastic layers.

2. Formulation of the differential equations of the dynamic equilibrium and structural model

It can be seen that the literature on the dynamic analysis of elastically parallel-beam systems is concentrated primarily on the case of a double-beam system of two parallel simply supported beams continuously joined by a Winkler elastic layer. Very few research papers can be found that deal with the problem related to the elastically connected three-beam system. Those studies of this region are limited to the particular cases of identical beams with some prescribed boundary conditions. In most of these references, the simple Bernoulli–Euler beam theory has been used in deriving the necessary equation. Here, the basic differential equations of motion for the analysis will be deduced by considering a Timoshenko beam of length l (Figure 1a) subjected to an axial compressive force F, and to distributed lateral loads of intensity q_1 and q_2 which vary with the distance z along the beam. This will be applied on the basis of several assumptions:

- The behavior of the beam material is linear elastic.
- The cross-section is rigid and constant throughout the length of the beam and has one plane of symmetry.

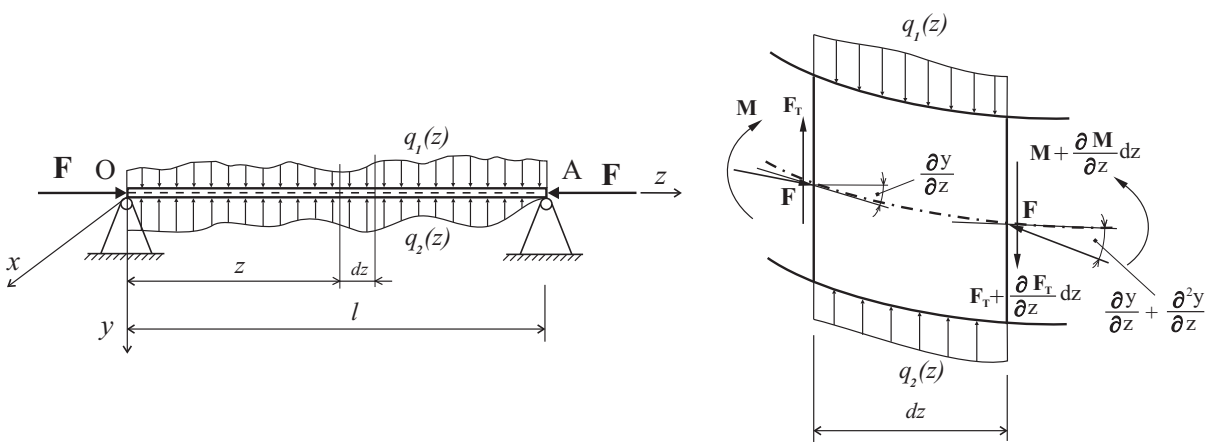

(a) (b)

Figure 1. The physical model Timoshenko beam subjected to an axial compressive force F and to distributed lateral loads of intensity q_1 and q_2.

- Shear deformations of the cross-section of the beam are taken into account while elastic axial deformations are ignored.
- The equations are derived bearing in mind the geometric axial deformations.
- The axial forces F acting on the ends of the beam are not changed with time.

Consider the element of length dz between two cross-sections normal to the deflected axis of the beam (Figure 1b). Since the slope of the beam is small, the normal forces acting on the sides of the element can be taken as equal to the axial compressive force F. The shearing force F_T is related to the following relationship:

$$F_T = kGA\left(\frac{\partial w}{\partial z} - \psi\right), \tag{1}$$

where $w = w(z, t)$ is the displacement of a cross-section in the y-direction, $\partial w/\partial z$ is the global rotation of the cross-section, ψ is the bending rotation, G is the shear modulus, A is the area of the beam cross-section, and k is the shear factor. Analogously the relationship between bending moments M and bending angles $\psi = \psi(z, t)$ is given by

$$M = -EI_x \frac{\partial \psi}{\partial z}, \tag{2}$$

where E is the Young's modulus and I_x is the second moment of the area of the cross-section. Finally, the forces and moments of inertia are given by

$$f_I = -\rho A \frac{\partial^2 w}{\partial t^2}, \quad J_I = -\rho I_x \frac{\partial^2 \psi}{\partial t^2}, \tag{3}$$

respectively, where ρ is the mass density.

The forces acting on a differential layered-beam element are shown in Figure 1b. The dynamic-force equilibrium conditions of these forces are given by the following equations:

$$\rho A \frac{\partial^2 w}{\partial t^2} - kGA\left(\frac{\partial^2 w}{\partial z^2} - \frac{\partial \psi}{\partial z}\right) + F\frac{\partial^2 w}{\partial z^2} - q_1(z) + q_2(z) = 0, \tag{4a}$$

$$\rho I_x \frac{\partial^2 \psi}{\partial t^2} - EI_x \frac{\partial^2 \psi}{\partial z^2} - kGA\left(\frac{\partial w}{\partial z} - \psi\right) = 0. \tag{4b}$$

The development and solution of the differential equations of motion governing the free flexural vibrations of a system of three identical elastically connected beams, considering the effects of shear deformation and rotary inertia (Figure 2).

Each beam is made of material with a Young's modulus E and mass density ρ, and has a uniform cross-section of area A and moment of inertia $I = I_x$. Each beam is subjected to the same compressive axial loading. The first beam is connected to a Winkler layer of stiffness modulus K, and the second and third beams are also connected by a continuous linear elastic layer of Winkler type of the same stiffness modulus K. The transverse displacement of the beams is $w_i = w_i(z, t)$, $i = 1, 2, 3$, and $\psi_i = \psi_i(z, t)$, $i = 1, 2, 3$, are the bending rotations. If we apply the abovementioned procedure to a differential element

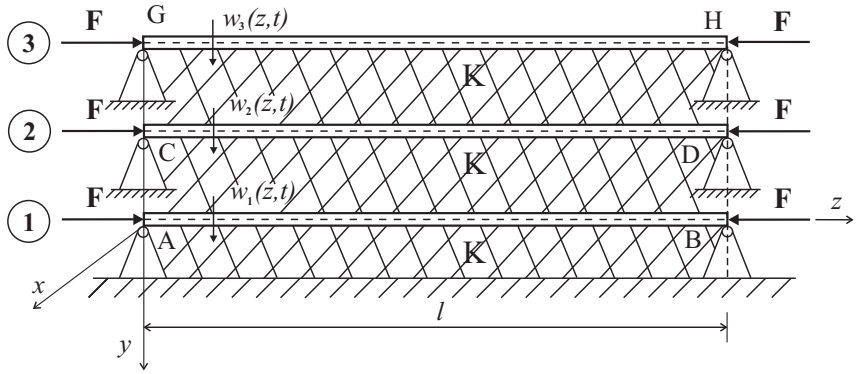

Figure 2. Three identical Timoshenko beams supported on a Winkler elastic layer.

of each beam, the following set of coupled differential equations will be obtained:

$$\begin{aligned} \rho A\frac{\partial^2 w_1}{\partial t^2} - kGA\left(\frac{\partial^2 w_1}{\partial z^2} - \frac{\partial \psi_1}{\partial z}\right) + F\frac{\partial^2 w_1}{\partial z^2} + 2Kw_1 - Kw_2 = 0, \\ \rho I\frac{\partial^2 \psi_1}{\partial t^2} - EI\frac{\partial^2 \psi_1}{\partial z^2} - kGA\left(\frac{\partial w_1}{\partial z} - \psi_1\right) = 0, \end{aligned} \tag{5}$$

$$\begin{aligned} \rho A\frac{\partial^2 w_2}{\partial t^2} - kGA\left(\frac{\partial^2 w_2}{\partial z^2} - \frac{\partial \psi_2}{\partial z}\right) + F\frac{\partial^2 w_2}{\partial z^2} - Kw_1 + 2Kw_2 - Kw_3 = 0, \\ \rho I\frac{\partial^2 \psi_2}{\partial t^2} - EI\frac{\partial^2 \psi_2}{\partial z^2} - kGA\left(\frac{\partial w_2}{\partial z} - \psi_2\right) = 0, \end{aligned} \tag{6}$$

$$\begin{aligned} \rho A\frac{\partial^2 w_3}{\partial t^2} - kGA\left(\frac{\partial^2 w_3}{\partial z^2} - \frac{\partial \psi_3}{\partial z}\right) + F\frac{\partial^2 w_3}{\partial z^2} - Kw_2 + Kw_3 = 0, \\ \rho I\frac{\partial^2 \psi_3}{\partial t^2} - EI\frac{\partial^2 \psi_3}{\partial z^2} - kGA\left(\frac{\partial w_3}{\partial z} - \psi_3\right) = 0. \end{aligned} \tag{7}$$

3. The axial buckling load of the elastically connected identical three Timoshenko beams

The stability behavior of simply supported Timoshenko-beam systems on a Winkler elastic layer is of great interest to both practicing engineers and researchers. The usual approach to formulating this problem is to include the layer reaction in the corresponding differential equation of the beam. The buckling of an elastically connected simply supported Timoshenko beam under some static compressive axial load is investigated. The analytical solution for the critical buckling load of the system is derived. The second-order partial differential equations (5), (6), and (7) can be further reduced, by eliminating ψ_1, ψ_2, and ψ_3, respectively, to the following system of fourth-order partial differential equations:

$$\begin{aligned} EI\left(1 - \frac{F}{kAG}\right)\frac{\partial^4 w_1}{\partial z^4} + \left(\rho A + 2\frac{K\rho I}{kAG}\right)\frac{\partial^2 w_1}{\partial t^2} - \frac{K\rho I}{kAG}\frac{\partial^2 w_2}{\partial t^2} + \left(F - 2\frac{KEI}{kAG}\right)\frac{\partial^2 w_1}{\partial z^2} \\ + \frac{KEI}{kAG}\frac{\partial^2 w_2}{\partial z^2} - \left(\rho I + \frac{\rho EI}{kG} - \frac{F\rho I}{kAG}\right)\frac{\partial^4 w_1}{\partial z^2 \partial t^2} + \frac{\rho^2 I}{kG}\frac{\partial^4 w_1}{\partial t^4} + 2Kw_1 - Kw_2 = 0, \end{aligned} \tag{8a}$$

$$EI\left(1-\frac{F}{kAG}\right)\frac{\partial^4 w_2}{\partial z^4}-\frac{K\rho I}{kAG}\frac{\partial^2 w_1}{\partial t^2}+\left(\rho A+2\frac{K\rho I}{kAG}\right)\frac{\partial^2 w_2}{\partial t^2}-\frac{K\rho I}{kAG}\frac{\partial^2 w_3}{\partial t^2}+\frac{KEI}{kAG}\frac{\partial^2 w_1}{\partial z^2}+\left(F-\frac{KEI}{kAG}\right)\frac{\partial^2 w_2}{\partial z^2}$$
$$+\frac{KEI}{kAG}\frac{\partial^2 w_3}{\partial z^2}-\left(\rho I+\frac{\rho EI}{kG}-\frac{F\rho I}{kAG}\right)\frac{\partial^4 w_2}{\partial z^2\partial t^2}+\frac{\rho^2 I}{kG}\frac{\partial^4 w_2}{\partial t^4}-Kw_1+2Kw_2-Kw_3=0, \quad (8b)$$

$$EI\left(1-\frac{F}{kAG}\right)\frac{\partial^4 w_3}{\partial z^4}-\frac{K\rho I}{kAG}\frac{\partial^2 w_2}{\partial t^2}+\left(\rho A+\frac{K\rho I}{kAG}\right)\frac{\partial^2 w_3}{\partial t^2}+\frac{KEI}{kAG}\frac{\partial^2 w_2}{\partial z^2}+\left(F-\frac{KEI}{kAG}\right)\frac{\partial^2 w_3}{\partial z^2}$$
$$-\left(\rho I+\frac{\rho EI}{kG}-\frac{F\rho I}{kAG}\right)\frac{\partial^4 w_3}{\partial z^2\partial t^2}+\frac{\rho^2 I}{kG}\frac{\partial^4 w_3}{\partial t^4}-Kw_2+Kw_3=0. \quad (8c)$$

The initial conditions in general form and the boundary conditions for simply supported beams of the same length l are assumed as follows:

$$w_i(z,0)=w_{i0}(z), \quad \dot{w}_i(z,0)=v_{i0}(z), \quad \psi_i(z,0)=\psi_{i0}(z), \quad \dot{\psi}_i(z,0)=\omega_{i0}(z), \quad (9)$$

$$w_i(z,0)=w_i''(0,t)=w_i(l,0)=w_i''(l,t)=0, \quad i=1,2,3. \quad (10)$$

Assuming time-harmonic motion and using the separation of variables and the solutions of (8), the governing boundary conditions (10) can be written in the form

$$w_i(z,t)=\sum_{n=1}^{\infty}X_n(z)T_{in}(t), \quad i=1,2,3, \quad (11)$$

where $T_{in}(t)$, $i=1,2,3$, is the unknown time function and $X_n(z)$ is the known mode shape function for a simply supported single beam, which is defined as

$$X_n(x)=\sin(k_n z), \quad k_n=n\pi/l, \quad n=1,2,3,\ldots. \quad (12)$$

Introducing the general solutions (11) into (8) one gets the system of ordinary differential equations

$$\sum_{n=1}^{\infty}\left\{\frac{1}{C_s^2}\frac{d^4T_{1n}}{dt^4}+\left[1+C_r^2k_n^2\left(1+\frac{C_b^2}{C_s^2C_r^4}\right)+\frac{1}{C_s^2}(2H-F\eta)\right]\frac{d^2T_{1n}}{dt^2}\right.$$
$$\left.-\frac{H}{C_s^2}\frac{d^2T_{2n}}{dt^2}+\left[C_b^2k_n^4+(2H-F\eta)\left(1+\frac{C_b^2}{C_s^2C_r^2}k_n^2\right)\right]T_{1n}-H\left(1+\frac{C_b^2}{C_s^2C_r^2}k_n^2\right)T_{2n}\right\}=0, \quad (13a)$$

$$\sum_{n=1}^{\infty}\left\{\frac{1}{C_s^2}\frac{d^4T_{2n}}{dt^4}-\frac{H}{C_s^2}\frac{d^2T_{1n}}{dt^2}+\left[1+C_r^2k_n^2\left(1+\frac{C_b^2}{C_s^2C_r^4}\right)+\frac{1}{C_s^2}(2H-F\eta)\right]\frac{d^2T_{2n}}{dt^2}-\frac{H}{C_s^2}\frac{d^2T_{3n}}{dt^2}\right.$$
$$\left.-H\left(1+\frac{C_b^2}{C_s^2C_r^2}k_n^2\right)T_{1n}+\left[C_b^2k_n^4+(2H-F\eta)\left(1+\frac{C_b^2}{C_s^2C_r^2}k_n^2\right)\right]T_{2n}-H\left(1+\frac{C_b^2}{C_s^2C_r^2}k_n^2\right)T_{3n}\right\}=0, \quad (13b)$$

$$\sum_{n=1}^{\infty}\left\{\frac{1}{C_s^2}\frac{d^4T_{3n}}{dt^4}-\frac{H}{C_s^2}\frac{d^2T_{2n}}{dt^2}+\left[1+C_r^2k_n^2\left(1+\frac{C_b^2}{C_s^2C_r^4}\right)+\frac{1}{C_s^2}(H-F\eta)\right]\frac{d^2T_{3n}}{dt^2}\right.$$
$$\left.-H\left(1+\frac{C_b^2}{C_s^2C_r^2}k_n^2\right)T_{2n}+\left[C_b^2k_n^4+(H-F\eta)\left(1+\frac{C_b^2}{C_s^2C_r^2}k_n^2\right)\right]T_{3n}\right\}=0, \quad (13c)$$

where

$$H = \frac{K}{\rho A}, \quad \eta = \frac{k_n^2}{\rho A}.$$

The coefficients

$$C_b = \sqrt{\frac{EI}{\rho A}}, \quad C_s = \sqrt{\frac{GAk}{\rho I}}, \quad C_r = \sqrt{\frac{I}{A}},$$

related to the bending stiffness, shear stiffness, and rotational effects, respectively, are now introduced. The shear beam model, the Rayleigh beam model, and the simple Euler beam model can be obtained from the Timoshenko beam model by setting C_r to zero (that is, ignoring the rotational effect), C_s to infinity (ignoring the shear effect), and setting both C_r to zero and C_s to infinity, respectively.

The solutions of (13a), (13b), and (13c) can be assumed to have the following forms:

$$T_{1n} = A_{1n}e^{j\omega_n t}, \quad T_{2n} = A_{2n}e^{j\omega_n t}, \quad T_{3n} = A_{3n}e^{j\omega_n t}, \quad j = \sqrt{-1}, \tag{14}$$

where ω_n denotes the natural frequency of the system. Substituting (14) into (13) results in the following system of homogeneous algebraic equations for the unknown constants A_{1n}, A_{2n}, and A_{3n}:

$$\left\{\frac{\omega_n^4}{C_s^2} - \left[1 + C_r^2 k_n^2\left(1 + \frac{C_b^2}{C_s^2 C_r^4}\right) + \frac{1}{C_s^2}(2H - F\eta)\right]\omega_n^2 + \left[C_b^2 k_n^4 + (2H - F\eta)\left(1 + \frac{C_b^2}{C_s^2 C_r^2}k_n^2\right)\right]\right\}A_{1n} + H\left[\frac{\omega_n^2}{C_s^2} - \left(1 + \frac{C_b^2}{C_s^2 C_r^2}k_n^2\right)\right]A_{2n} = 0, \tag{15a}$$

$$H\left[\frac{\omega_n^2}{C_s^2} - \left(1 + \frac{C_b^2}{C_s^2 C_r^2}k_n^2\right)\right]A_{1n} + \left\{\frac{\omega_n^4}{C_s^2} - \left[1 + C_r^2 k_n^2\left(1 + \frac{C_b^2}{C_s^2 C_r^4}\right) + \frac{1}{C_s^2}(2H - F\eta)\right]\omega_n^2 + \left[C_b^2 k_n^4 + (2H - F\eta)\left(1 + \frac{C_b^2}{C_s^2 C_r^2}k_n^2\right)\right]\right\}A_{2n} + H\left[\frac{\omega_n^2}{C_s^2} - \left(1 + \frac{C_b^2}{C_s^2 C_r^2}k_n^2\right)\right]A_{3n} = 0, \tag{15b}$$

$$H\left[\frac{\omega_n^2}{C_s^2} - \left(1 + \frac{C_b^2}{C_s^2 C_r^2}k_n^2\right)\right]A_{2n} + \left\{\frac{\omega_n^4}{C_s^2} - \left[1 + C_r^2 k_n^2\left(1 + \frac{C_b^2}{C_s^2 C_r^4}\right) + \frac{1}{C_s^2}(H - F\eta)\right]\omega_n^2 + \left[C_b^2 k_n^4 + (H - F\eta)\left(1 + \frac{C_b^2}{C_s^2 C_r^2}k_n^2\right)\right]\right\}A_{3n} = 0. \tag{15c}$$

Equations (15) have nontrivial solutions when the determinant of the system matrix coefficients of A_{1n}, A_{2n}, and A_{3n} is zero. This yields the following frequency (characteristic) equation, which is a twelfth-order polynomial in ω_n. When the natural frequency of the system vanishes under the axial loading, the system begins to buckle. By introducing $\omega_n = 0$ into (15) expressed in matrix form one gets

$$\begin{bmatrix} x + 2RH & -HR & 0 \\ -HR & x + 2RH & -HR \\ 0 & -HR & x + RH \end{bmatrix} \begin{Bmatrix} A_{1n} \\ A_{2n} \\ A_{3n} \end{Bmatrix} = 0, \tag{16}$$

where

$$R = 1 + \frac{C_b^2}{C_s^2 C_r^2}k_n^2, \quad x = C_b^2 k_n^4 - RF\eta. \tag{17}$$

The existence of nontrivial solutions for A_{1n}, A_{2n}, and A_{3n} requires that the determinant of the coefficient matrix vanish. This gives the cubic characteristic equation $x^3 + 5RHx^2 + 6(RH)^2x + (RH)^3 = 0$, or

$$\left(\frac{x}{RH}\right)^3 + 5\left(\frac{x}{RH}\right)^2 + 6\left(\frac{x}{RH}\right) + 1 = 0. \tag{18}$$

Solution of the characteristic equation. We solve (18) using a standard method. Denote the coefficients by $a_0 = 1,\ a_1 = 5,\ a_2 = 6$, and $a_3 = 1$, and set

$$p = \frac{a_2}{a_0} - \frac{a_1^2}{3a_0^2} \quad \text{and} \quad q = \frac{a_3}{a_0} - \frac{a_1 a_2}{3a_0^2} + \frac{2a_1^3}{27a_0^3}. \tag{19}$$

The discriminant $D = \frac{1}{4}q^2 + \frac{1}{27}p^3$ is negative, so there are three roots for $x/(RH)$, given by

$$-\frac{a_1}{3a_0} + 2\sqrt{-\frac{p}{3}}\cos\frac{\theta + 2k\pi}{3}, \quad \text{with } \theta = \cos^{-1}\left[-\frac{q}{2}\left(-\frac{p}{3}\right)^{-\frac{3}{2}}\right] \text{ and } k = 0, 1, 2.$$

Thus the roots are

$$\frac{x_1}{RH} = -0.19806, \quad \frac{x_2}{RH} = -1.55496, \quad \frac{x_3}{RH} = -3.24698. \tag{20}$$

Substituting into (17), we obtain the buckling loads for different vibration modes n:

$$F_b^{\mathrm{I}} = \frac{0.198062H}{\eta} + \frac{C_b^2 k_n^4}{R\eta}, \quad F_b^{\mathrm{II}} = \frac{1.554962H}{\eta} + \frac{C_b^2 k_n^4}{R\eta}, \quad F_b^{\mathrm{III}} = \frac{3.24698H}{\eta} + \frac{C_b^2 k_n^4}{R\eta}. \tag{21}$$

As can be seen, the values of the buckling loads F_b^{I}, F_b^{II}, and F_b^{III} are positive and $F_b^{\mathrm{I}} < F_b^{\mathrm{II}} < F_b^{\mathrm{III}}$. Thus F_b^{I} is the critical buckling load:

$$F_b^{\mathrm{cr}} = \frac{0.198062Kl^2}{\pi^2 n^2} + \frac{EI\pi^2 n^2}{l^2\left(1 + \dfrac{EI}{GAk}\dfrac{\pi^2 n^2}{l^2}\right)}. \tag{22}$$

For $K = 0$ from (22) we obtain

$$P_n = \frac{EI\pi^2 n^2}{l^2\left(1 + \dfrac{EI}{GAk}\dfrac{\pi^2 n^2}{l^2}\right)},$$

which is the critical buckling load corresponding to the number n of the Timoshenko beams as shown in [Timoshenko and Gere 1964, p. 134]. Setting $n = 1$ in the preceding equation we obtain

$$P = \frac{EI\pi^2}{l^2\left(1 + \dfrac{EI}{GAk}\dfrac{\pi^2}{l^2}\right)}.$$

This is the smallest load at which the beam ceases to be in stable equilibrium.

Remark. An alternative, but equivalent, method of solution is given in [Rašković 1965, pp. 157–166].

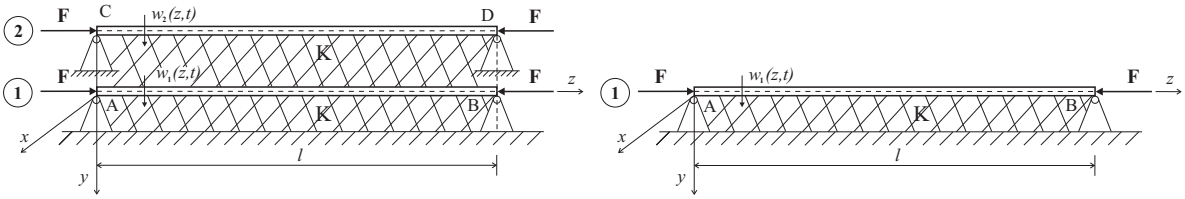

Figure 3. Left: system with two identical Timoshenko beams supported on a Winkler elastic layer. Right: analogous system with a single Timoshenko beam.

Critical buckling load for system with fewer Timoshenko beams. The preceding analysis was also applied to a system with two beams instead of three (Figure 3, left) and a system with a single beam resting on a Winkler elastic layer (Figure 3, right). The computation is easier in these cases, in that the characteristic equation is quadratic or linear, respectively. For the case of two beams we get

$$F_b^{\mathrm{I}} = \frac{0.382H}{\eta} + \frac{C_b^2 k_n^4}{R\eta}, \qquad F_b^{\mathrm{II}} = \frac{2.618H}{\eta} + \frac{C_b^2 k_n^4}{R\eta};$$

thus F_b^{I} is the critical buckling load corresponding to vibration mode n for this system:

$$F_b^{\mathrm{cr}} = \frac{0.382Kl^2}{\pi^2 n^2} + \frac{EI\pi^2 n^2}{l^2\left(1 + \dfrac{EI}{GAk}\dfrac{\pi^2 n^2}{l^2}\right)}. \tag{23}$$

For the case of a single beam we have

$$F_b^{\mathrm{cr}} = \frac{Kl^2}{\pi^2 n^2} + \frac{EI\pi^2 n^2}{l^2\left(1 + \dfrac{EI}{GAk}\dfrac{\pi^2 n^2}{l^2}\right)}. \tag{23a}$$

4. Numerical results

We ran numerical calculations for the system with parameters

$$\begin{gathered} E = 1\times 10^{10}\,\mathrm{Nm}^{-2}, \quad G = 0.417\times 10^{10}\,\mathrm{Nm}^{-2}, \quad k = 5/6, \quad K_0 = 2\times 10^5\,\mathrm{Nm}^{-2}, \\ \rho = 2\times 10^3\,\mathrm{kgm}^{-3}, \quad l = 10\,\mathrm{m}, \quad A = 5\times 10^{-2}\,\mathrm{m}^2, \quad I = 4\times 10^{-4}\,\mathrm{m}^4, \end{gathered} \tag{24}$$

as in [Zhang et al. 2008]. If we introduce a nondimensional value $\xi = h/l$, the ratio of the cross-sectional height h to the beam length l, we can write the surface and moment of inertia of the cross-section of the beam as a function of the nondimensional value ξ as

$$A = h^2 = (\xi l)^2, \qquad I = \frac{h^4}{12} = \frac{(\xi l)^4}{12}. \tag{25}$$

The change in the critical buckling load in the function of the nondimensional value ξ is given in Figures 4 and 5. These diagrams represent the variation of the critical buckling load for systems with triple, double, and single Timoshenko beams obtained by analytical expressions (22), (23), and (23a) for the different parameters of the system (24). Figure 4 shows the diagrams obtained for different values of the stiffness

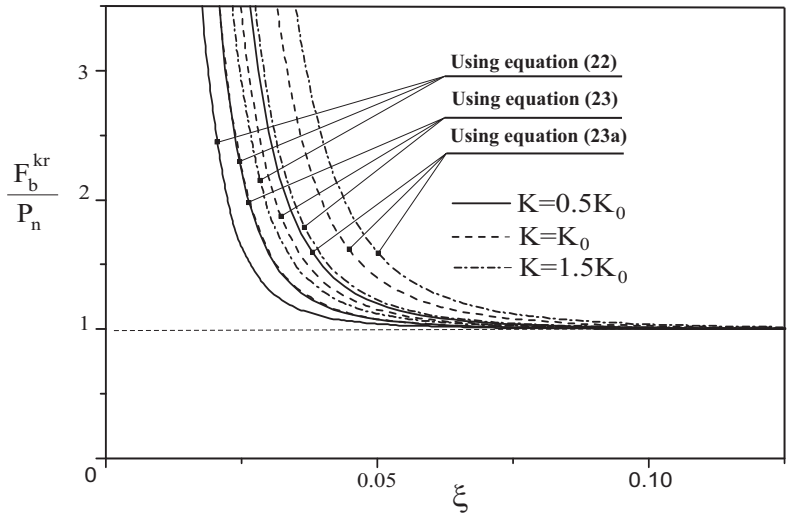

Figure 4. Effect of the nondimensional value ξ on the critical buckling load F_b^{cr} for different values of K and $n = 1$.

modulus $K = 0.5K_0$, K_0, and $1.5K_0$ and for vibration mode $n = 1$. It can be seen that the critical buckling load increases with an increase in the stiffness modulus K. Figure 5 shows diagrams of the critical buckling load for different values of the vibration mode $n = 1, 2, 3$, and for stiffness modulus $K = K_0$. It can be seen that the critical buckling load decreases with an increase in the vibration mode n.

In Figure 6, the static stability regions for the first vibration mode $n = 1$ are represented for systems with triple, double, and single Timoshenko beams supported on a Winkler elastic layer. It can be seen that the static stability region is largest in the case of a single beam. For the system with two beams, the static stability region is reduced, and even more so for three beams.

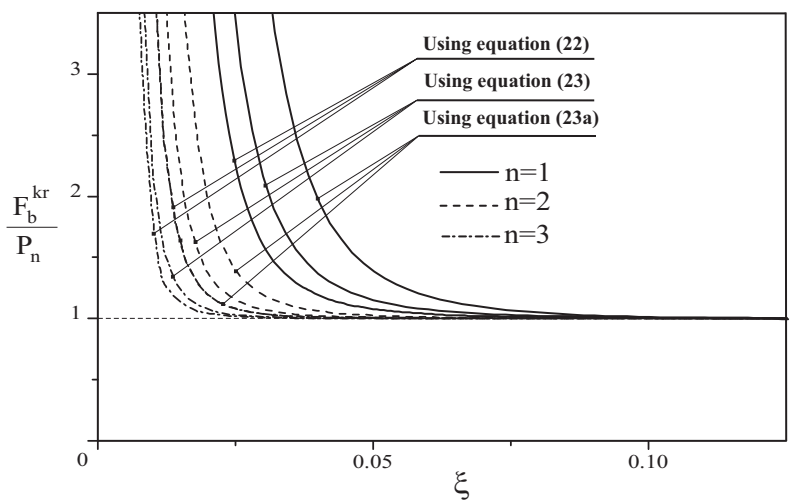

Figure 5. Effect of the nondimensional value ξ on the critical buckling load F_b^{cr} for different values of n and $K = K_0$.

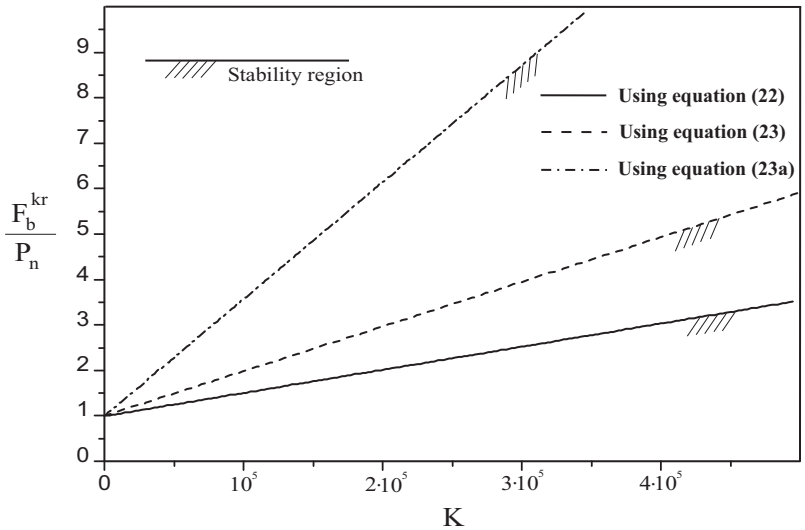

Figure 6. Influence of the stiffness modulus K on the static stability region for $n = 1$.

Conclusions

In the present paper, the equations of dynamic equilibrium and the equations of natural vibration of a triple Timoshenko beam elastically connected to a Winkler elastic layer are formulated. In order to derive these equations, the influence of constant axial forces at the ends of the same beams (second-order theory), as well as the influence of the elastic layer on the beams, are taken into account. Using the classical Bernoulli–Fourier method, the solutions of the differential equations of motion for the system are formulated. The explicit expressions for the critical buckling loads of the systems with triple, double, and single Timoshenko beams are obtained. The critical buckling load for the triple-beam model is also determined using the trigonometric method. The thus determined values for the critical buckling load are only slightly different from the values determined by the numerical solution of the characteristic equation. It is observed from the numerical results that the static stability region is influenced by the Winkler layer of stiffness modulus K and the number of Timoshenko beams. The static stability region of the triple and double-Timoshenko-beam systems is always smaller than that of the single-beam system. It can be concluded that an increase in the number of elastically connected Timoshenko beams leads to a reduction of the static stability region for the same system parameters.

References

[De Rosa 1995] M. A. De Rosa, "Free vibrations of Timoshenko-beams on two-parameter elastic foundation", *Comput. Struct.* **57** (1995), 151–156.

[Kelly and Srinivas 2009] G. S. Kelly and S. Srinivas, "Free vibrations of elastically connected stretched beams", *J. Sound Vib.* **326** (2009), 883–893.

[Lazopoulos and Lazopoulos 2011] K. A. Lazopoulos and K. A. Lazopoulos, "On a strain gradient elastic Timoshenko beam model", *Z. Angew. Math. Mech.* **91**:11 (2011), 875–882.

[Li et al. 2008] J. Li, Y. Chen, and H. Hua, "Exact dynamic stiffness matrix of a Timoshenko three-beam system", *Int. J. Mech. Sci.* **50** (2008), 1023–1034.

[Matsunaga 1996] H. Matsunaga, "Buckling instabilities of thick elastic beams subjected to axial stresses", *Comput. Struct.* **59** (1996), 859–868.

[Miranda and Taghavi 2005] E. Miranda and S. Taghavi, "Approximate floor acceleration demands in multistory buildings, I: Formulation", *J. Struct. Eng.* (*ASCE*) **131** (2005), 203–211.

[Rašković 1965] D. Rašković, *Teorija oscilacija*, Građevinska knjiga, Beograd, 1965. A scan can be found at http://tinyurl.com/RaskovicTeorijaOscilacija.

[Stojanović et al. 2011] V. Stojanović, P. Kozić, R. Pavlović, and G. Janevski, "Effect of rotary inertia and shear on vibration and buckling of a double beam system under compressive axial loading", *Arch. Appl. Mech.* **81**:12 (2011), 1993–2005.

[Timoshenko and Gere 1964] S. P. Timoshenko and J. M. Gere, *Theory of elastic stability*, 2nd ed., McGraw-Hill, 1964.

[Zhang et al. 2008] Q. Y. Zhang, Y. Lu, L. S. Wang, and X. Liu, "Vibration and buckling of a double-beam system under compressive axial loading", *J. Sound Vib.* **318** (2008), 341–352.

Received 2 Nov 2011. Revised 31 Jan 2012. Accepted 2 Feb 2012.

VLADIMIR STOJANOVIĆ: vladast83@yahoo.com
Department of Mechanical Engineering, University of Niš, Univerzitetski trg 2, 18000 Niš, Serbia

PREDRAG KOZIĆ: kozicp@yahoo.com
Department of Mechanical Engineering, University of Niš, Univerzitetski trg 2, 18000 Niš, Serbia

GORAN JANEVSKI: gocky.jane@gmail.com
Department of Mechanical Engineering, University of Niš, Univerzitetski trg 2, 18000 Niš, Serbia

JOURNAL OF MECHANICS OF MATERIALS AND STRUCTURES
Vol. 7, No. 4, 2012

THE EFFECTIVE THICKNESS OF LAMINATED GLASS PLATES

LAURA GALUPPI AND GIANNI ROYER-CARFAGNI

The flexural performance of laminated glass, a composite of two or more glass plies bonded together by polymeric interlayers, depends upon shear coupling between the glass components through the polymer. This effect is usually taken into account, in the design practice, through the definition of the *effective thickness*, i.e., the thickness of a monolith with equivalent bending properties in terms of stress and deflection. The traditional formulas *à la* Bennison–Wölfel are accurate only when the deformed bending shape of the plate is cylindrical and the plate response is similar to that of a beam under uniformly distributed load. Here, assuming approximating shape function for the deformation of laminated plates variously constrained at the edges, minimization of the corresponding strain energy furnishes new simple expressions for the effective thickness, which can be readily used in the design. Comparisons with accurate numerical simulations confirm the accuracy of the proposed simple method for laminated plates.

1. Introduction

Laminated glass is a sandwich structure where two or more glass plies are bonded together by thin polymeric interlayers with a process at high temperature and pressure in autoclave. Because of the shear deformability of the polymer, there is not a perfectly coupling between any two consecutive glass plies [Behr et al. 1993], and the degree of coupling depends upon the shear stiffness of the polymeric interlayer [Hooper 1973]. Consequently, the flexural response is somehow intermediate between the two borderline cases [Norville et al. 1998] of *layered limit*, i.e., frictionless relative sliding of the plies, and *monolithic limit*, i.e., perfect bonding of the plies. This problem has close similarities with the case of composite beams with partial interaction. The most classical contribution, conceived of for a concrete slab and a steel beam bonded by shear connectors, is associated with the name of Newmark et al. [1951], who considered a linear and continuous relationship between the relative interface slip and the corresponding shear stress. More recently Murakami [1984] introduced the usual hypotheses of Timoshenko beam to model the interlayer in the analysis of composite beams. In a recent paper, Xu and Wu [2007] presented a very comprehensive approach for static, dynamic and buckling behavior of composite beams with partial interaction, accounting for the influence of rotary inertia and shear deformation. Approximate formulations of this kind are particularly important for studying the problem of buckling of composite columns (e.g., [Le Grognec et al. 2012; Schnabl and Planinc 2011]), applicable to various materials, including lamellar wood [Cas et al. 2007].

Geometric nonlinearities are usually important because of the slenderness of the laminated panel [Aşik 2003], but are usually negligible when the loads are orthogonal to the panel surface and no in-plane forces are present. From an analytical point of view, it is often very difficult to obtain a closed-form solution for the strain and stress field in a laminated glass plate. An analytical approach has been recently proposed

Keywords: structural glass, laminated glass, composite structure, laminated plate, effective thickness, energy minimization.

by Foraboschi [2012] for the case of rectangular plates made of laminated glass, simply supported on four sides. The precise calculation of the resulting state of stress and strain is quite difficult and usually requires numerical analysis, complicated by the fact that response of the polymer is nonlinear, viscoelastic and temperature dependent [Behr et al. 1993; Bennison et al. 2005; Louter et al. 2010].

This is why simplified methods are becoming more and more popular in the design practice , and much of current research is directed towards their definition and verification [Foraboschi 2007]. Reference is made to [Ivanov 2006] for an updated list of the most relevant current literature.

A commonly accepted simplification is to assume that the polymer is linear elastic, with proper secant elastic moduli that account for environmental temperature and load duration. There are various commercial polymeric films: polyvinyl butyral (PVB), ethylene vinyl acetate (EVA), and sentry glass (SG) [Bennison et al. 2008; Bennison et al. 2001]. Depending upon the polymer type, temperature T and characteristic load-duration t_0, the secant shear modulus of the interlayer may vary from 0.01 MPa (PVB at $T = +60°\text{C}$ under permanent load) up to 300 MPa (SG at $T = 0°\text{C}$ and $t_0 = 1$ s). On the other hand, glass remains linear elastic up to failure (Young's modulus $E \simeq 70$ GPa and Poisson ratio $\nu \simeq 0.2$).

A simplified method of very practical value makes use the notion of "effective" thickness. This method has been introduced starting from the analysis for sandwich beams with linear elastic components originally developed by Wölfel [1987] and later transferred to the case of laminated glass [Bennison 2009; Calderone et al. 2009]. To illustrate, consider (as in Figure 1) a beam of length l and width b composed of two external glass plies of thickness h_1 and h_2 and Young's modulus E, bonded by a soft polymeric interlayer of thickness t and elastic shear modulus G. The latter has negligible axial and bending strength, but nevertheless it can transfer shear coupling stresses between the external layers. Let

$$A_i = h_i b, \quad I_i = \tfrac{1}{12} b h_i^3 \ \ (i = 1, 2), \quad H = t + \tfrac{1}{2}(h_1 + h_2), \quad A^* = \frac{A_1 A_2}{A_1 + A_2},$$
$$I_{\text{tot}} = I_1 + I_2 + A^* H^2, \quad A = bt, \quad B_s = E A^* H^2. \tag{1-1}$$

Clearly, I_{tot} is the cross sectional inertia of the composing glass layers properly spaced of the interlayer gaps, associated with the case of perfect bonding of the glass plies as in Bennison et al. [1999] (monolithic limit). Besides, B_s is the bending stiffness when the external layers have negligible inertia, while the mid-layer can only bear shear stress. When, as in the case of laminated glass, the external layers have

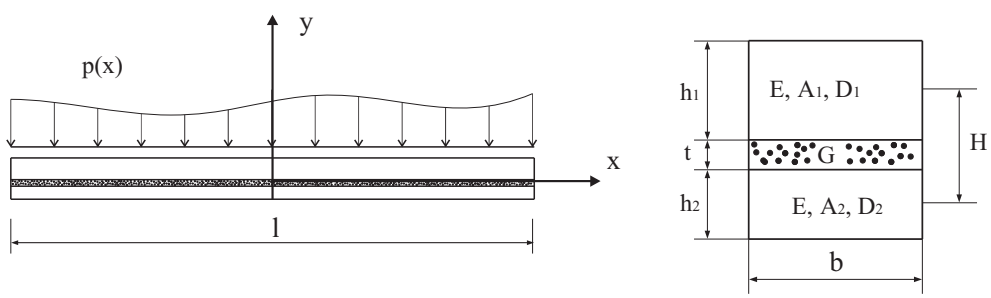

Figure 1. Beam composed of two glass plies bonded by a polymeric interlayer. Longitudinal and cross sectional view (not in the same scale).

nonnegligible inertia, Wölfel proposed the expression B_s^* defined as

$$B_s^* = EI_1 + EI_2 + \frac{1}{1+\mathcal{K}} B_s, \tag{1-2}$$

where the coefficient $(1+\mathcal{K})$ indicates the degradation of the bending properties of the composite due to the incomplete interaction between the external layers. Using the principle of virtual work one finds that the coefficient $\mathcal{K}$ is of the form

$$\mathcal{K} = \beta\, B_s \frac{\chi}{Gbtl^2}, \tag{1-3}$$

where, as explained in [Galuppi and Royer-Carfagni 2012], the shear coefficient of the intermediate layer χ is evaluated as $\chi = t^2/H^2$ and β is another parameter that depends upon the load condition. For simply supported beams, the corresponding values of β are recorded in [Wölfel 1987] for various loadings. Notice from (1-3) that $G \to \infty \Rightarrow \mathcal{K} \to 0$, so that from (1-2) also $B_s^* \to EI_{\text{tot}}$, i.e., the monolithic limit; moreover, $G \to 0 \Rightarrow \mathcal{K} \to \infty$ and $B_s^* \to E(I_1 + I_2)$, i.e., the layered limit.

Bennison [2009] and Calderone et al. [2009] have referred specifically to Wölfel's approach for the case of laminated glass. More precisely, they define the nondimensional coefficient $\Gamma = 1/(1+\mathcal{K})$, $\Gamma \in (0, 1)$, introduce the *equivalent moment of inertia* of the cross section in the form

$$I_{eq} = I_1 + I_2 + \Gamma \frac{A_1 A_2}{A_1 + A_2} H^2, \tag{1-4}$$

and consider for Γ the expression

$$\Gamma = \frac{1}{1+\beta \dfrac{\chi B_s}{Gbtl^2}} = \frac{1}{1+9.6\dfrac{tB_s}{GbH^2l^2}}. \tag{1-5}$$

This is equivalent to using in (1-3) the value $\beta = 9.6$, which corresponds to Wölfel's analysis for the particular case of a simply supported beam under uniformly distributed load. Consequently, recalling (1-4), for calculating the laminate deflection one can consider a monolithic beam with *deflection-effective thickness* $h_{\text{ef};w}$ given by

$$h_{\text{ef};w} = \sqrt[3]{h_1^3 + h_2^3 + 12\Gamma \frac{h_1 h_2}{h_1 + h_2} H^2}. \tag{1-6}$$

Once the deflection of the laminate is established, one can estimate the degree of connection offered by the deformable interlayer and, from this, the maximum stress in the glass can be easily estimated. The result [Bennison 2009; Calderone et al. 2009] is that the maximum bending stress in the i-th glass plies, $i = 1, 2$, is the same of that in a fictitious monolithic beam with analogous constraint and load conditions, with respectively *stress-effective thickness*

$$h_{1;\text{ef};\sigma} = \sqrt{\frac{h_{\text{ef};w}^3}{h_1 + 2\Gamma \dfrac{Hh_2}{h_1+h_2}}}, \quad h_{2;\text{ef};\sigma} = \sqrt{\frac{h_{\text{ef};w}^3}{h_2 + 2\Gamma \dfrac{Hh_1}{h_1+h_2}}}. \tag{1-7}$$

It is important to notice that this method relies upon the particular form of Γ given by (1-5), which assumes the coefficient $\beta = 9.6$, i.e., the one proposed by Wölfel for the very particular case of simply supported beams under uniformly distributed loading. Moreover, according to [Wölfel 1987], the validity of the method is limited because its simplifying assumptions are valid for statically determined composite beams, where the bending stiffness of the composite plies is considerably small. Nevertheless, this approach is widely used. In the design practice, the calculations for laminated glass panels are usually performed on an equivalent monolithic plate whose thickness is assumed to be given by (1-6), to determine maximum deflection, or by (1-7), where it is the bending stress to be calculated. This effective thickness is usually adopted in place of the actual thickness in analytic equations and simplified finite-element analysis; sometimes the method is abused in very delicate conditions, for example when calculating the stress concentrations around holes and contact regions in a neighborhood of the point-wise fixing of frameless glazing. In general, *no approach based upon the definition of the effective thickness can be used to evaluate local effects*. In any case, the Bennison–Wölfel method may lead to inaccurate results also when calculating maximum stress and deflection at the center of a laminated plate, especially when load and boundary conditions are different from that of a rectangular plate simply supported at two opposite side (cylindrical deformed shape) under uniformly distributed load.

In [Galuppi and Royer-Carfagni 2012] we treated the classical problem of a composite laminated glass beam under flexure using a variational approach similar in type to that proposed in [Aşik and Tezcan 2005] for numerical purposes. Using convenient shape functions for the beam deflection, simple formulas for the effective thickness were obtained which, for the one-dimensional case of beams with various constraint and load conditions, fitted with numerical experiments much better than the classical expressions (1-6) and (1-7). Our aim now is to extend this approach to the two-dimensional case of a rectangular laminated glass plate under uniform pressure, variously supported at the borders. For the cases considered in [Galuppi and Royer-Carfagni 2012] the problem is certainly much more complicated, but we show that by assuming again proper shape functions for the plate deflection, simple expressions of the effective thickness can be found. Comparisons with careful numerical experiments on full three-dimensional models, show the proposed formulation furnishes results more reliable than those obtainable with the classical Bennison–Wölfel approach. The method can be readily extended to plates of various shape, under diverse load conditions.

2. The variational problem

As indicated in Figure 2, with notation analogous to (1-1), consider a laminated plate composed of two glass layers of thickness h_1 and h_2 with Young's modulus E and Poisson's ratio ν, connected by a polymeric interlayer of thickness t and shear modulus G. Let

$$D_i = \frac{E h_i^3}{12(1-\nu^2)}$$

represent the flexural stiffness of the i-th glass plate, $i = 1, 2$, while H is the distance between their middle planes. Upon introduction of a reference system as indicated in Figure 2, the plate is identified by the $x - y$ domain Ω with border $\partial\Omega$, and is loaded by a pressure per unit area $p(x, y)$, not necessarily uniformly distributed.

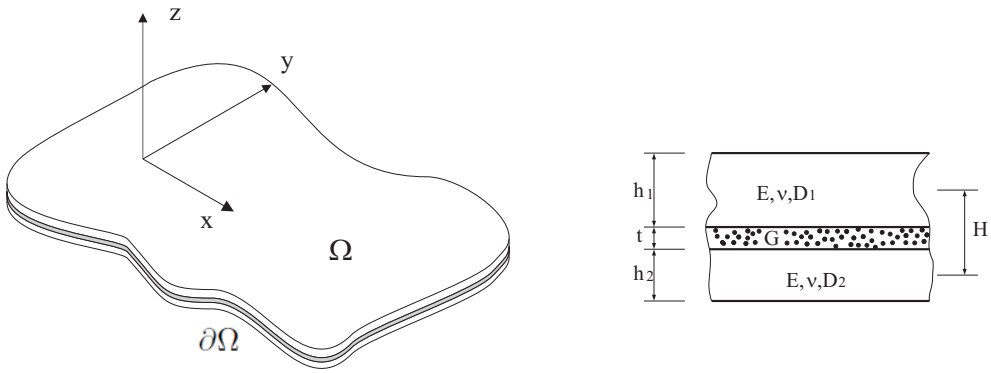

Figure 2. Plate composed of two glass plies bonded by a polymeric interlayer. Isometric and cross sectional view (not in the same scale).

No slippage is supposed to occur between glass and polymer (case of perfect bonding). Under the hypotheses that strains are small and rotations moderate, the kinematics is completely described by the out-of-plane displacement $w(x, y)$ in the z direction that, by neglecting the interlayer strain along z, is the same for the two glass layers, and the in-plane displacements of the i-th glass layers, $i = 1, 2$, for which the x and y components are denoted by $u_i(x, y)$ and $v_i(x, y)$, respectively (Figure 3).

2.1. ***The minimization problem.*** As represented Figure 3, let us denote with $u_{\text{sup}}(x, y)$ and $v_{\text{sup}}(x, y)$, $u_{\text{inf}}(x, y)$ and $v_{\text{inf}}(x, y)$, the x and y displacement components of those faces of the superior and inferior glass plies, respectively, in contact with the polymer. Then, the shear strain in the interlayer, constant through its thickness, is characterized by the components

$$\begin{aligned}\tilde{\gamma}_{zx} &= \frac{1}{t}[u_{\text{sup}}(x, y) - u_{\text{inf}}(x, y) + w_{,x}(x, y)t] = \frac{1}{t}[u_1(x, y) - u_2(x, y) + w_{,x}(x, y)H],\\ \tilde{\gamma}_{zy} &= \frac{1}{t}[v_{\text{sup}}(x, y) - v_{\text{inf}}(x, y) + w_{,y}(x, y)t] = \frac{1}{t}[v_1(x, y) - v_2(x, y) + w_{,y}(x, y)H],\end{aligned} \tag{2-1}$$

where subscript commas denote partial differentiation with respect to the indicated variable. The strain energy $\mathfrak{E}$ of the laminated glass plate is provided by the flexural and extensional contributions of the

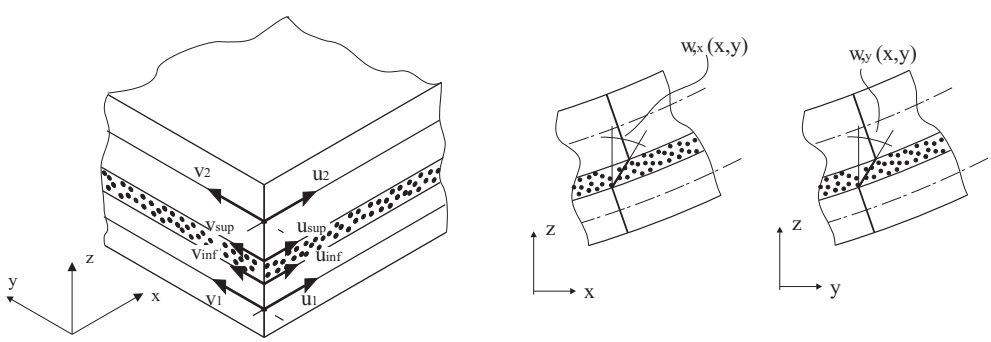

Figure 3. Relevant displacement components and corresponding deformation in the composite plate.

two glass layers, by the part corresponding to the shear deformation of the interlayer, and by the work associated with the external loads $p(x, y)$. We have, suppressing from the notation the dependence of w, u_i, v_i on x, y (see [Timoshenko and Woinowsky-Krieger 1971]):

$$\begin{aligned}\mathfrak{E}[w, u_1, u_2, v_1, v_2] = \int_\Omega \frac{1}{2}\Big\{&(D_1+D_2)[(w_{,xx}+w_{,yy})^2 - 2(1-\nu)(w_{,xx}w_{,yy} - w_{,xy}^2)]\\ &+12\frac{D_1}{h_1^2}\big[(u_{1,x}+v_{1,y})^2 - 2(1-\nu)\big(u_{1,x}v_{1,y} - \tfrac{1}{4}(u_{1,y}+v_{1,x})^2\big)\big]\\ &+12\frac{D_2}{h_2^2}\big[(u_{2,x}+v_{2,y})^2 - 2(1-\nu)\big(u_{2,x}v_{2,y} - \tfrac{1}{4}(u_{2,y}+v_{2,x})^2\big)\big]\\ &+\frac{G}{t}\big[(u_1-u_2+w_{,x}\,H)^2+(v_1-v_2+w_{,y}\,H)^2\big]+2p(x,y)w\Big\}\,dx\,dy. \qquad (2\text{-}2)\end{aligned}$$

The analysis of the first variation of the functional with respect to $w(x, y)$, $u_i(x, y)$ and $v_i(x, y)$, $i = 1, 2$, gives respectively the following Euler–Lagrange equations:

$$(D_1+D_2)\triangle\triangle w - \frac{GH}{t}[(u_1-u_2+w_{,x}\,H)_{,x}+(v_1-v_2+w_{,y}\,H)_{,y}] - p(x,y) = 0, \qquad (2\text{-}3)$$

$$\frac{12D_1}{h_1^2}\Big(u_{1,xx}+\frac{1-\nu}{2}u_{1,yy}+\frac{1+\nu}{2}v_{1,xy}\Big) - \frac{G}{t}(u_1-u_2+w_{,x}\,H) = 0, \qquad (2\text{-}4)$$

$$\frac{12D_2}{h_2^2}\Big(u_{2,xx}+\frac{1-\nu}{2}u_{2,yy}+\frac{1+\nu}{2}v_{2,xy}\Big) + \frac{G}{t}(u_1-u_2+w_{,x}\,H) = 0, \qquad (2\text{-}5)$$

$$\frac{12D_1}{h_1^2}\Big(v_{1,yy}+\frac{1-\nu}{2}v_{1,xx}+\frac{1+\nu}{2}u_{1,xy}\Big) - \frac{G}{t}(v_1-v_2+w_{,y}\,H) = 0, \qquad (2\text{-}6)$$

$$\frac{12D_2}{h_2^2}\Big(v_{2,yy}+\frac{1-\nu}{2}v_{2,xx}+\frac{1+\nu}{2}u_{2,xy}\Big) + \frac{G}{t}(v_1-v_2+w_{,y}\,H) = 0, \qquad (2\text{-}7)$$

with conditions at the boundary $\partial\Omega$

$$\begin{aligned}\oint_{\partial\Omega}\Big\{&(D_1+D_2)\frac{\partial}{\partial n}\triangle w - \frac{GH}{t}\big[(u_1-u_2+w_{,x}\,H),\,xn_x+(v_1-v_2+w_{,y}\,H),\,yn_y\big]\Big\}\,\delta w\,ds\\ &-\oint_{\partial\Omega}(D_1+D_2)\big[(w_{,xx}+\nu w_{,yy})n_x + w_{,xy}\,n_y\big]\,\delta w_{,x}\;ds\\ &-\oint_{\partial\Omega}(D_1+D_2)2(1-\nu)\big[w_{,xy}\,n_x+(w_{,xx}+\nu w_{,yy})n_y\big]\,\delta w_{,y}\;ds = 0, \qquad (2\text{-}8)\end{aligned}$$

$$\oint_{\delta\Omega}\Big[(u_{i,x}+\nu v_{i,y})n_x + \frac{1-\nu}{2}(u_{i,y}+v_{i,x})n_y\Big]\,\delta u_i\,ds = 0,\;\; i = 1..2, \qquad (2\text{-}9)$$

$$\oint_{\partial\Omega}\Big[\frac{1-\nu}{2}(u_{i,y}+v_{i,x})n_x + (v_{i,y}+\nu u_{i,x})n_y\Big]\,\delta v_i\,ds = 0,\;\; i = 1..2, \qquad (2\text{-}10)$$

where $\delta w(x, y)$, $\delta u_i(x, y)$ and $\delta v_i(x, y)$ are the variations of $w(x, y)$, $u_i(x, y)$ and $v_i(x, y)$, $i = 1, 2$, respectively. As customary in the calculus of variations [Sagan 1969], the geometric constraints at the border furnish restriction on the possible variations of the displacement components. Then, (2-8), (2-9) and (2-10) give the boundary conditions for the problem at hand.

2.2. ***Interpretation of the Euler–Lagrange Equation and boundary conditions.*** With standard notation from plate theory [Timoshenko and Woinowsky-Krieger 1971], the x- and y-components of the in-plane forces-per-unit-length in the i-th glass ply are of the form

$$N_{ix} = \frac{12D_i}{h_i^2}(u_{i,x} + \nu v_{i,y}), \quad N_{iy} = \frac{12D_i}{h_i^2}(v_{i,y} + \nu u_{i,x}), \quad N_{ixy} = \frac{12D_i}{h_1^2}\frac{1-\nu}{2}(u_{i,y} + v_{i,x}). \tag{2-11}$$

As shown in Figure 4, imagine cutting the interlayer of the laminated plate with a plane parallel to x and y at an arbitrary height t^*. The tangential stress component on the resulting surfaces are $\tilde{\tau}_{zx} = G\tilde{\gamma}_{zx}$ and $\tilde{\tau}_{zy} = G\tilde{\gamma}_{zy}$, where the shear strains $\tilde{\gamma}_{zx}$ and $\tilde{\gamma}_{zy}$ have been defined in (2-1). Since $\tilde{\gamma}_{zx}$ and $\tilde{\gamma}_{zy}$ do not depend on z, $\tilde{\tau}_{zx}$ and $\tilde{\tau}_{zy}$ are independent of t^*. It is then easily verified that (2-4), (2-5), (2-6) and (2-7) are the equilibrium equations in the x and y directions of the composing glass plies, that is,

$$\begin{aligned} &N_{1x,x} + N_{1xy,y} + \tilde{\tau}_{zx} = 0, \quad N_{2x,x} + N_{2xy,y} - \tilde{\tau}_{zx} = 0, \\ &N_{1y,y} + N_{1xy,x} + \tilde{\tau}_{zy} = 0, \quad N_{2y,y} + N_{2xy,x} - \tilde{\tau}_{zy} = 0. \end{aligned} \tag{2-12}$$

Moreover, from the moment-curvature relationships [Timoshenko and Woinowsky-Krieger 1971] for the i-th glass plate,

$$M_{ix} = -D_i(w_{,xx} + \nu w_{,yy}), \quad M_{iy} = -D_i(w_{,yy} + \nu w_{,xx}), \quad M_{ixy} = D_i(1-\nu)(w_{,xy}), \tag{2-13}$$

one finds that Equation (2-3) can be rewritten as

$$(M_{1x} + M_{2x})_{,xx} + (M_{1y} + M_{2y})_{,yy} - 2(M_{1xy} + M_{2xy})_{,xy} - (\tilde{\tau}_{zx,x} + \tilde{\tau}_{zy,y})H - p = 0. \tag{2-14}$$

Notice from Figure 4 that the shear stress at the surfaces resulting after the horizontal cut of the interlayer are statically equivalent, for each one of the component glass plies, to distributed torques per unit length. In particular, $\tilde{\tau}_{zx}$ generates $m_{1zx}(x, y) = -\tilde{\tau}_{zx}(\frac{1}{2}h_1 + t - t^*)$ and $m_{2zx}(x, y) = -\tilde{\tau}_{zx}(\frac{1}{2}h_2 + t^*)$ in the upper and lower glass plate, respectively. Then, the overall torque per unit length on the two glass plates is $m_{zx}(x, y) = m_{1zx}(x, y) + m_{2zx}(x, y) = -\tilde{\tau}_{zx}(\frac{1}{2}(h_1 + h_2) + t) = -G\tilde{\gamma}_{zx}H$. Similarly, $\tilde{\tau}_{zy}$

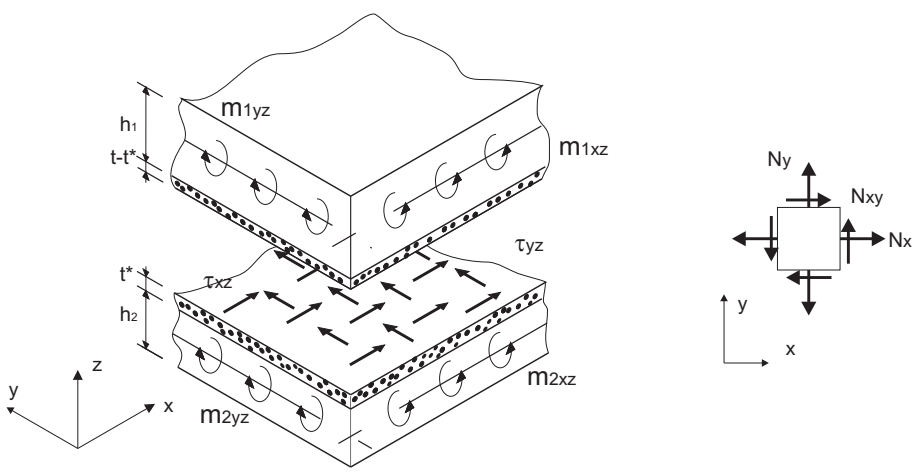

Figure 4. Equilibrium of portions of the laminated plate.

generates $m_{zy}(x, y) = -\tilde{\tau}_{zy}(\frac{1}{2}(h_1 + h_2) + t) = -G\tilde{\gamma}_{zy}H$. Henceforth, condition (2-3), or equivalently (2-14), represents the flexural equilibrium of the package glass + polymer under bending, in the form $(D_1 + D_2)\triangle\triangle w - p + m_{zx},_x + m_{zy},_y = 0$.

For what the border is concerned, (2-11) allows to write (2-9) and (2-10) in the form

$$\oint_{\partial\Omega} (N_{ix}n_x + N_{ixy}n_y)\delta u_i \, ds = 0, \quad \oint_{\partial\Omega} (N_{ixy}n_x + N_{iy}n_y)\delta v_i \, ds = 0 \quad (i = 1, 2), \tag{2-15}$$

these being the standard in-plane boundary conditions for the i-th glass layers [Timoshenko and Woinowsky-Krieger 1971]. Moreover, using (2-13) and defining $M_x = (M_{1x} + M_{2x})$, $M_y = (M_{1y} + M_{2y})$, $M_{xy} = (M_{1xy} + M_{2xy})$, condition (2-8) may be rearranged as

$$\oint_{\partial\Omega} [(M_x,_x - M_{xy},_y - H\tilde{\tau}_{zx},_x)n_x + (M_y,_y - M_{xy},_x - H\tilde{\tau}_{zy},_y)n_y]\,\delta w \, ds + \oint_{\partial\Omega} [M_x n_x + M_{xy}n_y]\,\delta w,_x \, ds + \oint_{\partial\Omega} [M_y n_y + M_{xy}n_x]\,\delta w,_y \, ds = 0. \tag{2-16}$$

This is readily interpretable because $Q_x = M_x,_x - M_{xy},_y$ and $Q_y = M_y,_y - M_{xy},_x$ represent the sum of the transversal shearing forces per unit length acting on the two glass plies. As in classical Kirchhoff plate theory [Timoshenko and Woinowsky-Krieger 1971], (2-16) gives the boundary condition in terms of bending couples and transversal shear.

2.3. ***Correlation between the displacements of the external layers.*** There are noteworthy identities, important for the forthcoming considerations, that correlate the displacements of the two constituent glass plies. In fact, we will prove that the (weighted) average displacement fields, defined as

$$U(x, y) = u_1(x, y) + \frac{h_2}{h_1} u_2(x, y), \quad V(x, y) = v_1(x, y) + \frac{h_2}{h_1} v_2(x, y), \tag{2-17}$$

are identically zero.

To illustrate, notice first that equations (2-4), (2-5), (2-6) and (2-7) may be rearranged in the form

$$\frac{12D_1}{h_1^2}\left(u_{1,xx} + \frac{1-\nu}{2}u_{1,yy} + \frac{1+\nu}{2}v_{1,xy}\right) = -\frac{12D_2}{h_2^2}\left(u_{2,xx} + \frac{1-\nu}{2}u_{2,yy} + \frac{1+\nu}{2}v_{2,xy}\right), \tag{2-18}$$

$$\frac{12D_1}{h_1^2}\left(v_{1,yy} + \frac{1-\nu}{2}v_{1,xx} + \frac{1+\nu}{2}u_{1,xy}\right) = -\frac{12D_2}{h_2^2}\left(v_{2,yy} + \frac{1-\nu}{2}v_{2,xx} + \frac{1+\nu}{2}u_{2,xy}\right). \tag{2-19}$$

In terms of $U(x, y)$ and $V(x, y)$, these can be rewritten as

$$\begin{aligned} U,_{xx} + \tfrac{1}{2}(1-\nu)U,_{yy} + \tfrac{1}{2}(1+\nu)V,_{xy} &= 0, \\ V,_{yy} + \tfrac{1}{2}(1-\nu)V,_{xx} + \tfrac{1}{2}(1+\nu)U,_{xy} &= 0, \end{aligned} \tag{2-20}$$

which is a system of partial differential equations defined on a connected domain Ω. If the glass plies are constrained so that $u_i = v_i = 0$, $i = 1..2$, on the boundary $\partial\Omega$, then from (2-17) also $U = V = 0$ on $\partial\Omega$. In general, however, the in-plane displacements of laminated glass are not constrained; in this case,

from (2-9) and (2-10) one finds the boundary conditions

$$\begin{aligned}(U_{,x}+\nu V_{,y})n_x+\tfrac{1}{2}(1-\nu)(U_{,y}+V_{,x})n_y=0 \quad &\text{on } \partial\Omega,\\ \tfrac{1}{2}(1-\nu)(U_{,y}+V_{,x})n_x+(V_{,y}+\nu V_{,x})n_y=0 \quad &\text{on } \partial\Omega.\end{aligned} \tag{2-21}$$

We can prove that the system of partial differential equations (2-20) with boundary condition $U=V=0$ on $\partial\Omega$ or, equivalently, with boundary condition given by (2-21), implies $U=V\equiv 0$ in Ω. Indeed, this is a standard argument in PDEs, because the system (2-20) can be proved to be strongly elliptic. Here, however, we use a more practical argument, by showing that this problem is equivalent to a classical boundary value problem in linear elasticity, for which well-known results hold. To this aim, we imagine that $U(x, y)$ and $V(x, y)$ represents the displacement field of a fictitious two-dimensional linear-elastic body Ω, with Young's modulus E and Poisson's ration ν, for which the (fictitious) stress components read

$$\hat{\sigma}_x=\frac{E}{1-\nu^2}(U_{,x}+\nu V_{,y}),\quad \hat{\sigma}_y=\frac{E}{1-\nu^2}(V_{,y}+\nu U_{,x}),\quad \hat{\sigma}_{xy}=\frac{E}{2(1+\nu)}(U_{,y}+V_{,x}). \tag{2-22}$$

It can then be shown that equations (2-20) with boundary conditions (2-21) can be rewritten as

$$\begin{cases}\hat{\sigma}_{x,x}+\hat{\sigma}_{xy,y}=0\\ \hat{\sigma}_{xy,x}+\hat{\sigma}_{y,y}=0\end{cases} \quad \text{in } \Omega, \tag{2-23}$$

$$\begin{cases}\hat{\sigma}_x n_x+\hat{\sigma}_{xy}n_y=0\\ \hat{\sigma}_{xy}n_x+\hat{\sigma}_y n_y=0\end{cases} \quad \text{on } \partial\Omega. \tag{2-24}$$

In the language of linear elasticity, these represent the equilibrium of a body in generalized plane stress with null boundary traction. Kirchhoff's theorem [Knops and Payne 1971] states that there is at most one solution to the Dirichlet boundary value problems in plane elasticity provided $-\infty<\nu<\frac{1}{2}$, $\nu\neq -1$, $E\neq 0$; in the traction boundary value problem there is uniqueness to within a rigid body displacement. In the considered case of null body forces and null boundary traction, since $E>0$ and $-1<\nu<\frac{1}{2}$, the solution is unique and it consist in a null stress field, leading to a displacement field of the form

$$\begin{pmatrix}U(x,y)\\ V(x,y)\end{pmatrix}=\begin{pmatrix}-\omega y\\ \omega x\end{pmatrix}+\begin{pmatrix}c_1\\ c_2\end{pmatrix}, \tag{2-25}$$

with constants c_1, c_2 and ω, that represents an infinitesimal rigid body displacement. It is easy to show that such constants are null for the case at hand if the laminated glass package is properly constraint in order to prevent its rigid displacements. In conclusion, one finds $U(x, y)\equiv 0$ and $V(x, y)\equiv 0$, for which the expected identities

$$u_2(x,y)=-\frac{h_1}{h_2}\,u_1(x,y),\quad v_2(x,y)=-\frac{h_1}{h_2}\,v_1(x,y). \tag{2-26}$$

This is because the in-plane forces in the two glass plies, which are due to the mutual shear forces transmitted by the interlayer, must balance one another.

2.4. ***Layered and monolithic limits.*** When the shear modulus of the interlayer vanishes, i.e., $G \to 0$, conditions (2-3), (2-4), (2-5), (2-6) and (2-7) take the form ($i = 1, 2$)

$$\begin{cases} (D_1 + D_2)\triangle\triangle w - p(x, y) = 0, \\ \dfrac{12D_i}{h_i^2}\left(u_{i,xx} + \dfrac{1-\nu}{2}u_{i,yy} + \dfrac{1+\nu}{2}v_{i,xy}\right) = 0, \\ \dfrac{12D_i}{h_i^2}\left(v_{i,yy} + \dfrac{1-\nu}{2}v_{i,xx} + \dfrac{1+\nu}{2}u_{i,xy}\right) = 0. \end{cases} \tag{2-27}$$

The first equation clearly corresponds to the flexural equilibrium of two frictionless sliding glass plates, with flexural bending $D_1 + D_2$, subject to a distributed load $p(x, y)$, while the others are the equilibrium conditions for the in-plane forces in x and y direction of the upper and lower glass plies, respectively. This is the *layered limit*, i.e., the laminated glass plate behaves as two free-sliding glass plies.

When $G \to +\infty$, then the shear strain in the interlayer tends to zero, i.e., $\tilde{\gamma}_{zx} = 0$, $\tilde{\gamma}_{zy} = 0$ in (2-1). Using the relationships (2-26), such conditions give:

$$\begin{aligned} \tilde{\gamma}_{zx} = [u_1 - u_2 + w_{,x}\, H]/t = 0 \quad &\Rightarrow \quad u_1 = -\frac{D_2 h_1^2}{D_1 h_2^2 + D_2 h_1^2} H\, w_{,x} = -\frac{h_2}{h_1 + h_2} H\, w_{,x}\,, \\ \tilde{\gamma}_{zy} = [v_1 - v_2 + w_{,y}\, H]/t = 0 \quad &\Rightarrow \quad v_1 = -\frac{D_2 h_1^2}{D_1 h_2^2 + D_2 h_1^2} H\, w_{,y} = -\frac{h_2}{h_1 + h_2} H\, w_{,y}\,. \end{aligned} \tag{2-28}$$

Substituting in the Euler–Lagrange equations, one finds

$$\begin{cases} D_{\text{tot}}\triangle\triangle w - p(x, y) = 0, \\ \dfrac{12D_1}{h_1^2}\left(u_{1,xx} + \dfrac{1-\nu}{2}u_{1,yy} + \dfrac{1+\nu}{2}v_{1,xy}\right) = -\dfrac{12D_2}{h_2^2}\left(u_{2,xx} + \dfrac{1-\nu}{2}u_{2,yy} + \dfrac{1+\nu}{2}v_{2,xy}\right), \\ \dfrac{12D_1}{h_1^2}\left(v_{1,yy} + \dfrac{1-\nu}{2}v_{1,xx} + \dfrac{1+\nu}{2}u_{1,xy}\right) = -\dfrac{12D_2}{h_2^2}\left(v_{2,yy} + \dfrac{1-\nu}{2}v_{2,xx} + \dfrac{1+\nu}{2}u_{2,xy}\right), \\ G\tilde{\gamma}_{zx} = \dfrac{12D_1}{h_1^2}\left(u_{1,xx} + \dfrac{1-\nu}{2}u_{1,yy} + \dfrac{1+\nu}{2}v_{1,xy}\right), \\ G\tilde{\gamma}_{zy} = \dfrac{12D_1}{h_1^2}\left(v_{1,yy} + \dfrac{1-\nu}{2}v_{1,xx} + \dfrac{1+\nu}{2}u_{1,xy}\right), \end{cases} \tag{2-29}$$

where the quantity D_{tot}, defined as

$$D_{\text{tot}} = D_1 + D_2 + \frac{12D_1 D_2}{D_1 h_2^2 + D_2 h_1^2} H^2 = D_1 + D_2 + \frac{E}{1-\nu^2}\frac{h_1 h_2}{h_1 + h_2} H^2, \tag{2-30}$$

represents the flexural stiffness of a monolithic plate, whose flexural inertia is that of the two glass plies properly spaced of the gap given by the thickness of the interlayer. This is indeed the *monolithic limit* of laminated glass [Bennison et al. 1999].

3. The enhanced effective thickness approach

It is not possible to solve the system of differential equations (2-3), (2-4), (2-5), (2-6) and (2-7) in closed form, but an approximation can be found by choosing an appropriate class of shape functions for the unknown fields $w(x, y)$, $u_1(x, y)$, $u_2(x, y)$, $v_1(x, y)$ and $v_2(x, y)$ defined up to parameters that will be

determined from energy minimization. The shape functions must be compatible with the qualitative properties of the exact solution and, in particular, must comprehend the monolithic-limit solution, when $G \to \infty$, and the layered-limit solution, when $G \to 0$. In terms of the field $w(x, y)$, such borderline cases correspond, respectively, to the fields $w_M(x, y)$ and $w_L(x, y)$ that, being the solutions of the differential equations

$$D_{\text{tot}} \triangle\triangle w_M(x, y) - p(x, y) = 0, \quad (D_1 + D_2) \triangle\triangle w_L(x, y) - p(x, y) = 0, \tag{3-1}$$

are of the form

$$w_M(x, y) \equiv \frac{g(x, y)}{D_{\text{tot}}}, \quad w_L(x, y) \equiv \frac{g(x, y)}{D_1 + D_2}, \tag{3-2}$$

where $g(x, y)$ is a function that depends upon the boundary conditions of the problem at hand. Henceforth, we may define the equivalent (reduced) flexural rigidity of the laminate plate

$$\frac{1}{D_R} = \frac{\eta}{D_{\text{tot}}} + \frac{1 - \eta}{D_1 + D_2}, \tag{3-3}$$

being the parameter η a nondimensional quantity, tuning the plate response from the layered limit ($\eta = 0$) to the monolithic limit ($\eta = 1$). An approximating class of solutions can thus be sought in the form

$$w(x, y) = \frac{g(x, y)}{D_R}, \tag{3-4}$$

where $g(x, y)$ is the shape function for the vertical displacement, uniquely determined by the shape of the laminated glass plate in $x - y$ plane, by the external load $p(x, y)$ and by the geometric boundary conditions.

The shape functions for the in-plane displacements should also guarantee that $\tilde{\gamma}_{zx} = 0$, $\tilde{\gamma}_{zy} = 0$ in the borderline monolithic case. Recalling (2-18) and (2-19), we select the form

$$\begin{aligned} u_1(x, y) &= -\beta \frac{1}{D_{\text{tot}}} \frac{h_2}{h_1 + h_2} H g_{,x}(x, y), \quad u_2(x, y) = \beta \frac{1}{D_{\text{tot}}} \frac{h_1}{h_1 + h_2} H g_{,x}(x, y), \\ v_1(x, y) &= -\beta \frac{1}{D_{\text{tot}}} \frac{h_2}{h_1 + h_2} H g_{,y}(x, y), \quad v_2(x, y) = \beta \frac{1}{D_{\text{tot}}} \frac{h_1}{h_1 + h_2} H g_{,y}(x, y), \end{aligned} \tag{3-5}$$

where β is another nondimensional parameter, again tuning the response from the layered limit ($\beta = 0$, implying null in-plane force in the glass layers) to the monolithic limit ($\beta = 1$, leading to $\tilde{\gamma}_{zx} = \tilde{\gamma}_{zy} = 0$).

The corresponding total strain energy (2-2) can thus be rewritten as a function of the parameters η and β to give

$$\begin{aligned} &\mathfrak{E}[w, u_1, u_2, v_1, v_2] = \widetilde{\mathfrak{E}}[\eta, \beta] = \\ &\frac{1}{2} \int_\Omega \left\{ \left(\frac{D_1 + D_2}{D_R^2} + \beta^2 \frac{12 D_1 D_2 H^2}{D_1 h_2^2 + D_2 h_1^2} \frac{1}{D_{\text{tot}}} \right) \left[(g_{,xx} + g_{,yy})^2 - 2(1 - \nu)(g_{,xx}\, g_{,yy} - g_{,xy}^2) \right] \right. \\ &\qquad \left. + \frac{G H^2}{t} \left(\frac{1}{D_R} - \frac{\beta}{D_{\text{tot}}} \right) [g_{,x}^2 + g_{,y}^2] + 2 \frac{p(x, y)}{D_R} g \right\} dx\, dy. \end{aligned} \tag{3-6}$$

This expression can be simplified by observing from (3-1) and (3-2) that $w(x, y) = g(x, y)/D_R$ of (3-4) is the exact solution of the elastic bending of a plate with constant flexural rigidity D_R under the load $p(x, y)$, with the same domain Ω and the geometric boundary condition of the problem at hand.

Consider the virtual work equality for this elastic body, in which the aforementioned $w(x, y)$ is selected as the strain/displacement field, whereas the stress/force field in equilibrium with $p(x, y)$ is given by

$$\begin{cases} M_x = -D_R(w_{,xx} + \nu w_{,yy}) = -(g_{,xx} + \nu g_{,yy}), \\ M_y = -D_R(w_{,yy} + \nu w_{,xx}) = -(g_{,yy} + \nu g_{,xx}), \\ M_{xy} = D_R(1-\nu) w_{,xy} = (1-\nu) g_{,xy}\,. \end{cases} \tag{3-7}$$

The external and internal virtual works, L_{ve} and L_{vi}, can be written as

$$\begin{aligned} L_{ve} &= -\frac{1}{D_R}\int_\Omega p(x, y)\, g\, dx\, dy, \\ L_{vi} &= \int_\Omega [M_x w_{,x} + M_y w_{,y} + M_{xy}\gamma_{xy}]\, dx\, dy \\ &= -\frac{1}{D_R}\int_\Omega \left[(g_{,xx} + g_{,yy})^2 - 2(1-\nu)(g_{,xx}\, g_{,yy} - g_{,xy}^2)\right] dx\, dy. \end{aligned} \tag{3-8}$$

Equality of external and internal virtual work then gives

$$\int_\Omega p(x, y) g\, dx\, dy = \int_\Omega \left[(g_{,xx} + g_{,yy})^2 - 2(1-\nu)(g_{,xx}\, g_{,yy} - g_{,xy}^2)\right] dx\, dy. \tag{3-9}$$

This condition allows a drastic simplification of the energy (3-6). In fact, substituting (3-9) into (3-6), the following expression for the strain energy can be found:

$$\begin{aligned} &\mathfrak{E}[w, u_1, u_2, v_1, v_2] = \widetilde{\mathfrak{E}}[\eta, \beta] = \\ &\frac{1}{2}\int_\Omega \left\{ \left(\frac{D_1 + D_2}{D_R^2} + \beta^2 \frac{12 D_1 D_2 H^2}{D_1 h_2^2 + D_2 h_1^2} \frac{1}{D_{\text{tot}}} \right) p(x, y)\, g \right. \\ &\qquad \left. + \frac{G H^2}{t}\left(\frac{1}{D_R} - \frac{\beta}{D_{\text{tot}}} \right)[g_{,x}^2 + g_{,y}^2] + \frac{p(x, y)\, g}{D_R} \right\} dx\, dy. \end{aligned} \tag{3-10}$$

Since $g(x, y)$ is supposed to have been determined from (3-1), the integral in (3-10) depends upon the free parameters η and β only, whose optimal value, say η^* and β^*, is obtained by direct minimization. The final result is that

$$\eta^* = \beta^* = \frac{1}{1 + \dfrac{D_1 + D_2}{(G/t) D_{\text{tot}}} \dfrac{12 D_1 D_2}{D_1 h_2^1 + D_2 h_1^2} \Psi}, \tag{3-11}$$

where the coefficient

$$\Psi = \frac{\int_\Omega p(x, y)\, g\, dx\, dy}{\int_\Omega [g_{,x}^2 + g_{,y}^2]\, dx\, dy} \tag{3-12}$$

depends upon the geometry of the plate and on its boundary and loading condition.

Deflection-effective thickness. The coefficient η, appearing in the definition of D_R (3-3), is in some sense analogous to the parameter Γ of (1-5) in the Bennison–Wölfel model [Wölfel 1987; Bennison 2009; Calderone et al. 2009], because the layered limit corresponds to $\Gamma = \eta = 0$ and the monolithic limit to $\Gamma = \eta = 1$. From (3-3), the *deflection-effective thickness* $\hat{h}_{\text{ef};w}$, associated with the value η^*, can be written in the form

$$\hat{h}_w = \left(\frac{\eta^*}{h_1^3 + h_2^3 + 12 \dfrac{h_1 h_2}{h_1 + h_2} H^2} + \frac{1 - \eta^*}{h_1^3 + h_2^3} \right)^{-1/3}. \tag{3-13}$$

Stress-effective thickness. The stress-effective thickness may be defined as the (constant) thickness $\hat{h}_{i;\mathrm{ef};\sigma}$ of a monolithic plate for which the maximum bending stress is equal to the maximum stresses in the i-th glass layer of the laminated plate. The stresses in a monolithic plate are associated with the moments per-unit-length M_x, M_y, M_{xy}, defined by (3-7). On the other hand, the i-th glass ply of the laminated plate is subjected to moments and in-plane forces per unit length given by (2-13) and (2-11), respectively. Then, $\hat{h}_{i;\mathrm{ef};\sigma}$ can be found by equating the two contributions, i.e.,

$$\begin{aligned}
|\sigma_{xx}|_{\max} &= \max \left| \frac{N_{ix}(x, y)}{h_i} \pm \frac{6 M_{ix}(x, y)}{h_i^2} \right| = \frac{\max |M_x(x, y)|}{\frac{1}{6} \hat{h}_{i;\mathrm{ef};\sigma}^2}, \\
|\sigma_{yy}|_{\max} &= \max \left| \frac{N_{iy}(x, y)}{h_i} \pm \frac{6 M_{iy}(x, y)}{h_i^2} \right| = \frac{\max |M_y(x, y)|}{\frac{1}{6} \hat{h}_{i;\mathrm{ef};\sigma}^2}, \\
|\sigma_{xy}|_{\max} &= \max \left| \frac{N_{ixy}(x, y)}{h_i} \pm \frac{6 M_{ixy}(x, y)}{h_i^2} \right| = \frac{\max |M_{xy}(x, y)|}{\frac{1}{6} \hat{h}_{i;\mathrm{ef};\sigma}^2}.
\end{aligned} \tag{3-14}$$

Recalling (3-4) and (3-5), the moments and in-plane forces per unit length can be rewritten as a function of the shape function $g(x, y)$ in the form

$$\begin{aligned}
M_{ix} &= -\frac{D_i}{D_R}(g_{,xx} + \nu g_{,yy}), \quad N_{ix} = -(-1)^i \eta^* \frac{12 D_1 D_2}{D_2 h_1^2 + D_1 h_2^2} \frac{H}{D_{\mathrm{tot}}} (g_{,xx} + \nu g_{,yy}), \\
M_{iy} &= -\frac{D_i}{D_R}(g_{,yy} + \nu g_{,xx}), \quad N_{iy} = -(-1)^i \eta^* \frac{12 D_1 D_2}{D_2 h_1^2 + D_1 h_2^2} \frac{H}{D_{\mathrm{tot}}} (g_{,yy} + \nu g_{,xx}), \\
M_{ixy} &= (1 - \nu) \frac{D_i}{D_R} g_{,xy}, \qquad N_{ixy} = -(-1)^i \eta^* (1 - \nu) \frac{12 D_1 D_2}{D_2 h_1^2 + D_1 h_2^2} \frac{H}{D_{\mathrm{tot}}} g_{,xy}.
\end{aligned} \tag{3-15}$$

After defining, as in [Bennison 2009],

$$h_{s;1} = \frac{h_1 H}{h_1 + h_2}, \quad h_{s;2} = \frac{h_2 H}{h_1 + h_2}, \tag{3-16}$$

one finds from (3-14) expressions analogous to that defined in (1-7) in the form

$$\frac{1}{\hat{h}_{1;\sigma}^2} = \frac{2 \eta^* h_{s;2}}{h_1^3 + h_2^3 + 12 \dfrac{h_1 h_2}{h_1 + h_2} H} + \frac{h_1}{\hat{h}_w^3}, \quad \frac{1}{\hat{h}_{2;\sigma}^2} = \frac{2 \eta^* h_{s;1}}{h_1^3 + h_2^3 + 12 \dfrac{h_1 h_2}{h_1 + h_2} H} + \frac{h_2}{\hat{h}_w^3}. \tag{3-17}$$

Notice that the expressions for the effective thickness (3-13) and (3-17) are of the same type obtained in [Galuppi and Royer-Carfagni 2012] for the one dimensional case.

In the following, the method based upon formulas (3-13) and (3-17) will be referred to as the enhanced effective thickness (EET) approach.

4. Examples

The four paradigmatic cases of rectangular laminated plates $\{0 \le x \le a;\ 0 \le y \le b\}$ with various boundary conditions, as shown in Figure 5, are now examined. We set $b = 2000\,\text{mm}$, while for a the three values $a = 2000\,\text{mm}$, $a = 3000\,\text{mm}$ and $a = 6000\,\text{mm}$ are considered. Parameters for glass plates are $E = 70\,\text{GPa}$, $\nu = 0.22$, $h_1 = h_2 = 10\,\text{mm}$, the thickness of the interlayer is $t = 0.76\,\text{mm}$ while its shear modulus G is continuously varied from 0.01 MPa to 10 MPa, in order to evaluate its influence on the shear-coupling of the glass plies. All the laminates are subjected to a uniformly distributed pressure $p = 0.75\,\text{kN/m}^2$, but since all materials are linear elastic, stress and strain depend linearly upon p. The results obtained with the approximate methods will in each case be compared with an accurate numerical analysis performed with ABAQUS, using a 3-D mesh with 110000 solid 20-node quadratic bricks with reduced integration, available in the ABAQUS program library.

The shape function $g(x, y)$ of (3-4) is assumed according to the form (uniform distribution) of the external load $p(x, y)$ and the geometric boundary conditions. The coefficient η^*, which allows to calculate the stress and deflection-effective thickness, as per (3-13) and (3-17), is calculated by using (3-11), evaluating the parameter Ψ through (3-12). But since for the case at hand $h_1 = h_2 = h$, as customary in the design practice, the expression for η^* can be simplified:

$$\eta^* = \frac{1}{1 + \dfrac{t}{G}\dfrac{E}{1-\nu^2}\dfrac{h^3}{2(h^2+3H^2)}\Psi}. \tag{4-1}$$

To facilitate the analysis of rectangular plates of any size, the values of Ψ are recorded in tables as a function of the length a and of the aspect ratio $\lambda = b/a$.

4.1. ***Simply supported rectangular plates.*** Consider a rectangular laminated glass under a uniformly distributed load p with four simply supported edges (Figure 5a). The classical Navier solution [Timoshenko and Woinowsky-Krieger 1971] gives the elastic deflection of a monolithic plate with flexural

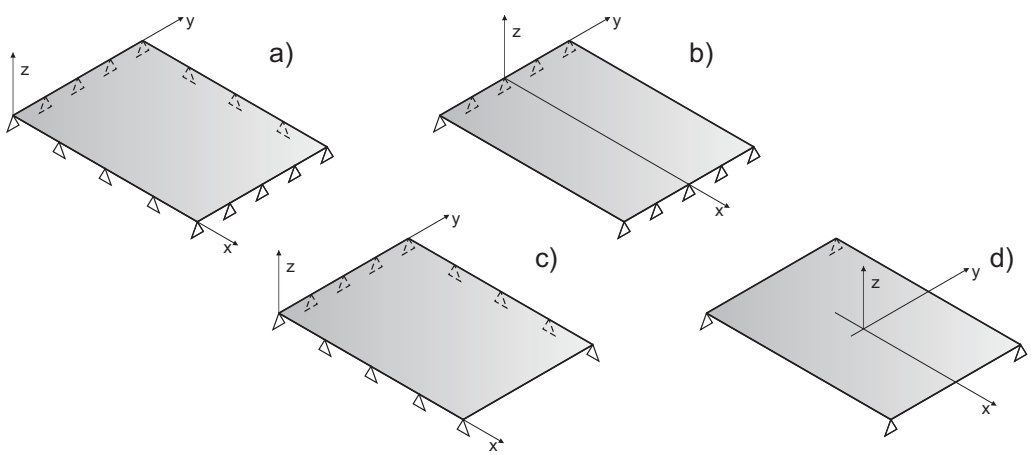

Figure 5. Representative examples of laminated glass plates under various boundary and load conditions.

a[mm] \ λ	0.1	0.2	0.3	0.4	0.5	0.6	0.7	0.8	0.9	1
500	39.8732	10.2644	4.7813	2.8622	1.9739	1.4914	1.2005	1.0116	0.8822	0.7896
1000	9.9683	2.5661	1.1953	0.7155	0.4935	0.3729	0.3001	0.2529	0.2205	0.1974
1500	4.4304	1.1405	0.5313	0.3180	0.2193	0.1657	0.1334	0.1124	0.0980	0.0877
2000	2.4921	0.6415	0.2988	0.1789	0.1234	0.0932	0.0750	0.0632	0.0551	0.0493
2500	1.5949	0.4106	0.1913	0.1145	0.0790	0.0597	0.0480	0.0405	0.0353	0.0316
3000	1.1076	0.2851	0.1328	0.0795	0.0548	0.0414	0.0333	0.0281	0.0245	0.0219

Table 1. Coefficient Ψ (in $\mathrm{mm}^{-2} \times 10^4$) for rectangular plates with four edges simply supported.

rigidity D_R in the form

$$w(x, y) = \frac{16p}{\pi^6 D_R} \sum_{m=1}^{\infty} \sum_{n=1}^{\infty} \frac{\sin \dfrac{m\pi x}{a} \sin \dfrac{n\pi y}{b}}{nm\left(\dfrac{m^2}{a^2} + \dfrac{n^2}{b^2}\right)^2}. \tag{4-2}$$

Partial sums of a finite number of terms of the series can be used as approximations of the entire function. By taking just the first term in the series (first-order approximation), the shape function $g(x, y)$ of (3-4) is

$$g(x, y) = \frac{16p}{\pi^6} \frac{1}{\left(\dfrac{1}{a^2} + \dfrac{1}{b^2}\right)^2} \sin \frac{\pi x}{a} \sin \frac{\pi y}{b}, \tag{4-3}$$

and the corresponding graph is drawn in Figure 6.

From this, the coefficient η^*, evaluated through (3-11) or (4-1), reads

$$\eta^* = \frac{1}{1 + \dfrac{D_1 + D_2}{(G/t) D_{\mathrm{tot}}} \dfrac{12 D_1 D_2}{D_1 h_2^1 + D_2 h_1^2} \dfrac{\pi^2 (a^2 + b^2)}{a^2 b^2}}. \tag{4-4}$$

It has been directly verified that higher-order approximations, obtained by considering more terms of the series (4-2), do not substantially increase the level of accuracy. The coefficient $\Psi[\mathrm{mm}^{-2}]$ that appears in (3-11) and (4-1) is tabulated in Table 1 as a function of the length a [mm] and of the aspect ratio $\lambda = b/a$.

For the case $a = 3000$ mm, $b = 2000$ mm and for a shear modulus of the polymeric interlayer G varying from 0, 01 MPa to 10 MPa, the graphs in Figure 7 compare the deflection- and stress-effective thickness

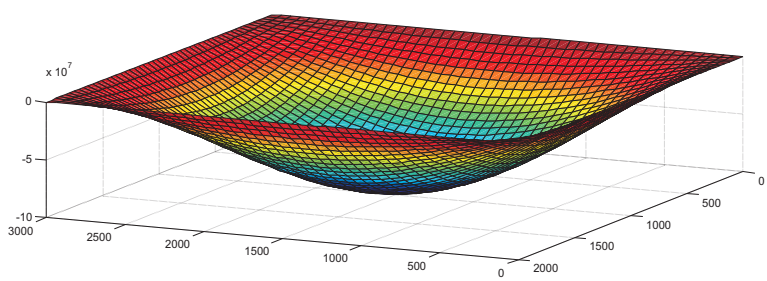

Figure 6. Shape function for simply supported rectangular laminated plates. Case $a = 3000$ mm, $b = 2000$ mm.

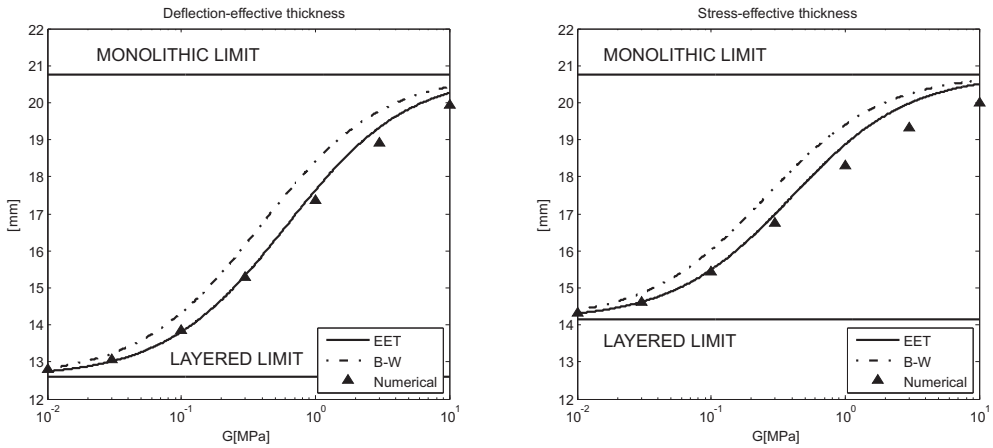

Figure 7. Simply supported rectangular plate, case $a = 3000\,\text{mm}$, $b = 2000\,\text{mm}$. Comparison of the effective thicknesses obtained with the Bennison–Wölfel approach (B-W), the enhanced effective thickness approach (ETT), and numerical simulations.

calculated according to the proposed approach of Section 3, here referred to as EET (enhanced effective thickness), with the effective thicknesses calculated through (1-6) and (1-7) for the Bennison–Wölfel model, recalled in the Introduction.

It is evident here that the proposed enhanced effective-thickness (ETT) approach and the Bennison–Wölfel (B-W) formulation give qualitatively different results. However, B-W is on the side of safeness, because it predicts deflection and stress values higher than those predicted by the EET approach. The numerical simulations show that the EET approach provides a better approximation than B-W, but the difference is not substantial, at least for the case at hand. The analytical approach recently proposed in [Foraboschi 2012] for the particular case at hand gives results in good agreement with the EET results.

The case of Figure 8 corresponds to $a = 6000\,\text{mm}$ and $b = 2000\,\text{mm}$, that is, the plate is a long rectangle whose deformation tends to be cylindrical in a neighborhood of the center. In such a case, the behavior predicted by the EET approach is close to Bennison–Wölfel's. This is not surprising because the aspect ratio is such that plate response is similar to the response of a beam ($\lambda = b/a \gg 1$), and Bennison–Wölfel's model is calibrated on the case of simply supported beams under uniformly distributed load [Galuppi and Royer-Carfagni 2012]. Numerical simulations confirm the accuracy.

On the contrary, the greatest differences between the EET and B-W approaches are obtained when the plate is square, i.e., when the deflections of beam and plate differ the most. This case is illustrated in Figure 9 for a plate with $a = 2000\,\text{mm}$ and $b = 2000\,\text{mm}$. It is evident, here, that the results achieved through the ETT approach are closer to the numerical data.

4.2. ***Rectangular plates with two opposite simply supported sides.*** For the case of rectangular plates with two opposite simply supported sides (Figure 5b), following [Timoshenko and Woinowsky-Krieger 1971] and reasoning as in the previous case, the shape function $g(x, y)$ may be chosen in the form

$$g(x, y) = pa^4 \sum_{m=1,3,5,\ldots}^{\infty} \left[\frac{4}{\pi^5 m^5} + A_m \cosh \frac{m\pi y}{a} + B_m \frac{m\pi y}{a} \sinh \frac{m\pi y}{a} \right] \sin \frac{m\pi x}{a}, \tag{4-5}$$

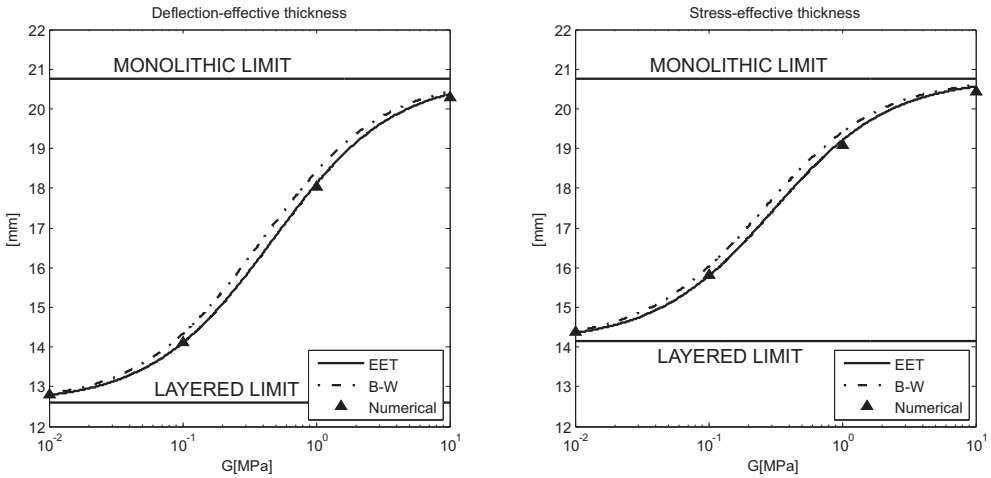

Figure 8. Simply supported rectangular plate, case $a = 6000\,\text{mm}$, $b = 2000\,\text{mm}$ (see Figure 7 for legend).

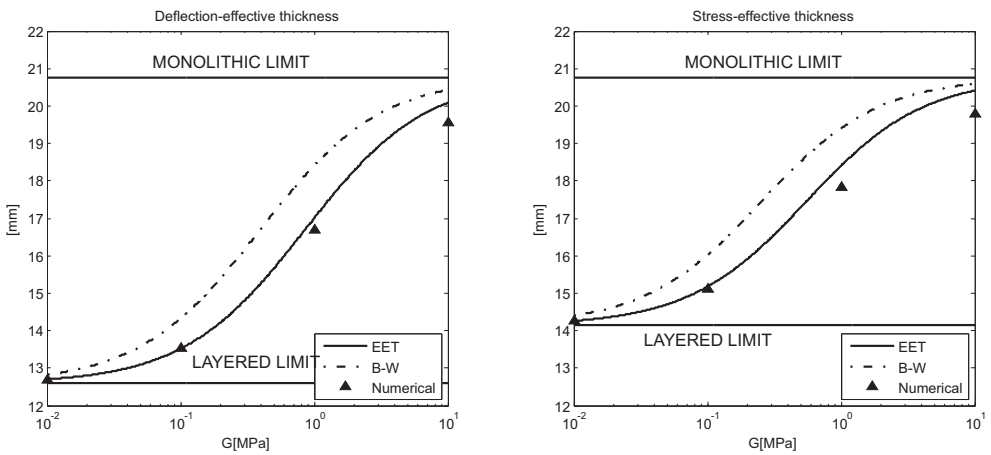

Figure 9. Simply supported square plate, case $a = 2000\,\text{mm}$, $b = 2000\,\text{mm}$ (see Figure 7 for legend).

where

$$A_m = \frac{4}{\pi^5 m^5} \frac{\nu(1+\nu)\sinh\frac{m\pi b}{2a} - \nu(1-\nu)\frac{m\pi b}{2a}\cosh\frac{m\pi b}{2a}}{(3+\nu)(1-\nu)\sinh\frac{m\pi b}{2a}\cosh\frac{m\pi b}{2a} - (1-\nu)^2\frac{m\pi b}{2a}},$$
$$B_m = \frac{4}{\pi^5 m^5} \frac{\nu(1-\nu)\sinh\frac{m\pi b}{2a}}{(3+\nu)(1-\nu)\sinh\frac{m\pi b}{2a}\cosh\frac{m\pi b}{2a} - (1-\nu)^2\frac{m\pi b}{2a}}. \tag{4-6}$$

We take a first-order approximation just keeping the first term of the series, whose graph is plotted in Figure 10.

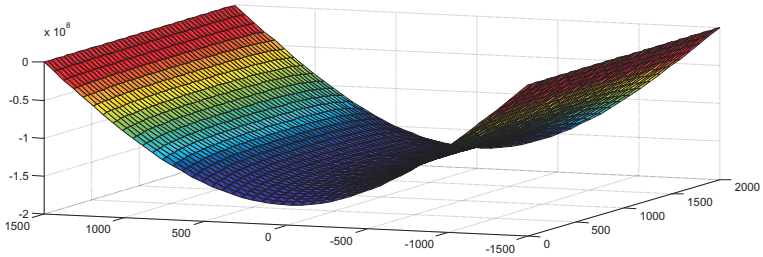

Figure 10. Shape function for rectangular plate with two opposite edges simply supported. Case $a = 3000\,\text{mm}$, $b = 2000\,\text{mm}$.

The coefficient η^* is given by (4-1), where Ψ, when evaluated by taking the first term only in the series, is of the form

$$\Psi = \frac{8\pi^2\big(4b + B_1\pi^5 bC + 2aS\pi^4(A_1 - B_1)\big)}{a\big(B_1^2\pi^{11}b^2SC + 32ab + abB_1(-B_1 + 4A_1S^2)\pi^{10} + 2a^2SC(2A_1^2 + B_1^2)\pi^9 + 16B_1\pi^5 abC + 32a^2S\pi^4(A_1 - B_1)\big)}, \tag{4-7}$$

with $C = \cosh\dfrac{m\pi b}{2a}$ and $S = \sinh\dfrac{m\pi b}{2a}$. The value of Ψ is reported in Table 2 as a function of a and $\lambda = b/a$.

Figure 11 shows the comparison between the deflection- and stress-effective thicknesses, calculated according to the enhanced effective thickness approach and to Bennison–Wölfel model as a function of G.

In this case the EET and B-W approaches give results that in practice coincide. A plate under these particular boundary conditions presents in fact a cylindrical deformed shape very similar to that of a beam with equivalent cross-sectional inertia. The good approximation that can be achieved is evidenced by the comparison with the numerical results.

4.3. ***Rectangular plates with three simply supported sides.*** For the case of rectangular plates with three simply supported sides under uniform pressure (Figure 5c), Timoshenko and Woinowsky-Krieger [1971] furnishes the general form for the elastic deflection of a monolith. Then, the shape function can be

a[mm] \ λ	0.2	0.4	0.6	0.8	1	1.25	1.667	2.5	5
500	0.4233	0.3908	0.3816	0.3770	0.3742	0.3718	0.3690	0.3653	0.3579
1000	0.1058	0.0977	0.0954	0.0943	0.0935	0.0929	0.0922	0.0913	0.0895
1500	0.0470	0.0434	0.0424	0.0419	0.0416	0.0413	0.0410	0.0406	0.0398
2000	0.0265	0.0244	0.0238	0.0236	0.0234	0.0232	0.0231	0.0228	0.0224
2500	0.0169	0.0156	0.0153	0.0151	0.0150	0.0149	0.0148	0.0146	0.0143
3000	0.0118	0.0109	0.0106	0.0105	0.0104	0.0103	0.0102	0.0101	0.0099

Table 2. Coefficient Ψ (in $\text{mm}^{-2} \times 10^4$) for rectangular plates with two opposite edges simply supported.

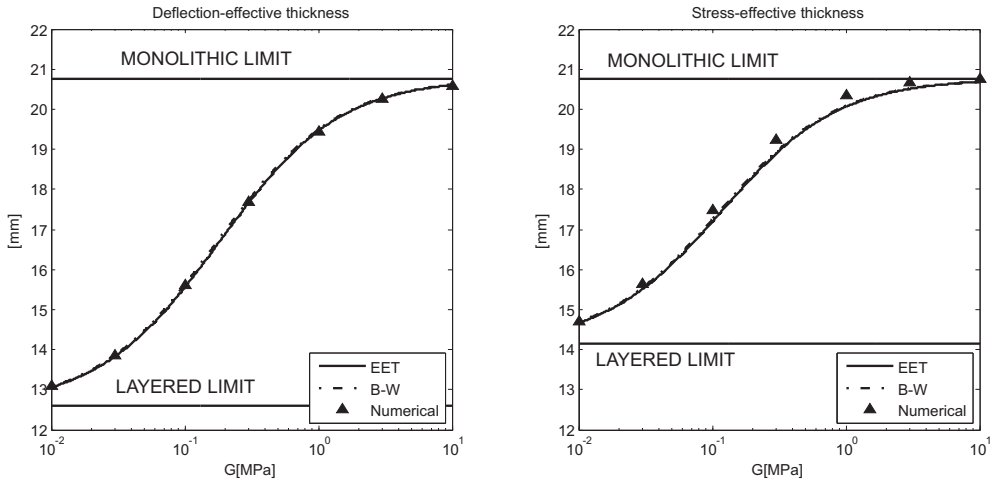

Figure 11. Rectangular plates with two opposite edges simply supported, case $a = 3000\,\text{mm}$, $b = 2000\,\text{mm}$. Comparison of the effective thicknesses obtained with: Bennison–Wölfel approach (B-W); the enhanced effective thickness approach (EET); the numerical simulations.

written as

$$g(x, y) = p\,a^4 \tag{4-8}$$
$$\times \sum_{m=1,3,5,\ldots}^{\infty} \left[\frac{4}{\pi^5 m^5} + A_m \cosh\frac{m\pi y}{a} + B_m \frac{m\pi y}{a} \sinh\frac{m\pi y}{a} + C_m \sinh\frac{m\pi y}{a} + D_m \frac{m\pi y}{a} \cosh\frac{m\pi y}{a} \right] \sin\frac{m\pi x}{a}$$

By imposing the relevant boundary conditions, one finds with some effort the values of the constants appearing in (4-8) in the form

$$A_m = -\frac{4}{\pi^5 m^5}, \quad B_m = \frac{2}{\pi^5 m^5}, \quad D_m = \frac{(2((3-\nu)S^2 + 2\nu C(C-1)))a}{((3+\nu)CSa + (1-\nu)\pi bm)\pi^5 m^5},$$
$$C_m = \frac{2(\pi^2 m^2 (1-\nu)^2 b^2 + 2\nu(1-\nu)m\pi Sab + (2\nu C(C-1)(1+\nu) - 2S^2(3-\nu))a^2)}{(1-\nu)((3+\nu)CSa + (1-\nu)\pi bm)\pi^5 m^5 a}, \tag{4-9}$$

where $C = \cosh(m\pi b/a)$ and $S = \sinh(m\pi b/a)$. Figure 12 shows the graph of the first-order approximation of the shape function. The coefficient Ψ to calculate η^* from (3-12) is tabulated in Table 3 again as a function of a and $\lambda = b/a$.

It is evident, from Figure 13, that the enhanced effective thickness approach and the Bennison–Wölfel model give, in the case at hands, slightly different results; the data obtained numerically are in favor of the approach proposed here.

4.4. ***Rectangular plates resting on corner points.*** The case of rectangular plates point-wise supported at the corners under uniform pressure (Figure 5d) is of particular interest for frameless glazing, but presents some difficulty because even the elastic solution for the monolith is not simple. The first attempts of analytical solutions were given by Galerkin [1915] and Nádai [1922]. Then Wang et al. [2002] proved

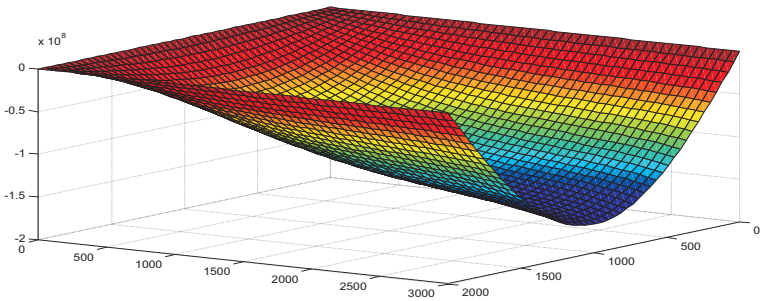

Figure 12. Shape function for rectangular plates with three simply supported sides. Case $a = 3000\,\text{mm}$, $b = 2000\,\text{mm}$.

a[mm] \ λ	0.2	0.4	0.6	0.8	1	1.25	1.667	2.5	5
500	0.5982	0.5578	0.5168	0.4855	0.4640	0.4465	0.4300	0.4156	0.4166
1000	0.1495	0.1394	0.1292	0.1214	0.1160	0.1116	0.1075	0.1039	0.1041
1500	0.0665	0.0620	0.0574	0.0539	0.0516	0.0496	0.0478	0.0462	0.0441
2000	0.0374	0.0349	0.0323	0.0303	0.0290	0.0279	0.0269	0.0260	0.0260
2500	0.0239	0.0223	0.0207	0.0194	0.0186	0.0179	0.0172	0.0166	0.0171
3000	0.0166	0.0155	0.0144	0.0135	0.0129	0.0124	0.0119	0.0115	0.0110

Table 3. Coefficient Ψ (in $\text{mm}^{-2} \times 10^4$) for rectangular plates with three edges simply supported.

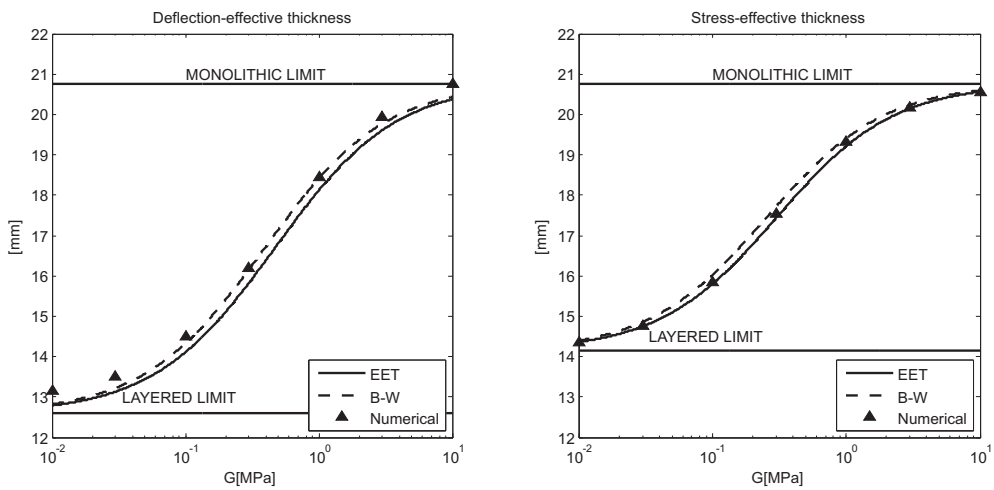

Figure 13. Rectangular plates with three simply supported edges, case $a = 3000\,\text{mm}$, $b = 2000\,\text{mm}$. Comparison of the effective thicknesses obtained with: Bennison–Wölfel approach (B-W); the enhanced effective thickness approach (EET); the numerical simulations.

that such works, focused on determining the deflection, produce rather inaccurate results in terms of stress. Batista [2010] presented a solution in form of trigonometric series , where the coefficients of the series form a regular *infinite* system of linear equations, providing accurate results for deflection, moment

and shear forces. Therefore, following Batista, the deflection of a monolith of flexural stiffness D is here expressed in the form

$$w(x,y)=\frac{p}{48(1-\nu)D}\left[5(a^4+b^4)-6\nu a^2b^2-6(a^2-\nu b^2)x^2-6(b^2-\nu a^2)y^2+x^4-6\nu x^2y^2+y^4\right]$$
$$+\frac{p}{D}\sum_{n=0}^{\infty}(-1)^n B_n\left[\left(\frac{\sinh(\alpha_n b)}{\cosh(\alpha_n b)}+\frac{2}{(1-\nu)\alpha_n b}\right)b\cosh(\alpha_n y)-y\sinh(\alpha_n y)\right]\frac{\cos(\alpha_n x)}{a\cosh(\alpha_n b)}$$
$$+\frac{p}{D}\sum_{n=0}^{\infty}(-1)^n D_n\left[\left(\frac{\sinh(\beta_n a)}{\cosh(\beta_n a)}+\frac{2}{(1-\nu)\beta_n a}\right)a\cosh(\beta_n y)-x\sinh(\beta_n y)\right]\frac{\cos(\beta_n y)}{b\cosh(\beta_n a)},\quad (4\text{-}10)$$

where $\alpha_n=(2n+1)\pi/(2a)$ and $\beta_n=(2n+1)\pi/(2b)$. The coefficients B_n and D_n can be found by expanding into a trigonometric series the boundary condition of null vertical forces on the free edges. By taking, as in the previous cases, just the first-order approximation, the shape function $g(x,y)$ reads

$$g(x,y)=\frac{p}{48(1-\nu)}\left[5(a^4+b^4)-6\nu a^2b^2-6(a^2-\nu b^2)x^2-6(b^2-\nu a^2)y^2+x^4-6\nu x^2y^2+y^4\right]$$
$$+pB_0\left[\left(\frac{\sinh(\alpha_0 b)}{\cosh(\alpha_0 b)}+\frac{2}{(1-\nu)\alpha_0 b}\right)b\cosh(\alpha_0 y)-y\sinh(\alpha_0 y)\right]\frac{\cos(\alpha_0 x)}{a\cosh(\alpha_0 b)}$$
$$+pD_0\left[\left(\frac{\sinh(\beta_0 a)}{\cosh(\beta_0 a)}+\frac{2}{(1-\nu)\beta_0 a}\right)a\cosh(\beta_0 y)-x\sinh(\beta_0 y)\right]\frac{\cos(\beta_0 y)}{b\cosh(\beta_0 a)},\quad (4\text{-}11)$$

where the coefficients B_0 and D_0 are given by

$$B_0=16a^4b\,C_{ba}^2(1-\nu)\left[-a(1-\nu)\pi^2+2b\,S_{ab}C_{ab}(3+\nu)\pi+\frac{16ab^4}{(b^2+a^2)^2}C_{ab}^2(1-\nu)\right]\Big/Q,$$
$$D_0=16a^4b\,C_{ba}^2(1-\nu)\left[-b(1-\nu)\pi^2+2a\,S_{ba}C_{ba}(3+\nu)\pi+\frac{16a^4b}{(b^2+a^2)^2}C_{ba}^2(1-\nu)\right]\Big/Q,\quad (4\text{-}12)$$

with

$$Q=\pi^2(ab(1-\nu)^2\pi^4-2(3+\nu)(1-\nu)(C_{ba}S_{ba}\,a^2+S_{ab}C_{ab}\,b^2)\pi^3$$
$$+4ab\,S_{ab}S_{ba}C_{ba}C_{ab}(3+\nu)^2\pi^2-\frac{256a^5b^5}{(b^2+a^2)^4}\,C_{ab}^2C_{ba}^2(1-\nu)^2),$$
$$C_{ab}=\cosh^2(\alpha_0 b),\quad S_{ab}=\sinh^2(\alpha_0 b),\quad C_{ba}=\cosh(\beta_0 a),\quad S_{ba}=\sinh(\beta_0 a).\quad (4\text{-}13)$$

The shape function thus obtained is plotted in Figure 14.

The coefficient η^* may be determined through (3-11) or (4-1) as a function of the material properties and of the coefficient Ψ of (3-12), tabulated in Table 4.

Figure 15 shows the comparison between the deflection- and stress-effective thickness calculated according to EET and B-W approaches, for the case $a=3000$ mm, $b=2000$ mm. From this, it is evident that the EET and B-W give substantially different results. For what concerns the stress-effective thickness, numerical experiments are in favor of our present proposal.

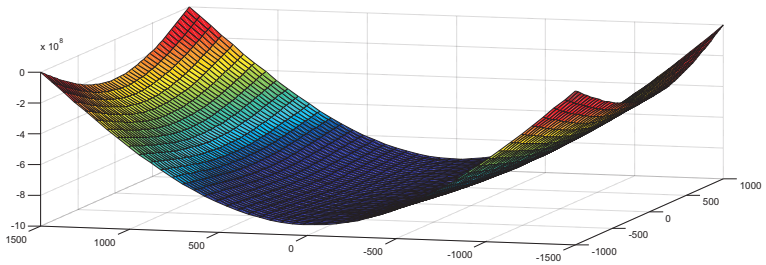

Figure 14. Shape function for rectangular plates resting on corner points. Case $a = 3000\,\text{mm}$, $b = 2000\,\text{mm}$.

a[mm] \ λ	0.1	0.2	0.3	0.4	0.5	0.6	0.7	0.8	0.9	1
500	0.6112	0.5982	0.5793	0.5578	0.5363	0.5168	0.4998	0.4855	0.4737	0.4640
1000	0.1528	0.1495	0.1448	0.1394	0.1341	0.1292	0.1249	0.1214	0.1184	0.1160
1500	0.0679	0.0665	0.0644	0.0620	0.0596	0.0574	0.0555	0.0539	0.0526	0.0516
2000	0.0382	0.0374	0.0362	0.0349	0.0335	0.0323	0.0312	0.0303	0.0296	0.0290
2500	0.0244	0.0239	0.0232	0.0223	0.0215	0.0207	0.0200	0.0194	0.0189	0.0186
3000	0.0170	0.0166	0.0161	0.0155	0.0149	0.0144	0.0139	0.0135	0.0132	0.0129

Table 4. Coefficient Ψ (in $\text{mm}^{-2} \times 10^4$) for rectangular plates resting on corner points.

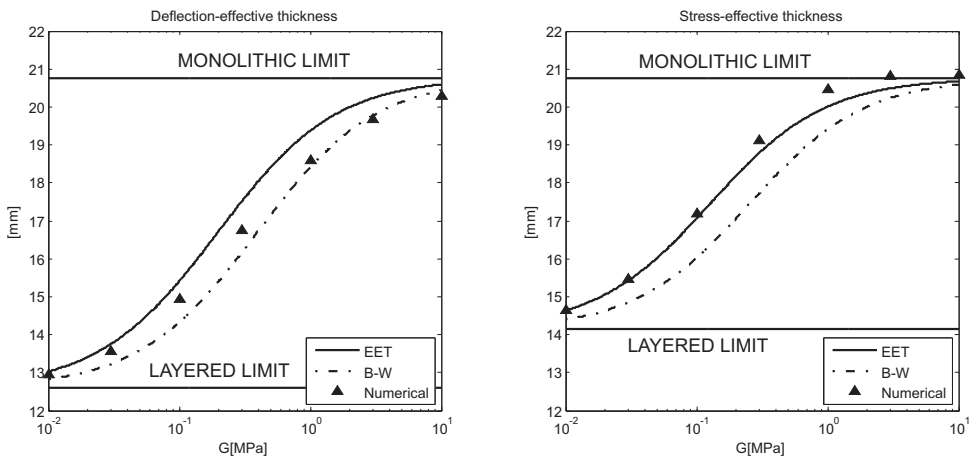

Figure 15. Rectangular plates supported at corner points, case $a = 3000\,\text{mm}$, $b = 2000\,\text{mm}$. Comparison of the effective thicknesses obtained with: Bennison–Wölfel approach (B-W); the enhanced effective thickness approach (EET); the numerical simulations.

Figure 16 shows the deflection- and stress-effective thickness for a 2000 mm $\times$2000 mm square plate supported on corner points. Once again, in this case experimental results are better fitted through the EET approach.

Whenever $b \gg a$, the plate deformed shape tends to be cylindrical and, consequently, the behavior close to that of a beam. This is why for the case $a = 6000\,\text{mm}$ and $b = 2000\,\text{mm}$, recorded in Figure 17, B-W and EET give results that in practice coincide, in agreement with the numerical simulations.

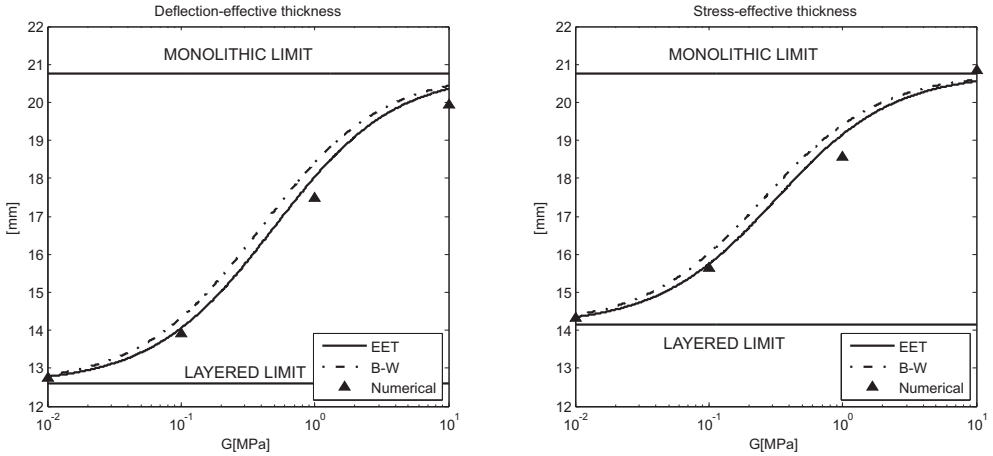

Figure 16. Square plates supported at corner points, case $a = 2000\,\text{mm}$, $b = 2000\,\text{mm}$. Comparison of the effective thicknesses obtained with: Bennison–Wölfel approach (B-W); the enhanced effective thickness approach (EET); the numerical simulations.

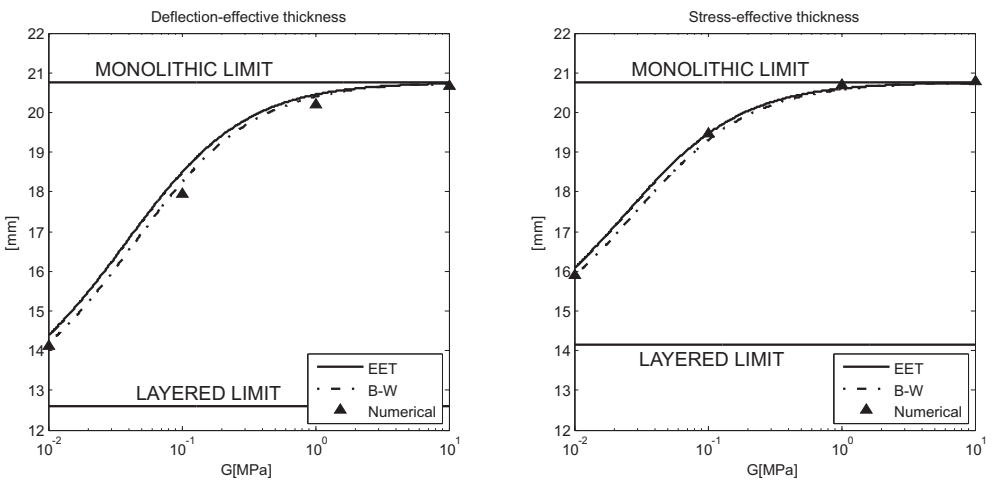

Figure 17. Rectangular plates supported at corner points, case $a = 6000\,\text{mm}$, $b = 2000\,\text{mm}$. Comparison of the effective thicknesses obtained with: Bennison–Wölfel approach (B-W); the enhanced effective thickness approach (EET); the numerical simulations.

5. Discussion and conclusions

Although it is possible to calculate numerically, and with excellent precision, the state of strain and stress in laminated glass of any composition, size and shape, under the most various boundary and load conditions, nevertheless simplified methods based upon the notion of effective thickness still remain a very powerful tool, especially in the first preliminary phases of the design procedure. The designers need simple expressions that allow to readily determine the structural response of laminated glass, leaving

more sophisticated computer methods to the final verifications. The most important result of this study has been the definition of simple formulas for the effective thickness that can be applied, in principle, to the two-dimensional problems of plates of any shape and size, under any boundary and load conditions. This method is not recommended to evaluate local effects, such as stress concentrations around holes and/or at contact points, but can be conveniently used to calculate maximum deflection and stress with good accuracy, as confirmed by numerical and analytical approaches [Foraboschi 2012].

The key point is the assumption of a shape-function $g(x, y)$ for the flexural-deformation surface of the laminate, which, in accord with (3-4), is taken equal to the deflection of a monolithic plate of arbitrary thickness with equal boundary and load conditions. Such a shape function may be estimated analytically, when an analytical though approximate solution is available, or even numerically, when this is not the case. From this, one can define the *deflection-* and *stress-effective thicknesses* of the laminate, by using the simple formulas (3-13) and (3-17). These are defined by a parameter η^*, indicating the shear coupling offered by the polymeric interlayer, whose form can be calculated from expression (3-11), which in turn is defined by the parameter Ψ, given by (3-12) as a function of the pressure distribution on the plate, $p(x, y)$, and of the shape function $g(x, y)$. Indeed, the only "difficulty" of the proposed method, here referred to as the enhanced effective thickness approach (EET), consists in calculating Ψ from (3-12), which involves integration of $p(x, y)$ and $g(x, y)$ over the referential domain of the plate, in accord with (3-12). Here, we have exemplified this procedure for the case, very important in the design practice, of a rectangular laminated glass plates under uniformly distributed pressure.

The shape function $g(x, y)$ has been approximated by the first term of the series expansion for the deflection surface of a monolithic plate, arriving at simple expressions for Ψ, whose values have been recorded in the tables of figures 1, 2, 3 and 4 for various boundary conditions at the borders. Comparisons with the results obtained with the classical formulas for the effective thickness *à la* Bennison–Wölfel (B-W), in accordance with (1-5), (1-6) and (1-7), and with the results from accurate numerical models, highlight the better accuracy that is obtained with the proposed EET approach. Indeed, the B-W approach assumes that laminated glass is a simply supported beam under uniformly distributed load; it then turns out to be reliable only when the flexural deformation of the plate is cylindrical, i.e., in the case of rectangular plates simply supported at two opposite sides. We have also shown that the use of B-W formulation is not always on the side of safeness because they are cases, like that of a laminated plate point-wise supported at the corners, where B-W gives effective thicknesses that underestimate both deflection and stress.

A more general and comprehensive treatment of other relevant problems for laminated glass design has been recorded in [Galuppi et al. 2012]. Here, the EET method is applied to the most common cases of the design practice including plates under pseudoconcentrated loads, providing synthetic tables for ease of reference and immediate applicability. The extension of the enhanced effective thickness approach to other cases, like that of curved plates and shells, presents in principle no further conceptual difficulty, and it will be the subject of future work.

Acknowledgements

Gianni Royer-Carfagni acknowledges the Italian MURST for its partial support under the PRIN2008 program.

References

[Aşik 2003] M. Z. Aşik, "Laminated glass plates: revealing of nonlinear behavior", *Comput. Struct.* **81**:28–29 (2003), 2659–2671.

[Aşik and Tezcan 2005] M. Z. Aşik and S. Tezcan, "A mathematical model for the behavior of laminated glass beams", *Comput. Struct.* **83**:21–22 (2005), 1742–1753.

[Batista 2010] M. Batista, "New analytical solution for bending problem of uniformly loaded rectangular plate supported on corner point", *IES J. A Civ. Struct. Eng.* **3**:2 (2010), 75–84.

[Behr et al. 1993] R. A. Behr, J. E. Minor, and H. S. Norville, "Structural behavior of architectural laminated glass", *J. Struct. Eng.* (*ASCE*) **119**:1 (1993), 202–222.

[Bennison 2009] S. J. Bennison, "Structural properties of laminated glass", short course presented at *Glass performance days* (Tampere), 2009.

[Bennison et al. 1999] S. J. Bennison, A. Jagota, and C. A. Smith, "Fracture of glass/poly(vinyl butyral) (Butacite®) laminates in biaxial flexure", *J. Am. Ceram. Soc.* **82**:7 (1999), 1761–1770.

[Bennison et al. 2001] S. J. Bennison, C. A. Smith, A. Van Duser, and A. Jagota, "Structural performance of laminated glass made with a 'stiff' interlayer", pp. 283–287 in *Glass processing days* (Tampere, 2001), edited by J. Vitkala, Tamglass, Tampere, 2001.

[Bennison et al. 2005] S. J. Bennison, J. G. Sloan, D. F. Kristunas, P. J. Buehler, T. Amos, and C. A. Smith, "Laminated glass for blast mitigation: role of interlayer properties", in *Glass processing days* (Tampere, 2005), Glaston Finland/GPD, Tampere, 2005.

[Bennison et al. 2008] S. J. Bennison, M. H. X. Qin, and P. S. Davies, "High-performance laminated glass for structurally efficient glazing", paper presented at conference on *Innovative light-weight structures and sustainable facades* (Hong Kong), 2008, available at http://tinyurl.com/Bennison-et-al-2008.

[Calderone et al. 2009] I. Calderone, P. S. Davies, S. J. Bennison, X. Huang, and L. Gang, "Effective laminate thickness for the design of laminated glass", in *Glass performance days* (Tampere, 2009), Glaston Finland/GPD, Tampere, 2009.

[Cas et al. 2007] B. Cas, M. Saje, and I. Planinc, "Buckling of layered wood columns", *Adv. Eng. Softw.* **38**:8–9 (2007), 586–597.

[Foraboschi 2007] P. Foraboschi, "Behavior and failure strength of laminated glass beams", *J. Eng. Mech.* (*ASCE*) **133**:12 (2007), 1290–1301.

[Foraboschi 2012] P. Foraboschi, "Analytical model for laminated-glass plate", *Compos. B Eng.* **43**:5 (2012), 2094–2106.

[Galerkin 1915] B. G. Galerkin, "Стержин и пластинки: ряды в некоторых волросах упругого равновесия стержней и пластинок", *Vestn. Inzh. Tekh.* (*USSR*) **1**:19 (1915), 897–908. In Russian; translated as *Rods and plates: series in some questions of elastic equilibrium of rods and plates*, National Technical Information Service, Springfield, VA, 1968.

[Galuppi and Royer-Carfagni 2012] L. Galuppi and G. F. Royer-Carfagni, "Effective thickness of laminated glass beams: new expressions via a variational approach", *Eng. Struct.* **38** (2012), 53–67.

[Galuppi et al. 2012] L. Galuppi, G. Manara, and G. F. Royer-Carfagni, "Practical expressions for the design of laminated glass", 2012, available at http://hdl.handle.net/1889/1720.

[Hooper 1973] J. A. Hooper, "On the bending of architectural laminated glass", *Int. J. Mech. Sci.* **15**:4 (1973), 309–323.

[Ivanov 2006] I. V. Ivanov, "Analysis, modelling, and optimization of laminated glasses as plane beam", *Int. J. Solids Struct.* **43**:22-23 (2006), 6887–6907.

[Knops and Payne 1971] R. J. Knops and L. E. Payne, *Uniqueness theorems in linear elasticity*, Springer, New York, 1971.

[Le Grognec et al. 2012] P. Le Grognec, Q.-H. Nguyen, and M. Hjiaj, "Exact buckling solution for two-layer Timoshenko beams with interlayer slip", *Int. J. Solids Struct.* **49**:1 (2012), 143–150.

[Louter et al. 2010] C. Louter, J. Belis, F. Bos, D. Callewaert, and F. Veer, "Experimental investigation of the temperature effect on the structural response of SG-laminated reinforced glass beams", *Eng. Struct.* **32**:6 (2010), 1590–1599.

[Murakami 1984] H. Murakami, "A laminated beam theory with interlayer slip", *J. Appl. Mech.* (*ASME*) **51**:3 (1984), 551–559.

[Nádai 1922] A. Nádai, "Über die Biegung durchlaufender Platten und der rechteckigen Platte mit freien Rändern", *Z. Angew. Math. Mech.* **2**:1 (1922), 1–26.

[Newmark et al. 1951] N. M. Newmark, C. P. Siess, and I. M. Viest, "Test and analysis of composite beams with incomplete interaction", *Proc. Soc. Exp. Stress Anal.* **9**:1 (1951), 75–92.

[Norville et al. 1998] H. S. Norville, K. W. King, and J. L. Swofford, "Behavior and strength of laminated glass", *J. Eng. Mech. (ASCE)* **124**:1 (1998), 46–53.

[Sagan 1969] H. Sagan, *Introduction to the calculus of variations*, McGraw-Hill, New York, 1969. Reprinted Dover, New York, 1992.

[Schnabl and Planinc 2011] S. Schnabl and I. Planinc, "The effect of transverse shear deformation on the buckling of two-layer composite columns with interlayer slip", *Int. J. Non-Linear Mech.* **46**:3 (2011), 543–553.

[Timoshenko and Woinowsky-Krieger 1971] S. P. Timoshenko and S. Woinowsky-Krieger, *Theory of plates and shells*, McGraw-Hill, New York, 1971.

[Wang et al. 2002] C. M. Wang, Y. C. Wang, and J. N. Reddy, "Problems and remedy for the Ritz method in determining stress resultants of corner supported rectangular plates", *Comput. Struct.* **80**:2 (2002), 145–154.

[Wölfel 1987] E. Wölfel, "Nachgiebiger Verbund: eine Näherungslösung und deren Anwendungsmöglichkeiten", *Stahlbau* **56**:6 (1987), 173–180.

[Xu and Wu 2007] R. Xu and Y. Wu, "Static, dynamic, and buckling analysis of partial interaction composite members using Timoshenko's beam theory", *Int. J. Mech. Sci.* **49**:10 (2007), 1139–1155.

Received 30 Nov 2011. Revised 1 Mar 2012. Accepted 16 Mar 2012.

LAURA GALUPPI: laura.galuppi@unipr.it
Civil-Environmental Engineering and Architecture, University of Parma, Parco Area delle Scienze 181/A, I, 43124 Parma, Italy

GIANNI ROYER-CARFAGNI: gianni.royer@unipr.it
Civil-Environmental Engineering and Architecture, University of Parma, Parco Area delle Scienze 181/A, I, 43124 Parma, Italy

JOURNAL OF MECHANICS OF MATERIALS AND STRUCTURES
Vol. 7, No. 4, 2012

ELASTIC SOLUTION IN A FUNCTIONALLY GRADED COATING SUBJECTED TO A CONCENTRATED FORCE

ROBERTA SBURLATI

Functionally graded materials are currently being actively explored in coating design to reduce the mismatch of thermomechanical properties at the interface and thus increase the resistance of coatings to fracture mechanisms. Many established and potential applications of graded materials involve contact or impact problems that are primarily load transfer problems; consequently, the goal is to study basic elasticity problems for graded inhomogeneous solids. Here we study the three-dimensional elastic deformation of a graded coating subjected to a point load on the free surface, deposited on a homogeneous elastic half-space. By assuming an isotropic coating for which Young's modulus depends exponentially on the thickness and Poisson's ratio is constant, the elastic solution is obtained using Plevako's representation, which reduces the problem to the construction of a potential function satisfying a linear fourth-order partial differential equation. We explicitly obtain the elastic solution for the coating and the substrate for two different interface conditions: the frictionless case and the perfectly bonded case. A comparative study of FGMs and homogeneous coatings is presented to investigate the effect of the graded coating properties.

1. Introduction

Functionally graded materials (FGMs) are two-phase composites with continuously varying volume fractions. Owing to the importance of the engineering applications of these materials, the thermomechanical behavior of FGM coatings has been investigated by many researchers [Suresh 2001]. The concept of grading the thermomechanical properties of materials provides an important tool to design new materials for certain specific functions. To take full advantage of this new tool, research is needed for developing efficient processing methods and material characterization techniques. If FGMs are used as coatings or in interfacial zones, they can reduce the thermally and mechanically induced stresses resulting from material property mismatches and, consequently, the risk of cracks and debonding of the coating or layer. Most studies of FGM coatings on substrates have focused on their fracture mechanisms, contact and impact response, and vibrational and thermoelastic behavior [Erdogan 1995; Birman and Byrd 2007].

The problem of a concentrated force acting normally to the free surface of a semi-infinite solid is of interest in contact mechanics. For example, Martin et al. [2002] studied it for a functional exponentially graded unbonded elastic solid subjected to a point force by assuming that the Lamé moduli vary exponentially in a given fixed direction, and obtained solutions that allow the development of boundary-integral methods for graded materials.

Various studies have considered the elastic response of a functionally graded coating deposited on a substrate. Kashtalyan and Menshykova [2008] determined a three-dimensional elastic solution of a

Work financed by the Italian Ministry of Education, University, and Research (MIUR), Project No. 2009XWLFKW: "Multiscale modeling of materials and structures".
Keywords: elasticity, coating, functionally graded materials.

functionally graded coating on a homogeneous finite thickness elastic substrate subjected to mechanical loading. By assuming that the elasticity modulus varies exponentially through the thickness of the coating, the solution allows the authors to analyze the effects of the coating type on the stress and displacement fields. [Liu and Wang 2008] studied the problem of a functionally graded coating half-space indented by an axisymmetric smooth rigid punch by using the Hankel integral transform technique to reduce the contact problem to a Cauchy singular equation to be solved numerically.

The aim of this paper is to study the three-dimensional elastic deformation of a functionally graded coating deposited on a homogeneous substrate subjected to a point load. We investigate the interface between the coating and the substrate in order to describe the difference in behavior due to localized damage. For this reason, we consider two ideal interface conditions: the perfectly bonded case and the frictionless contact case. (Real interface conditions lie in between: the contact is neither frictionless nor perfectly bonded.) In the isotropic coating, the Young's modulus depends exponentially on the position along the thickness, while the Poisson ratio is assumed to be constant and equal to the homogeneous substrate. Similar investigations have been performed to describe the elastic response in indentation tests on homogeneous films [Sburlati 2009a].

The solution is obtained in the framework of three-dimensional elasticity using Plevako's representation form [1971], which reduces the problem to determining a potential function satisfying a linear fourth-order partial differential equation. We explicitly obtain the solution by writing the potential function in terms of a Bessel expansion with respect to the radial coordinate [Sneddon 1966]. We investigate the stresses and displacements with respect to the corresponding homogeneous coating, and show that there is an increase of the radial stress on the free surface and a reduction on the interface zone due to the graded properties. Furthermore, the different interface conditions permit us to study the effects of localized interface damage in order to provide useful suggestions for the design of graded coatings.

2. Formulation of the problem

We consider a functionally graded material coating of thickness h deposited on a homogeneous substrate subjected to a point load on the upper face (see Figure 1). We introduce a cylindrical coordinate system

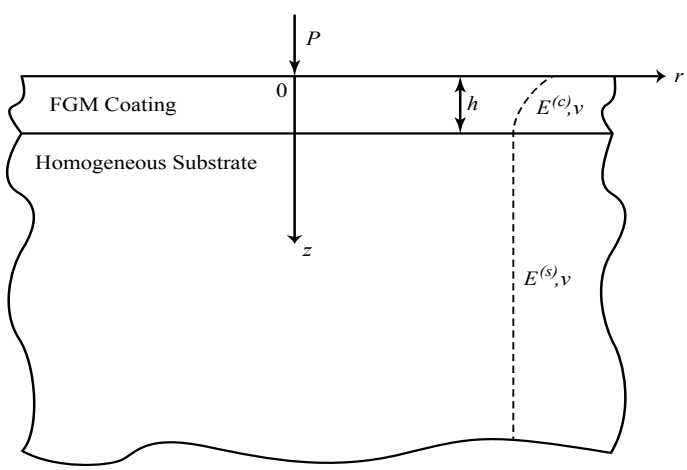

Figure 1. Sketch of the problem.

and assume that in the coating, the Young's modulus varies exponentially in the z-direction and that it is homogeneous and isotropic in the substrate:

$$E^{(c)}(z) = E_0\, e^{2kz}, \quad E^{(s)}(z) = E_h = E_0\, e^{2kh}, \tag{2-1}$$

while the Poisson ratios $\nu_c = \nu_s = \nu$ are uniform.

We denote the quantities in the coating by $(i) = (c)$ and the quantities in the substrate by $(i) = (s)$. Assuming a null body force, the elasticity equations are [Love 1927]:

$$\nabla^2 u^{(i)} - \frac{u^{(i)}}{r^2} + \frac{1}{1-2\nu}\frac{\partial \Theta^{(i)}}{\partial r} + \left(\frac{\partial u^{(i)}}{\partial z} + \frac{\partial w^{(i)}}{\partial r}\right)\frac{1}{E^{(i)}(z)}\frac{d}{dz}E^{(i)}(z) = 0, \tag{2-2}$$

$$\nabla^2 w^{(i)} + \frac{1}{1-2\nu}\frac{\partial \Theta}{\partial z} + \left(\frac{\partial w^{(i)}}{\partial z} + \frac{\nu}{1-2\nu}\,\Theta^{(i)}\right)\frac{2}{E^{(i)}(z)}\frac{d}{dz}E^{(i)}(z) = 0,$$

where

$$\Theta^{(i)} = \frac{\partial u^{(i)}}{\partial r} + \frac{u^{(i)}}{r} + \frac{\partial w^{(i)}}{\partial z}.$$

The load conditions on the free surface of the coating are

$$\sigma_z^{(c)}(r, 0) = -P\delta(\boldsymbol{r}) = -\frac{P\delta(r)}{\pi r}, \quad \tau_{rz}^{(c)}(r, 0) = 0, \tag{2-3}$$

where δ denotes the Dirac function. We study the problem for *perfectly bonded* and *frictionless contact* interface conditions.

In the perfectly bonded case we assume continuity of the displacement and stress components:

$$\begin{aligned} w^{(c)}(r, h) &= w^{(s)}(r, h), \quad u^{(c)}(r, h) = u^{(s)}(r, h), \\ \sigma_z^{(c)}(r, h) &= \sigma_z^{(s)}(r, h), \quad \tau_{rz}^{(c)}(r, h) = \tau_{rz}^{(s)}(r, h). \end{aligned} \tag{2-4}$$

In the frictionless contact case, we assume

$$w^{(c)}(r, h) = w^{(s)}(r, h), \quad \sigma_z^{(c)}(r, h) = \sigma_z^{(s)}(r, h), \quad \tau_{rz}^{(c)}(r, h) = \tau_{rz}^{(s)}(r, h) = 0. \tag{2-5}$$

In both cases, in the substrate, we set

$$\lim_{z\to\infty} \sigma_z^{(s)}(r, z) = 0, \quad \lim_{z\to\infty} \tau_{rz}^{(s)}(r, z) = 0. \tag{2-6}$$

3. Solution technique

In order to find the elastic solution we adopt Plevako's approach [1971] for an axisymmetric problem. To this end, the displacement field is expressed in terms of a potential function $L(r, z)$, in the form

$$u^{(i)}(r, z) = -\frac{1+\nu}{E^{(i)}(z)}\frac{\partial}{\partial r}\left(\nu\nabla_r^2 L^{(i)} - (1-\nu)\frac{\partial^2}{\partial z^2}L^{(i)}\right), \tag{3-1}$$

$$w^{(i)}(r, z) = -\frac{2(1+\nu)}{E^{(i)}(z)}\frac{\partial}{\partial z}\nabla_r^2 L^{(i)} + (1+\nu)\frac{\partial}{\partial z}\left[\frac{1}{E^{(i)}(z)}\left(\nu\nabla_r^2 L^{(i)} - (1-\nu)\frac{\partial^2}{\partial z^2}L^{(i)}\right)\right], \tag{3-2}$$

where ∇_r^2 is the radial Laplace operator. The function $L^{(i)}(r, z)$ is required to satisfy the Plevako equation

$$\nabla^2 \left(\frac{1}{E^{(i)}(z)} \nabla^2 L^{(i)} \right) - \frac{1}{1-\nu} \nabla_r^2 L^{(i)} \frac{d^2}{dz^2} \frac{1}{E^{(i)}(z)} = 0. \tag{3-3}$$

The stress field components assume the form

$$\begin{aligned}
\sigma_r^{(i)}(r, z) &= \frac{\nu}{r} \frac{\partial}{\partial r} \nabla_r^2 L^{(i)} + \frac{\partial^2}{\partial z^2} \nabla_r^2 L^{(i)} - \frac{1-\nu}{r} \frac{\partial^3}{\partial r \partial z^2} L^{(i)}, \\
\sigma_\theta^{(i)}(r, z) &= \nu \nabla_r^4 L^{(i)} - \frac{\nu}{r} \frac{\partial}{\partial r} \nabla_r^2 L^{(i)} + \nu \frac{\partial^2}{\partial z^2} \nabla_r^2 L^{(i)} + \frac{1-\nu}{r} \frac{\partial^3}{\partial r \partial z^2} L^{(i)}, \\
\tau_{rz}^{(i)}(r, z) &= -\frac{\partial^2}{\partial r \partial z} \nabla_r^2 L^{(i)}, \quad \sigma_z^{(i)}(r, z) = \nabla_r^4 L^{(i)}.
\end{aligned} \tag{3-4}$$

By using (2-1), we obtain from (3-3)

$$\nabla_r^4 L^{(c)} + 2 \left(\frac{\partial^2}{\partial z^2} - 2k \frac{\partial}{\partial z} - 2k^2 \omega^2 \right) \nabla_r^2 L^{(c)} + \left(\frac{\partial^2}{\partial z^2} - 4k \frac{\partial}{\partial z} + 4k^2 \right) \frac{\partial^2}{\partial z^2} L^{(c)} = 0 \tag{3-5}$$

and

$$\nabla_r^4 L^{(s)} + 2 \frac{\partial^2}{\partial z^2} \nabla_r^2 L^{(s)} + \frac{\partial^4}{\partial z^4} L^{(s)} = 0, \tag{3-6}$$

where $\omega^2 = \nu/(1-\nu)$.

In this work, we assume that the elastic deformation is contained within a cylindrical region of some radius $b > h$; in other words, the displacement field and the Plevako function are null for $r \geq b$.

Now, we write the Plevako function with the following Fourier–Bessel expansion [Sneddon 1966; Watson 1922]:

$$L^{(i)}(r, z) = \sum_{j=1}^{\infty} L_j^{(i)}(z)\, J_0(\phi_j r), \quad \text{where } \phi_j = \frac{z_j^{(0)}}{b} \tag{3-7}$$

and where the $z_j^{(0)}$, for $j = 1, 2, \ldots$, are the positive roots of $J_0(x)$, Bessel function of order zero, and

$$L_j^{(i)}(z) = \frac{2}{b^2 J_1^2(\phi_j b)} \int_0^b L^{(i)}(\rho, z)\, J_0(\phi_j \rho)\, \rho \, d\rho.$$

We remark that this expansion, which assumes $L^{(i)}(b, z) = 0$, can be generalized to the case for which this assumption is not made. This requires the introduction of two suitable functions $\beta(z) = L(b, z)$, and $\alpha(z) = \nabla_r^2 L(r, z)|_{r=b}$ which, in turn, give rise to a different componentwise expression of the Plevako equation [Sburlati 2009b; Sburlati and Bardella 2011].

Returning to the present case, we substitute the expansion (3-7) into (3-5) and (3-6), obtaining

$$L_j^{(c)\prime\prime\prime\prime}(z) - 4k\, L_j^{(c)\prime\prime\prime}(z) + \left(4k^2 - 2\phi_j^2\right) L_j^{(c)\prime\prime}(z) + 4\phi_j^2 k\, L_j^{(c)\prime}(z) + \phi_j^2 (4k^2\omega^2 + \phi_j^2) L_j^{(c)}(z) = 0 \tag{3-8}$$

and

$$L_j^{(s)\prime\prime\prime\prime}(z) - 2\phi_j^2 L_j^{(s)\prime\prime}(z) + \phi_j^4 L_j^{(s)}(z) = 0. \tag{3-9}$$

The solution of (3-8) is

$$L_j^{(c)}(z) = e^{kz}\big[e^{\beta_j z}\big(A_j\cos(\alpha_j z) + B_j\sin(\alpha_j z)\big) + e^{-\beta_j z}\big(C_j\cos(\alpha_j z) + D_j\sin(\alpha_j z)\big)\big], \tag{3-10}$$

where

$$\alpha_j = \frac{\sqrt{2}}{2}\sqrt{\sqrt{k^4+\phi_j^4+2\,k^2\,\phi_j^2(2\,\omega^2+1)} - k^2 - \phi_j^2} \quad \text{and} \quad \beta_j = \frac{k\,\omega\,\phi_j}{\alpha_j},$$

while the solution of (3-9) is

$$L_j^{(s)}(z) = e^{\phi_j z}(T_j + z\,Q_j) + e^{-\phi_j z}(F_j + z\,G_j). \tag{3-11}$$

4. Explicit solution

Now we substitute the expansions of the Plevako functions $L^{(c)}(r,z)$ and $L^{(s)}(r,z)$ into (3-1), (3-2) and (3-4). Denoting the Heaviside step function by $H(x)$, we write

$$u(r,z) = \sum_{j=1}^{\infty}\big(H(h-z)u_j^{(c)}(z) + H(z-h)u_j^{(s)}(z)\big)J_1(\phi_j r) \tag{4-1}$$

and

$$w(r,z) = \sum_{j=1}^{\infty}\big(H(h-z)w_j^{(c)}(z) + H(z-h)w_j^{(s)}(z)\big)J_0(\phi_j r), \tag{4-2}$$

where

$$u_j^{(c)}(z) = -\frac{(1+\nu)\phi_j e^{-2kz}}{E_0}\big(\nu\phi_j^2 L_j^{(c)}(z) + (1-\nu)L_j^{(c)\,\prime\prime}(z)\big), \tag{4-3}$$

$$u_j^{(s)}(z) = -\frac{(1+\nu)\phi_j e^{-2kh}}{E_0}\big(\nu\phi_j^2 L_j^{(s)}(z) + (1-\nu)L_j^{(s)\,\prime\prime}(z)\big), \tag{4-4}$$

$$w_j^{(c)}(z) = \frac{e^{-2kz}}{E_0}\big((\nu-1)(L_j^{(c)\,\prime\prime\prime}(z) - 2kL_j^{(c)\,\prime\prime}(z)) + (2-\nu)\phi_j^2 L_j^{(c)\,\prime}(z) + 2k\nu\phi_j^2 L_j^{(c)}(z)\big), \tag{4-5}$$

$$w_j^{(s)}(z) = \frac{(1+\nu)e^{-2kh}}{E_0}\big((\nu-1)L_j^{(s)\,\prime\prime\prime}(z) + (2-\nu)\phi_j^2 L_j^{(s)\,\prime\prime}(z)\big). \tag{4-6}$$

The stress field is given by

$$\sigma_z(r,z) = \sum_{j=1}^{\infty}\phi_j^4\big(H(h-z)L_j^{(c)}(z) + H(z-h)L_j^{(s)}(z)\big)J_0(\phi_j r),$$

$$\tau_{rz}(r,z) = -\sum_{j=1}^{\infty}\phi_j^3\big(H(h-z)L_j^{(c)\,\prime}(z) + H(z-h)L_j^{(s)\,\prime}(z)\big)J_1(\phi_j r),$$

$$\sigma_r(r,z) = -\sum_{j=1}^{\infty}\phi_j^2\big(H(h-z)L_j^{(c)\,\prime\prime}(z) + H(z-h)L_j^{(s)\,\prime\prime}(z)\big)J_0(\phi_j r)$$

$$+\frac{1-\nu}{r}\sum_{j=1}^{\infty}\phi_j\big[H(h-z)\big(L_j^{(c)\,\prime\prime}(z)+\omega^2\phi_j^2 L_j^{(c)}(z)\big)+H(z-h)\big(L_j^{(s)\,\prime\prime}(z)+\omega^2\phi_j^2 L_j^{(s)}(z)\big)\big]J_1(\phi_j r),$$

$$\sigma_\theta(r,z) = -\nu \sum_{j=1}^{\infty} \phi_j^2 \left[H(h-z)\left(L_j^{(c)\,\prime\prime}(z) - \phi_j^2 L_j^{(c)}(z)\right) + H(z-h)\left(L_j^{(s)\,\prime\prime}(z) - \phi_j^2 L_j^{(s)}(z)\right)\right] J_0(\phi_j r)$$
$$- \frac{1-\nu}{r} \sum_{j=1}^{\infty} \phi_j \left[H(h-z)\left(L_j^{(c)\,\prime\prime}(z) + \omega^2 \phi_j^2 L_j^{(c)}(z)\right) + H(z-h)\left(L_j^{(s)\,\prime\prime}(z) + \omega^2 \phi_j^2 L_j^{(s)}(z)\right)\right] J_1(\phi_j r).$$

Plevako's functions $L_j^{(c)}(z)$ and $L_j^{(s)}(z)$ are now obtained by taking into account the values of the four series of coefficients A_j, B_j, C_j, D_j and T_j, Q_j, F_j, G_j determined by imposing the interface conditions. In both cases, we write the point load applied on the upper face as a Bessel expansion:

$$p(r) = -P\frac{\delta(r)}{r\pi} = \sum_{j=1}^{\infty} p_j\, J_0(\phi_j\, r), \quad \text{where } p_j = \frac{P}{\pi b^2\, J_1^2(\phi_j\, b)}. \tag{4-7}$$

Then the boundary conditions (2-3) and (2-6) give

$$C_j = -A_j - \frac{p_j}{\phi_j^4}, \quad D_j = \frac{p_j(k-\beta_j) - \phi_j^4(2\beta_j\, A_j + \alpha_j\, B_j)}{\phi_j^4 \alpha_j^4}, \quad T_j = 0, \quad Q_j = 0, \tag{4-8}$$

and the interface conditions allow us to obtain the remaining coefficients (see Appendix).

5. Numerical results

The numerical example presented here highlights the effects of material inhomogeneity using the analytic solution obtained in the previous section. We conduct a comparative study of FGM versus homogeneous coatings to examine the different behaviors with attention to the effects of the interface conditions between the coating and the substrate.

We choose a hardened coating ($k < 0$) where $E_0 = 200\,\text{GPa}$, $E_h = 20\,\text{GPa}$ and $\nu = 0.3$. For the comparative analysis, we consider a homogeneous coating with $E_c = E_0$, deposited on a soft homogenous substrate with $E_s = E_h$. In addition, for all cases we assume $h = 500\,\mu\text{m}$, $P = 2000\,\text{N}$ and $b = 20h$.

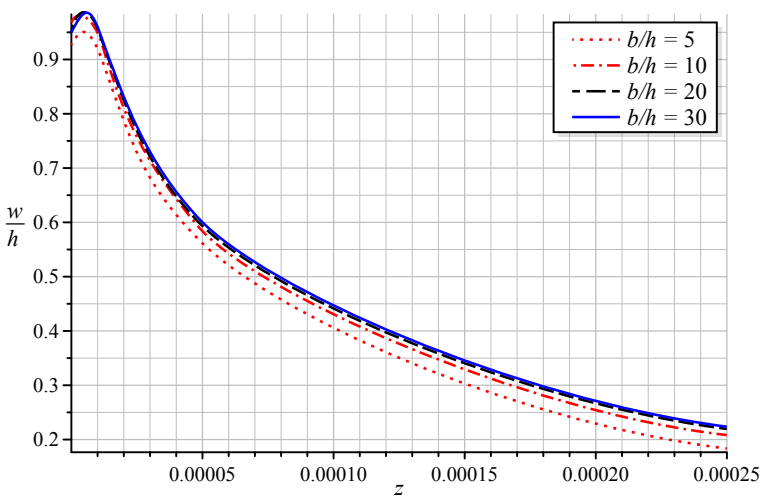

Figure 2. Normalized transversal displacements in the thickness for $b/h = 5, 10, 20, 30$.

We adopted this value for b because, according to a numerical sensitivity analysis, greater values of b do not affect the final results in these cases. To this end, in Figure 2 we plot the normalized transversal displacement for the case of a perfectly bonded interface condition, for the ratios $b/h = 5, 10, 20, 30$. Similar results can be obtained for radial displacement and stresses. We stress that the chosen value does not represent a specific material, but is used to better show the effect of the graded properties.

We now present some plots of normalized displacements and stresses throughout the thickness for two systems: a functionally graded coating on a homogeneous substrate (FGC) and a homogeneous coating on a homogeneous substrate (HC). For both systems, we consider the perfectly bonded (PB) and frictionless contact (FC) interface conditions.

In Figure 3, the normalized transversal displacement w/h at $r = 1/10h$ reveals, on the free surface, an increase of the order of 15% in the graded coating case compared to the homogeneous coating, The variation through the thickness of the normalized radial displacement, near the interface for $r = 1/10h$, is shown in Figure 4. It reveals very different behaviors for the two interface conditions. We observe that

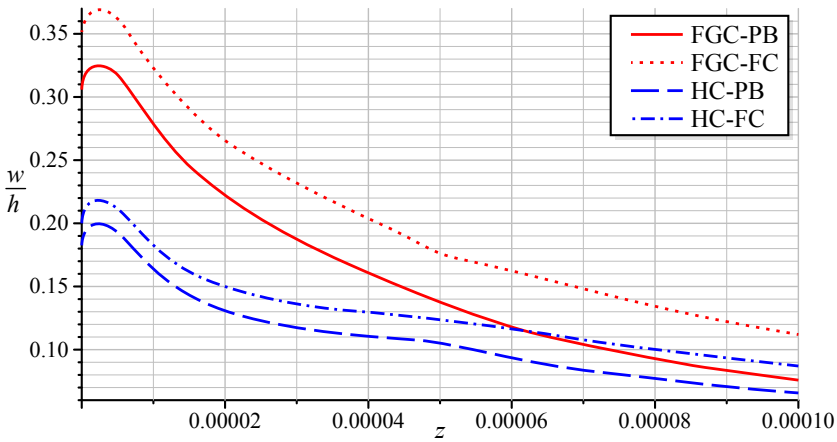

Figure 3. Normalized transversal displacements in the thickness for $r = 1/10\,h$.

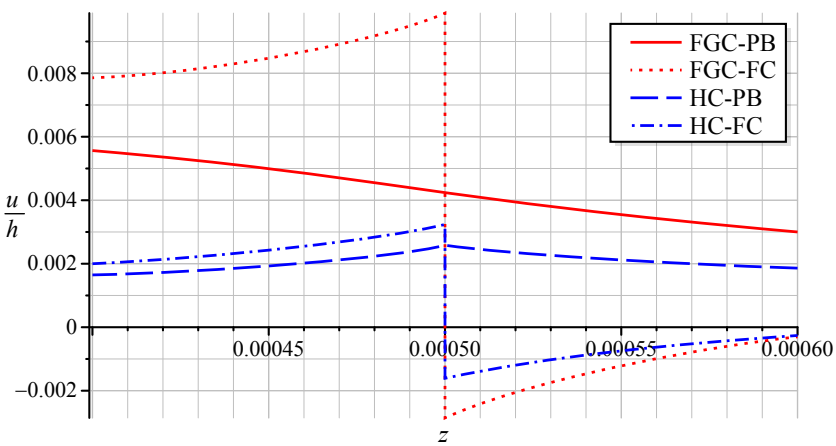

Figure 4. Normalized radial displacements near the interface for $r = 1/10\,h$.

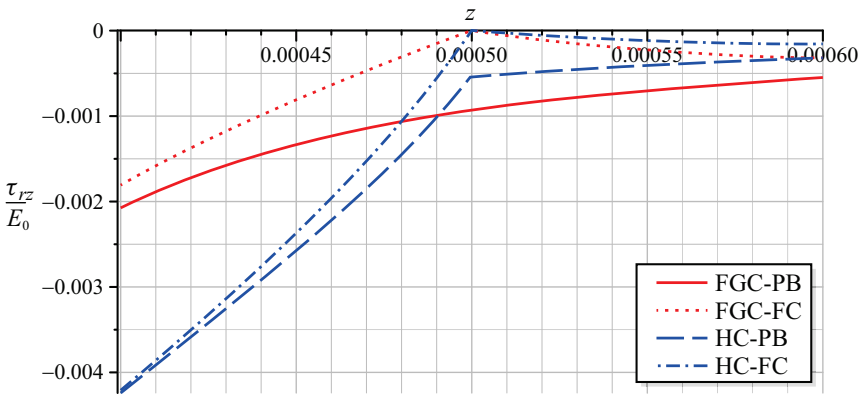

Figure 5. Normalized shear stresses near the interface for $r = 1/10\,h$.

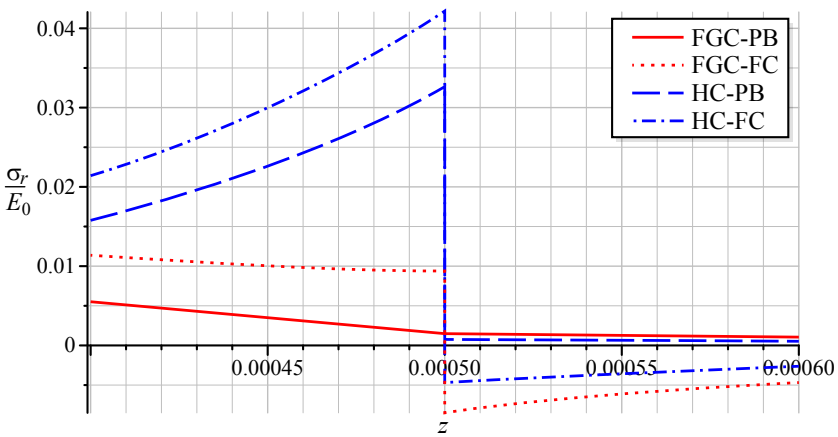

Figure 6. Normalized radial stresses near the interface for $r = 1/10\,h$.

in the graded coating, the radial displacement (FGC-PB) is about twice the corresponding value of the corresponding displacement for the homogeneous coating (HC-PB). In the frictionless contact case, the value is about three times as much. In Figure 5, we show the variations of the normalized shear stress. For FGM-PB, it has a smooth behavior at the interface, unlike the other cases. Furthermore, the FGC-PB stress is about twice the corresponding value for HC-PB. Finally, in Figure 6, we present the normalized radial stress near the interface. We observe that only the FGC-PB case is continuous, and its interface value is about $1/20$ times the corresponding value of the HC-PB in the coating.

An analysis of the radial stress solution, calculated in $r = 0$ and $z = h$ and for the HC-PB case, shows that

$$\sigma_r^{(\text{HC-PB})}(0, h^-) = \frac{f(E_0/E_h)}{h^2}, \quad \sigma_r^{(\text{FGC-PB})}(0, h) = \frac{g(E_0/E_h)}{h^2}$$

for suitable functions f and g. To better understand this we recall Boussinesq's half-space solution for

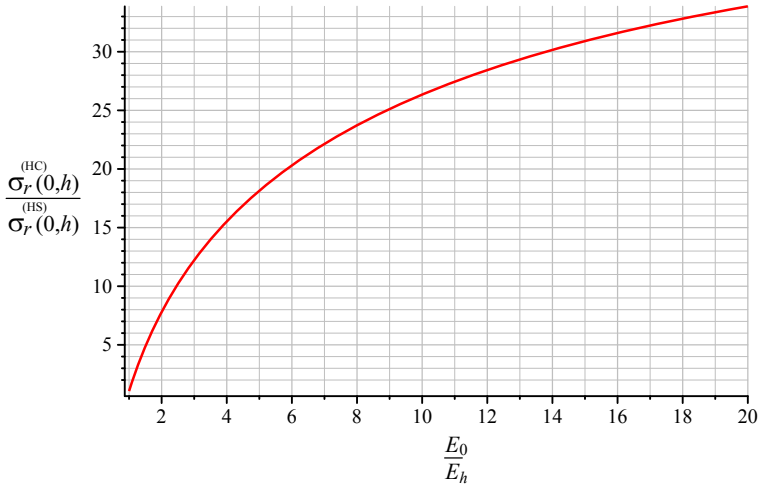

Figure 7. Radial stress ratios at the interface of the homogeneous coating.

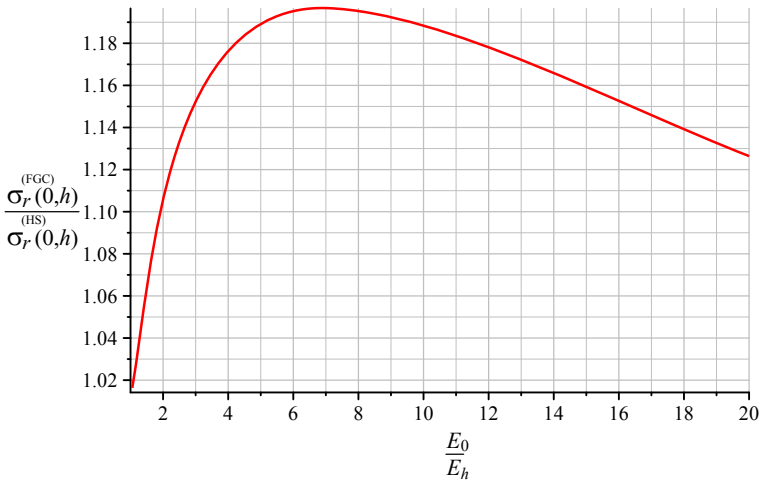

Figure 8. Radial stress ratios at the interface of the graded coating.

$r = 0$ and $z = h$, given by

$$\sigma_r^{(\mathrm{HS})}(0, h) = \frac{P(1-2\nu)}{4\pi h^2},$$

and plot in Figures 7 and 8 the ratios

$$\frac{\sigma_r^{(\mathrm{HC\text{-}PB})}(0, h^-)}{\sigma_r^{(\mathrm{HS})}(0, h)}, \qquad \frac{\sigma_r^{(\mathrm{FGC\text{-}PB})}(0, h)}{\sigma_r^{(\mathrm{HS})}(0, h)}$$

as functions of E_0/E_h. These plots show that the value at the interface of the radial stress for FGC is near the corresponding value of Boussinesq's solution. In contrast, this value for HC is quickly increasing with the ratio between the elastic properties.

6. Concluding remarks

We have determined an exact three-dimensional axisymmetric elastic solution for a functionally graded coating subjected to a point-force load. We assumed inhomogeneity governed by exponential gradation along the coating thickness, and considered two different interface conditions (perfectly bonded and frictionless contact). We compared the solution to the case of a homogeneous coating on a homogeneous substrate with different elastic properties. The analytical solution, obtained in terms of Bessel expansions, highlighted the effects of inhomogeneity on the behavior of the displacement and stress fields at the interface.

Appendix

We explicitly write the coefficients A_j, B_j, F_j, G_j of Section 4 in the case of perfectly bonded interface conditions. We first introduce the quantity

$$\Lambda = \phi_j^4\, k\big(d_1 \cos(\alpha_j h)\sin(\alpha_j h) + d_2 \cos^2(\alpha_j h) + d_3 + d_4\, e^{2h\beta_j} + d_5\, e^{-2h\beta_j}\big),$$

where

$$\begin{aligned}
d_1 &= -8\,\alpha_j\phi_j k\nu + 4\,(\beta_j^2 - 2\,k^2\nu)\alpha_j,\\
d_2 &= 8\,\phi_j^2 k\nu + 4\,(2\,k^2\nu - \beta_j^2)\phi_j + 8\,\nu\,k(k-\beta_j)(k+\beta_j),\\
d_3 &= -2\,\phi_j^3 - 4\,\phi_j^2 k\nu + (6\,\beta_j^2 - 2\,(1+2\,\nu)k^2)\phi_j + 4\,k\beta_j^2\nu - 4\,k^3\nu,\\
d_4 &= \phi_j^3 + \beta_j\phi_j^2 - (\beta_j^2 + 2\,k\nu\,\beta_j - (1-2\,\nu)k^2)\phi_j - \beta_j^3 - 2\,k\beta_j^2\nu + (1-2\,\nu)k^2\beta_j,\\
d_5 &= \phi_j^3 - \beta_j\phi_j^2 - (\beta_j^2 - 2\,k\nu\,\beta_j - (1-2\,\nu)k^2)\phi_j + \beta_j^3 - 2\,k\beta_j^2\nu + (2\,\nu-1)k^2\beta_j.
\end{aligned}$$

The constants of integration are

$$\begin{aligned}
A_j &= (p_j/\Lambda)\,\big(a_1\cos(\alpha_j h)\sin(\alpha_j h) + a_2\cos^2(\alpha_j h) + a_3\, e^{-2h\beta_j} + a_4\big),\\
B_j &= (p_j/\Lambda)\,\big(b_1\cos(\alpha_j h)\sin(\alpha_j h) + b_2\cos^2(\alpha_j h) + b_3\, e^{-2h\beta_j} + b_4\big),
\end{aligned}$$

where

$$\begin{aligned}
a_1 &= 4\,\alpha_j k^3\nu + (4\,\phi_j\nu - 2\,\beta_j)\alpha_j k^2 - 2\,\beta_j(\beta_j+\phi_j)\alpha_j k - 4\,\beta_j(\beta_j^2-\phi_j^2)(\nu-1)\alpha_j,\\
a_2 &= -4\,k^4\nu + (2\,\beta_j - 4\,\phi_j\nu)k^3 + (4\,\beta_j^2\nu - 4\,\phi_j^2\nu + 2\,\phi_j\beta_j)k^2 - 2\,\beta_j(\beta_j^2 - \phi_j^2 - \phi_j\beta_j)k\\
&\qquad + 4\,\phi_j\beta_j(\nu-1)(\beta_j^2-\phi_j^2),\\
a_3 &= (\beta_j - \phi_j)\big((1-2\,\nu)k^3 + 2\,\beta_j\nu\,k^2 - (\beta_j^2-\phi_j^2)k\big),\\
a_4 &= -2\,\nu\,k^2(\beta_j^2-\phi_j^2) + 2\,k^4\nu + ((1+2\,\nu)\phi_j - \beta_j)k^3 - 2\,\phi_j\beta_j(\beta_j^2-\phi_j^2)(\nu-1)\\
&\qquad + (\phi_j^3 + \beta_j^3 - 3\,\phi_j\beta_j^2 - \beta_j\phi_j^2)k
\end{aligned}$$

and

$$b_1 = -4k^4\nu+(2\beta_j-4\phi_j\nu)k^3+(4\beta_j^2\nu-4\phi_j^2\nu+2\phi_j\beta_j)k^2+2\beta_j(\phi_j^2+\phi_j\beta_j-\beta_j^2)k+4\phi_j\beta_j(\nu-1)(\beta_j^2-\phi_j^2),$$
$$b_2 = -4\alpha_j k^3\nu + (2\beta_j - 4\phi_j\nu)\alpha_j k^2 + 2\beta_j(\beta_j+\phi_j)\alpha_j k + 4\beta_j(\beta_j^2-\phi_j^2)(\nu-1)\alpha_j,$$
$$b_3 = \alpha_j(\beta_j-\phi_j)(k-\beta_j)(k-2k\nu+2\beta_j-2\beta_j\nu),$$
$$b_4 = 2\alpha_j k^3\nu - (\beta_j-\phi_j-2\phi_j\nu)\alpha_j k^2 - \beta_j(\beta_j+\phi_j)\alpha_j k - 2\beta_j(\beta_j^2-\phi_j^2)(\nu-1)\alpha_j.$$

The remaining coefficients are

$$F_j = e^{h(k+\phi_j)}\big[p_j f_1 e^{-h\beta_j} + A_j\big(f_2\sin(\alpha_j h) + f_3\cos(\alpha_j h)\big) + B_j\big(f_4\sin(\alpha_j h) + f_5\cos(\alpha_j h)\big)\big],$$
$$G_j = e^{h(k+\phi_j)}\big[p_j g_1 e^{-h\beta_j} + A_j\big(g_2\sin(\alpha_j h) + g_3\cos(\alpha_j h)\big) + B_j\big(g_4\sin(\alpha_j h) + g_5\cos(\alpha_j h)\big)\big],$$

where

$$f_1 = \big((1-h\phi_j)(k-\beta_j)-(\alpha_j^2+\beta_j^2+k^2-2\beta_j k)h\big)\sin(\alpha_j h)/(\alpha_j\phi_j^4)-(1-h\phi_j)\cos(\alpha_j h)/\phi_j^4,$$
$$f_2 = \big(-2\beta_j+(2\phi_j\beta_j+2\beta_j k-2\beta_j^2-\alpha_j^2)h\big)e^{-h\beta_j}/\alpha_j + e^{h\beta_j}\alpha_j h,$$
$$f_3 = 2\sinh(h\beta_j)(1-h\beta_j-hk-h\phi_j),$$
$$f_4 = 2\sinh(h\beta_j)(1-hk-h\phi_j)-2\cosh(h\beta_j)\beta_j h,$$
$$f_5 = -2\sinh(h\beta_j)\alpha_j h,$$
$$g_1 = (\alpha_j^2+\beta_j^2+k^2-2\beta_j k+\phi_j k-\phi_j\beta_j)\ \sin(\alpha_j h)/(\alpha_j\phi_j^4)-\alpha_j\cos(\alpha_j h)\phi_j,$$
$$g_2 = -e^{h\beta_j}\alpha_j-(2\phi_j\beta_j+2\beta_j k-2\beta_j^2-\alpha_j^2)e^{-h\beta_j}/\alpha_j,$$
$$g_3 = 2\sinh(h\beta_j)(\beta_j+k+\phi_j),$$
$$g_4 = 2\cosh(h\beta_j)\beta_j+2\sinh(h\beta_j)(k+\phi_j),$$
$$g_5 = 2\sinh(h\beta_j)\alpha_j.$$

References

[Birman and Byrd 2007] V. Birman and L. W. Byrd, "Modeling and analysis of functionally graded materials", *Appl. Mech. Rev.* **60** (2007), 195–216.

[Erdogan 1995] F. Erdogan, "Fracture mechanics of functionally graded materials", *Compos. Eng.* **5**:7 (1995), 753–770.

[Kashtalyan and Menshykova 2008] M. Kashtalyan and M. Menshykova, "Three-dimensional analysis of a functionally graded coating/substrate system of finite thickness", *Phil. Trans. R. Soc. A* **366**:1871 (2008), 1821–1826.

[Liu and Wang 2008] T.-J. Liu and Y.-S. Wang, "Axysimmetric frictionless contact problem of a functionally graded coating with exponentially varying modulus", *Acta Mech.* **199** (2008), 151–165.

[Love 1927] A. E. H. Love, *A treatise on the mathematical theory of elasticity*, 4th ed., Cambridge University Press, Cambridge, 1927. Reprinted by Dover, New York, 1944.

[Martin et al. 2002] P. A. Martin, J. D. Richardson, L. J. Gray, and J. R. Berger, "On Green's function for a three-dimensional exponentially graded elastic solid", *Proc. R. Soc. Lond. A* **458**:2024 (2002), 1931–1947.

[Plevako 1971] V. P. Plevako, "On the theory of elasticity of inhomogeneous media", *Prikl. Mat. Mekh.* **35**:5 (1971), 853–860. In Russian; translated in *J. Appl. Math. Mech.* **35**:5 (1971), 806–813.

[Sburlati 2009a] R. Sburlati, "Adhesive elastic contact between a symmetric indenter and an elastic film", *Int. J. Solids Struct.* **46**:5 (2009), 975–988.

[Sburlati 2009b] R. Sburlati, "Three-dimensional analytical solution for an axisymmetric biharmonic problem", *J. Elasticity* **95**:1-2 (2009), 79–97.

[Sburlati and Bardella 2011] R. Sburlati and L. Bardella, "Three-dimensional elastic solutions for functionally graded circular plates", *Eur. J. Mech. A Solids* **30**:3 (2011), 219–235.

[Sneddon 1966] I. N. Sneddon, *Mixed boundary value problems in potential theory*, North-Holland, Amsterdam, 1966.

[Suresh 2001] S. Suresh, "Graded materials for resistance to contact deformation and damage", *Science* **292**:5526 (2001), 2447–2451.

[Watson 1922] G. N. Watson, *A treatise on the theory of Bessel functions*, 2nd ed., Cambridge University Press, Cambridge, 1922. Reprinted in 1995.

Received 31 Jan 2012. Revised 17 Mar 2012. Accepted 5 Apr 2012.

ROBERTA SBURLATI: sburlati@dicat.unige.it
Department of Civil, Environmental and Architectural Engineering (DICAT), and Research Center for Materials Science and Technology (MaST), University of Genova, Via Montallegro 1, 16145 Genova, Italy

SUBMISSION GUIDELINES

ORIGINALITY

Authors may submit manuscripts in PDF format online at the Submissions page. Submission of a manuscript acknowledges that the manuscript is original and has neither previously, nor simultaneously, in whole or in part, been submitted elsewhere. Information regarding the preparation of manuscripts is provided below. Correspondence by email is requested for convenience and speed. For further information, write to one of the Chief Editors:

Davide Bigoni	bigoni@ing.unitn.it
Iwona Jasiuk	ijasiuk@me.concordia.ca
Yasuhide Shindo	shindo@material.tohoku.ac.jp

LANGUAGE

Manuscripts must be in English. A brief abstract of about 150 words or less must be included. The abstract should be self-contained and not make any reference to the bibliography. Also required are keywords and subject classification for the article, and, for each author, postal address, affiliation (if appropriate), and email address if available. A home-page URL is optional.

FORMAT

Authors can use their preferred manuscript-preparation software, including for example Microsoft Word or any variant of TEX. The journal itself is produced in LATEX, so accepted articles prepared using other software will be converted to LATEX at production time. Authors wishing to prepare their document in LATEX can follow the example file at www.jomms.net (but the use of other class files is acceptable). At submission time only a PDF file is required. After acceptance, authors must submit all source material (see especially Figures below).

REFERENCES

Bibliographical references should be complete, including article titles and page ranges. All references in the bibliography should be cited in the text. The use of BibTEX is preferred but not required. Tags will be converted to the house format (see a current issue for examples); however, for submission you may use the format of your choice. Links will be provided to all literature with known web locations; authors can supply their own links in addition to those provided by the editorial process.

FIGURES

Figures must be of publication quality. After acceptance, you will need to submit the original source files in vector format for all diagrams and graphs in your manuscript: vector EPS or vector PDF files are the most useful. (EPS stands for Encapsulated PostScript.)

Most drawing and graphing packages—Mathematica, Adobe Illustrator, Corel Draw, MATLAB, etc.—allow the user to save files in one of these formats. Make sure that what you're saving is vector graphics and not a bitmap. If you need help, please write to graphics@msp.org with as many details as you can about how your graphics were generated.

Please also include the original data for any plots. This is particularly important if you are unable to save Excel-generated plots in vector format. Saving them as bitmaps is not useful; please send the Excel (.xls) spreadsheets instead. Bundle your figure files into a single archive (using zip, tar, rar or other format of your choice) and upload on the link you been given at acceptance time.

Each figure should be captioned and numbered so that it can float. Small figures occupying no more than three lines of vertical space can be kept in the text ("the curve looks like this:"). It is acceptable to submit a manuscript with all figures at the end, if their placement is specified in the text by means of comments such as "Place Figure 1 here". The same considerations apply to tables.

WHITE SPACE

Forced line breaks or page breaks should not be inserted in the document. There is no point in your trying to optimize line and page breaks in the original manuscript. The manuscript will be reformatted to use the journal's preferred fonts and layout.

PROOFS

Page proofs will be made available to authors (or to the designated corresponding author) at a Web site in PDF format. Failure to acknowledge the receipt of proofs or to return corrections within the requested deadline may cause publication to be postponed.

Journal of Mechanics of Materials and Structures

Volume 7, No. 4 April 2012